Polar and Dipolar Contributions to Collective Cell Motility



Guanming Zhang

Keble College

University of Oxford

A thesis submitted for the degree of

Doctor of Philosophy

Trinity 2022

Abstract

Active materials take energy from their surroundings and use it to do mechanical work. The theories of active matter can describe a wide variety of living systems, such as bacterial colonies, actin-myosin networks and cell tissues. In this thesis, we investigate the collective behaviour of confluent, two-dimensional cell monolayers on a substrate, which is also one of the most common experimental systems to study collective cell motility. The cells are modelled using a computational phase field approach to study how polar and dipolar forces, the active, out-of-equilibrium force components, contribute to the cell motions.

We study the polar and dipolar contributions to collective cell motility using the phase-field model, which allows simulations of deformable cells. We study the interplay between the polar and dipolar forces in a confluent cell sheet and explore the collective behaviour emerging from different polarisation mechanisms. We find that either polar or dipolar forcing can drive the jammed-to-liquid transition. The mechanical properties, such as the cell deformation and speed, are independent of the polarisation mechanisms. However, a flocking state where most cells move in the same direction appears when the polar force of a cell aligns with its velocity as an exception.

Then we focus on studying the active inter-cellular force in a cell monolayer. We find that contractile inter-cellular forces elongate a cell and can give rise to a nematic state and active turbulence. Extensile inter-cellular forces cause frustration, where cells elongate perpendicular to their neighbours. Moreover, we show that anisotropic fluctuation in the inter-cellular forces can lead to the transition from contractile to extensile behaviour.

Finally, we investigate the interplay between the viscoelasticity of tissue and the inter-cellular forces for cells confined in a channel. We find that different collective behaviour emerges as viscoelasticity of the tissue is modulated by the cell-cell adhesion, repulsion. The transition between the jammed, nematic state, oscillation and spontaneous shear flow occurs as the cell-cell adhesion increases. The cells jam more easily with higher cell-cell repulsion, and cells of a higher aspect ratio favour steady shear.

The approaches developed in this thesis can be extended and applied to investigate other biological processes in cell mechanics, such as tissue expansion and the phase ordering of different cell types.

Acknowledgements

First of all, I would like to thank my supervisor, Prof. Julia Yeomans, for welcoming me into her research group and for her patient guidance. I appreciate your help in my research with your rich experience, which always provides me with a bigger picture and a better understanding of my research projects.

I would like to thank Amin Doostmohammadi for his guidance in my first year, for introducing the phase-field model to me, and Romain Mueller for providing the phase-field code. I also benefited a lot from Liam Ruske for countless interesting discussions, ideas in research, and chats. Also, I thank Saraswat Bhattacharyya, Ioannis Hadjifrangiskou, James Graham, Muriel van der Laan, Andrew Orr, Kristian Thijssen, Rian Hughes, Amin Doostmohammadi, Emmanuel Lance Plan and Yavor Novev in Julia's group for coffee breaks, discussions and interesting chats.

I would like to thank my friends in theoretical physics, in particular Minghao Li, Hanzhi Jiang, Shuofeng Zhang and Chengdong Li. Minghao, thank you for introducing the books you have read to me and sharing the interesting things in your daily life with me. Chengdong, thank you for continuously talking to me about your research in astrophysics and encouraging me to get things done. I thank my friend, also my research collaborator, Jun Zhang, for introducing experimental knowledge to me during our nice collaboration. I also thank Prof. Garret Cotter for providing me with the opportunity to teach at Exeter College.

Also, I would like to thank Prof. Michael Somekh for introducing the numerical study of optical vortices to me, which was my first research experience in physics.

I would like to thank everyone who helped me through the dark time of the pandemic. I thank my mother-in-law and father-in-law for caring about my health conditions. I thank the help from Michelle Jose and Keble MCR. I also thank my friends in the US for having countless chats with me online, although you are hundreds of miles away, in particular, Peijie Li. I thank my roommates for my undergraduate study. We scattered in three time zones, but we still managed to chat online simultaneously as if we were in the nostalgic, warm old days.

I thank my family members for their support, in particular, my cousins Yueyao Li and Xiaojuan Zhu. Special thanks are given to my parents who have always been supportive and helping me with their unconditional love.

Finally, I would like to thank my wonderful wife, Yunqi Zhou. Thank you for encouraging me to go through the ups and downs of the past years. Thanks for all the dishes you cooked for me with a unique taste of love from you.

Publications

Authored publications contributing to this thesis

1. G. Zhang, R. Mueller, A. Doostmohammadi, and J. M. Yeomans. Active inter-cellular forces in collective cell motility. *Journal of the Royal Society Interface* **2020**, 17, 20200312

2. G. Zhang, and J. M. Yeomans. Active inter-cellular forces in collective cell motility. *arXiv preprint* **2021**, arXiv:2111.14401 2021.

The work presented in Chapter 6 is currently being prepared for publication:

3. G. Zhang, and J. M. Yeomans. The interplay between tissue viscoelasticity and active intercellular forces. *in preparation*

Contents

List of Figures **xiii**

1 Introduction **1**

1.1 Introduction to active matter 1

1.2 Introduction to cell mechanics 4

1.2.1 Single eukaryotic cell movement 5

1.2.2 Collective cell motion 5

1.3 Physical models for collective cell motion 11

1.3.1 Disk model 12

1.3.2 Cellular Potts model 12

1.3.3 Active vertex model and Voronoi model 13

1.4 Overview of the thesis 14

2 Active nematic theory **17**

2.1 Liquid crystals 18

2.2 Nematic order parameter 19

2.3 Active nematics 20

2.4 Topological defects 21

2.4.1 Active half-integer defects 23

3 Phase Field Model **27**

3.1 Phase field dynamics 28

3.2 Passive forces 29

3.3 Active forces 33

3.3.1 Polar force 33

3.3.2 Dipolar forces: self elongation and inter-cellular forces . . . 36

3.4 Implementation of the model 40

3.5 Recent progress in modelling cells using the phase field model . . . 40

4 Active dipolar and polar forces in collective cell motility 43
4.1 Introduction . . . 43
4.2 Simulation method . . . 44
4.3 Results . . . 45
4.3.1 Unjamming . . . 45
4.3.2 Cell deformations . . . 48
4.3.3 Cell speed and flocking . . . 51
4.4 Discussion . . . 53

5 Active forces in confluent cell monolayers 57
5.1 Introduction . . . 57
5.2 Simulation method . . . 59
5.3 Inter-cellular contractile forces without fluctuations . . . 59
5.4 Inter-cellular extensile forces without fluctuations . . . 60
5.5 Fluctuations . . . 62
5.6 Discussion . . . 63

6 The interplay between tissue viscoelasticity and active inter-cellular forces 65
6.1 Introduction . . . 65
6.2 Boundary conditions and simulation method . . . 67
6.2.1 Boundary conditions . . . 67
6.2.2 Simulation method . . . 67
6.3 Results . . . 68
6.3.1 Transitions between jammed, oscillatory shear and shear flow states . . . 68
6.3.2 Jammed, nematic state . . . 70
6.3.3 Active instability induced oscillation and wave-like behaviour 70
6.3.4 Spontaneous shear flow . . . 73
6.3.5 The effects of the cell aspect ratio . . . 74
6.4 Discussion . . . 75

7 Discussion 79
7.1 Summary . . . 79
7.2 Outlook . . . 81
7.2.1 Mechanical waves during cell spreading . . . 81
7.2.2 Mechanochemical Coupling . . . 81
7.2.3 Cell sorting by active inter-cellular force . . . 82

Appendices

A Implementaion of the model **85**
A.1 Finite difference 85
A.2 Predictor-corrector method 86
A.3 Euler-Maruyama method 86

B Measurements: center of mass, velocity, cell orientation and defect detection **89**
B.1 Cell velocity 89
B.2 Deformation tensor and cell orientation 90
B.2.1 Coarse-grained fields 91
B.2.2 Defect detection 92

C Additional comments **93**
C.1 The cell-cell adhesion 93
C.2 Supplementary figures for Chapter 5 94
C.3 Supplementary information for Chapter 6 97
C.3.1 Oscillation period 97
C.4 Viscoelastic behaviour of passive tissue 97

References **101**

List of Figures

1.1 Active matters: microtubule, bacteria swimmer and epithelial cells. 2
1.2 Active half-integer defects in living systems 3
1.3 Schematics for single cell motility. 4
1.4 Coordination mechanisms of cell polarisation 7
1.5 Topological defects and nematic instability in confluent cell monolayers 9
1.6 Schematics and snapshots of different in-silico physical models . . . 11

2.1 Schematics of matter in solid, liquid and nematic phase. 18
2.2 Schematic showing contractile and extensile particles exerting a pair of equal and opposite forces 20
2.3 Schematics of topological defects with different charges. 22
2.4 The director fields (red lines) and velocity fields (black arrows) around +1/2 and -1/2 defects for a contractile system 23

3.1 Passive dynamics in the phase field model 30
3.2 The possible dynamics for cell polarisation 36
3.3 Dipolar force densities 37

4.1 Snapshots from the simulations 46
4.2 Stability diagrams 47
4.3 Unjamming 48
4.4 Liquid state 49
4.5 Cell shape 50
4.6 Cell movement 52
4.7 Cell shape index 55

5.1 Snapshots of the simulations 58
5.2 Cell and defect dynamics driven by inter-cellular forces 61
5.3 Defect velocity 63
5.4 Distributions of the elongation axes of neighbouring cells 64

6.1 Schematic for cells confined in a channel 67
6.2 ΔV_x and ΔV_x^{abs} are measures of different states 69
6.3 Oscillations 72

6.4 Wave-like behaviour 74
6.5 The shear flow state 75
6.6 Phase diagram as a function of ω and AR_0 76

B.1 Defect detection 92

C.1 Systems with both inter-cellular and self deformation forces 94
C.2 Trefoil-like, -1/2, defects in simulations without fluctuations 95
C.3 Behaviour of comet-like, +1/2, defects as anisotropic fluctuations are introduced 96
C.4 **Oscillation period:** The oscillation period as a function of the cell-cell adhesion ω. $AR_0 = 1.0$ and $\kappa = 4.0$ for this figure. 97
C.5 **Viscoelastic behaviour for the passive tissue:** (a) The shear strain,ϵ_{xy} and tissue stress σ_{xy} as a function of time. (b) The cross-correlation between ϵ_{xy} and σ_{xy}. It peaks at $\tau \approx -1920$ which corresponds to $\delta \approx 0.603$ (34.56^o). $AR_0 = 1.0$, $\kappa = 4.0$, $\omega = 0.75$ and $\zeta_{\text{inter}} = 0$ for this figure. 98

1 Introduction

Activity and motility are essential in living systems, and they give rise to various collective behaviours. The research field of active matter focuses on understanding the physical mechanism behind them. First, we discuss active polar and nematic matter in general and focus on how these features lead to different collective motions in cell mechanics. Also, we briefly introduce how physical models can be applied to study collective cell mechanics.

1.1 Introduction to active matter

Active matter describes out-of-equilibrium systems where individual particles take energies and convert them to mechanical work. The scale of a single active element ranges from a bacterium and cell of size a few micrometres to a fish or bird on the scale of metres. Collective behaviour on scales larger than an individual's size emerges as active particles come together and interact with each other. These collective behaviours are widely present in biological systems as living matter organises and coordinates collectively to better adapt to the environment, develop biological functions or compete with other species.

The active matter we are interested in is over-damped or viscous active systems at a low Reynolds number where the inertia of particles is negligible. These systems

are typically made of biopolymers such as microtubule and kinesin motors, bacteria or eukaryotic cells (Fig. 1.1). However, analysing these systems in a reductionism approach, e.g. studying the equation of motion for all the protein molecules in cells to understand the tissue mechanics, is inefficient and computationally exhaustive. Luckily, the collective behaviours of active systems made of different individuals share some common characteristics, which allows one to study them generically. One important aim of active matter research is to model the active entities in a minimum way without losing the emergence of the collective features.

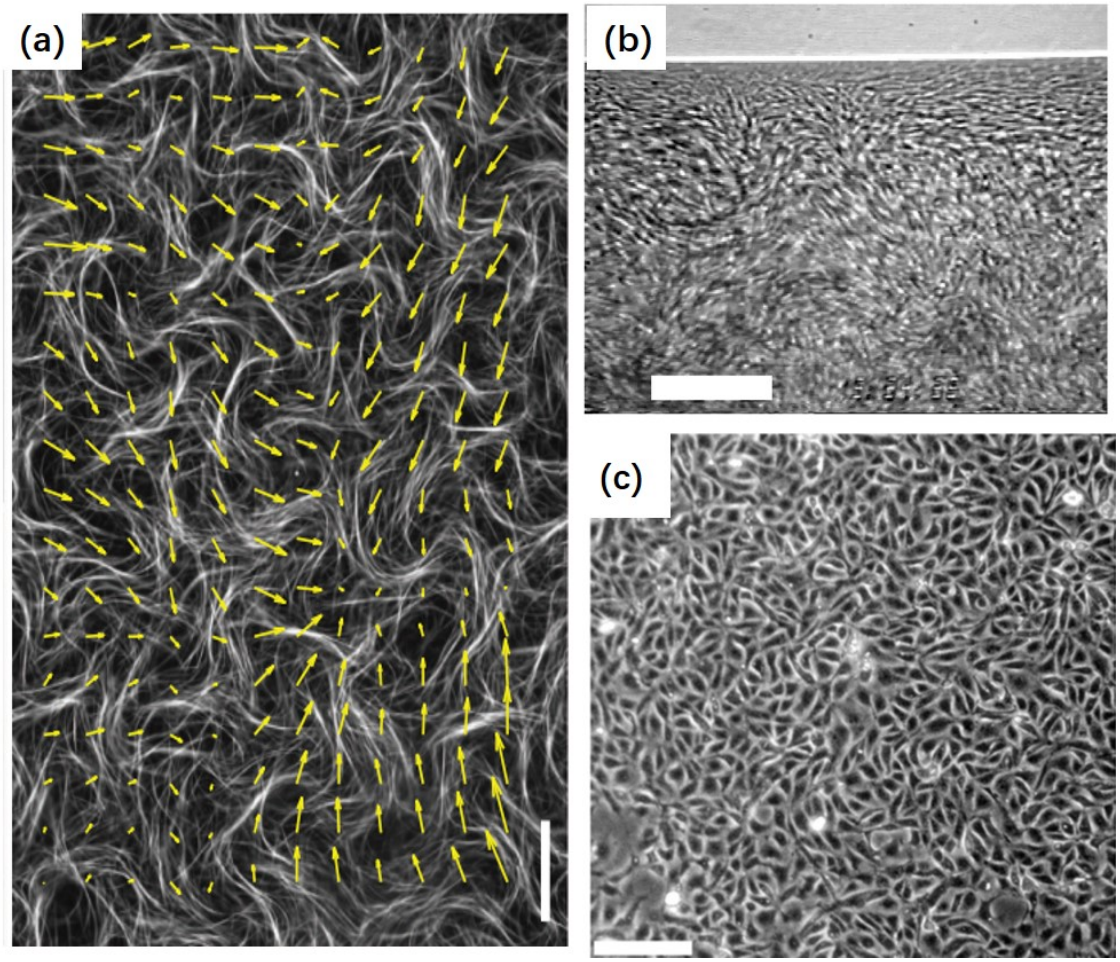


Figure 1.1: (a) The motion of an active microtubule network. The local velocity is shown by the yellow arrows. Scale bar, 80 μm (b) Bacterial flow viewed from below through the bottom of a petri dish. The scale bar is 35 μm. (c) A confluent MDCK cell monolayer shows a spatially jammed, glassy state. Scale bar, 100 μm. (a) (b) and (c) are adapted from [1], [2] and [3] respectively.

The forcing and their interactions classify most active matter particles as polar or

nematic. Polar units are described by a vector $\mathbf{p}$, the polarisation, which represents their self-propelled direction [4]. For these particles, the heads and tails are not equivalent ($\mathbf{p} \neq -\mathbf{p}$), thus making the individuals polarised. The first computational implementation of polar particles was the Vicsek model. This has been used to study the emergence of self-clustering motion in the presence of biological interactions [5]. In the Vicseck model, the self-propulsion ability of agents is modelled by assigning them velocities of constant magnitude, and individuals prefer to align their velocities parallel to their neighbours under the influence of random noise. A transition from random motion to a flocking state where all the particles move in the same direction as the number density of particles increases or the noise level decreases is observed [5]. Based on symmetry arguments only, Toner and Tu proposed an effective continuum theory of active polar matter [6].

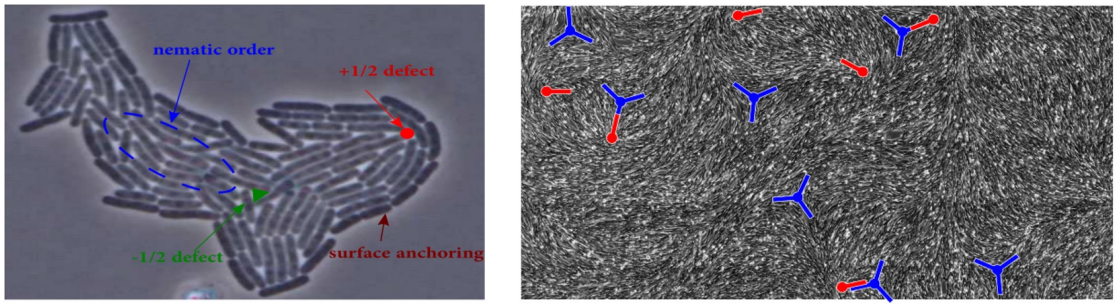


Figure 1.2: (a) The morphology of an E. coli colony responds to the motion of +1/2 defects at the interface (b) +1/2 defects (red, comet-like markers) and -1/2 defects (blue, trefoil-like markers) in neural progenitor cells. (a) and (b) are adapted from [7] and [8] respectively.

Active nematics are distinguished from polar particles by their head-tail symmetry. The orientation of a nematic individual is described by a nematic director $\mathbf{n}$ with symmetry $\mathbf{n} = -\mathbf{n}$. For low-Reynolds number hydrodynamic systems, active nematics exert dipolar forces on the solution and generate flows, and individual particles rotate in response to the flow field generated by others, resulting in active nematic hydrodynamics. This feedback between flow and local orientation leads to nematic instabilities where misalignment induced by hydrodynamic instabilities appears at the boundary of locally ordered nematic regions, forming "wall" structures [9, 10]. As the instability grows, an active turbulent state where the flow field of

the system is chaotic and random emerges on a characteristic length scale much larger than the single particle size. In contrast to turbulence in high-Reynolds number systems due to inertial effects, active nematic turbulence is correlated to the orientation field. Half-integer defect pairs, singular points in the orientation field, are found to proliferate at the "walls". The +1/2 half defects move, stir the flow and finally annihilate with -1/2 defects. In bacterial colonies [7], microtubules [1] and cell monolayers [11–13], local orientational order and half-integer defects have been observed, displaying the feature of active nematics. Examples are shown in Fig. 1.2

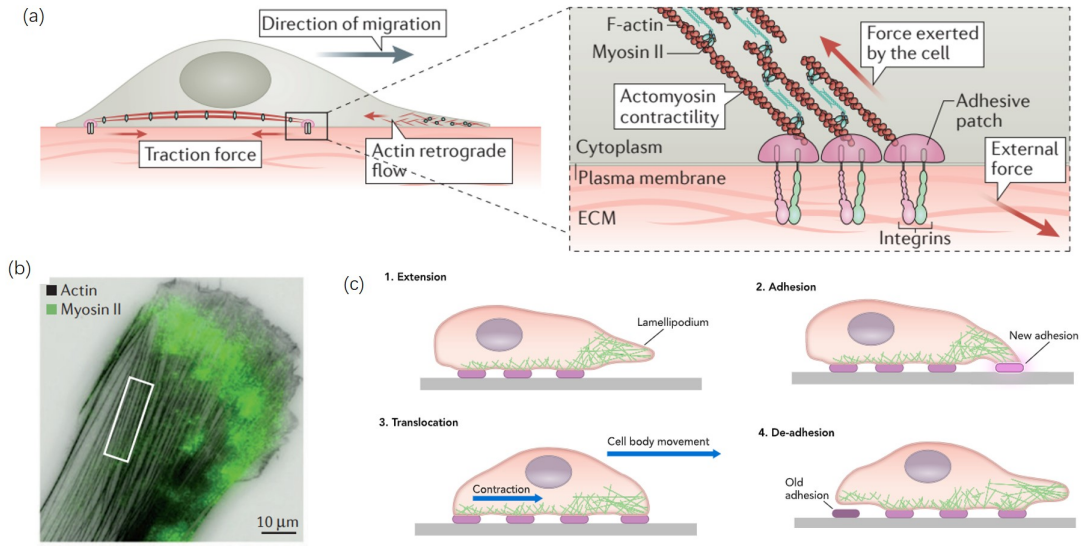


Figure 1.3: (a) Actomyosin networks exert traction forces on the substrate. (b) Immunofluorescence images of actin and myosin II of smooth muscle from a human airway. (c) Schematic of the single-cell crawling process. First, the cell grows a lamellipodium by actin filament protrusion. Then, it forms focal adhesion sites at the basal membrane. Next, the cell body is dragged to move forward by myosin motor contractility, the rear end of a cell is retracted, and the adhesion sites at the rear detach from the substrate. (a), (b) and (c) are adapted from [14], [15] and [16] respectively.

1.2 Introduction to cell mechanics

How cells can detect their neighbouring environment and adapt their shapes, motility and other local properties accordingly is not fully understood. Numerous in-vitro and in-vivo experiments have been performed by biologists to unravel the biochemical process occurring in collection motions. Here, we shall take a physics viewpoint that

the cells are examples of active matter, featuring both polar and nematic properties. The first step in studying cell mechanics is to understand single-cell behaviour.

1.2.1 Single eukaryotic cell movement

The cytoskeleton support cell structures and determines cell elasticity, the ability to resist deformation, by maintaining a cell's shape and inner structure. It is made of three major components, actin filaments, intermediate filaments and microtubules [17]. Actin-filaments, long bio-polymer chains made of actin proteins, together with myosin motors which provides contractility, are named actomyosin. These structures are crucial to cell motility [14]. Fig. 1.3(a) shows a schematic of the actomyosin network and the proteins relevant to cell protrusion. Fig. 1.3(b) labels the actin and myosin II for muscle cells.

Single cell movement is a relatively well-studied, complicated process involving different biochemical functions. It can be roughly described as a 4-step process. (1) actin filaments polymerise and protrude at the cell's leading edge to form lamellipodia. (2) focal adhesion sites are then formed at the basal membrane and attach to the substrate. (3) the cell body is dragged to move forward by myosin motor contractility. (4) the rear end of the cell is retracted, and the adhesion sites at the rear detach from the substrate. These steps then repeat in a single cell's directional motion. However, the motion is more complicated when cells are put together. Cell-cell interactions and collective guidance frequently occur, dominant over single-cell mechanics.

1.2.2 Collective cell motion

Collective cell motion is essential for morphogenesis, wound healing and tissue development. How to bridge single cell motion and the collective behaviour at the tissue level is still a challenging problem. Measurements of the displacement, the force and the cell shape as a function of time are necessary to study collective cell mechanics. One of the useful systems to achieve these measurements is an epithelial cell monolayer (an example is shown in Fig. 1.1(c)) where particle image velocimetry,

traction force microscopy and monolayer microscopy have been extensively applied to measure the velocity field, traction force and tissue stress [14]. Moreover, this system allows experiments in different geometries to mimic the in-vivo environment. For example, experiments on monolayers with free edges have been used to study tissue spreading, and laser ablation has been applied to investigate cell dynamics in wound healing and gap closure [18, 19].

To obtain a confluent cell monolayer (a cohesive, single-layer cell sheet covering the entire culture dish), cells are seeded at the centre of a soft gel substrate and cultured for a few days to reach confluency. As the cell layer reaches confluency, cadherin-based cell-cell junctions linking across neighbouring cells are developed. These junctions not only make the cells cohesive but also play a role in mechanosensing and force transmission. These properties differentiate collective cell behaviour from a superposition of non-interacting single-cell motions.

As long as the cells are not too tightly packed, they continually move around within the cluster, with flow patterns that show high vorticity and localised bursts of high velocities [20], reminiscent of the active turbulence that characterises dense active nematic materials [21]. As cell density increases to a certain level, most cells are jammed without migration. However, the motile cells in the layer can move together to develop multi-cellular flow. This velocity profile resembles the glassy state in colloid systems [3]. Fibroblasts and epithelial cells are able to become jammed only at extremely high packing fractions [22–24].

In wound healing and tissue expansion experiments, strongly polarised cells near the open space move persistently towards the empty regions. The coordination of polarisation, the mechanism of how cells sense their environment and drive their motility based on chemical or mechanical cues, may account for how persistent polarisation is established. An increasing number of observations show that different coordination mechanisms of cell polarisation are essential in collective cell behaviours. Here we briefly review some of them.

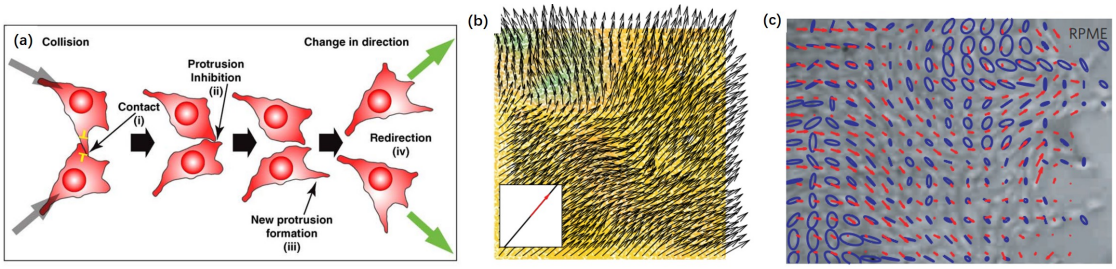


Figure 1.4: (a) CIL starts with cell-cell contact (yellow), resulting in repolarisation in the direction pointing away from the cell-cell contact (green arrows). (b) Flocking motion of MCF-10A cells after RAB5A treatment. The local velocity and average velocity over the tissue are shown by black and red arrows. (c) Traction forces (red arrows) align to the long axis of the local stress ellipse (blue), indicating plithotaxis guidance. (a) (b) and (c) are adapted from [25], [26] and [27] respectively

Contact inhibition of locomotion

Contact inhibition of locomotion (CIL) was an effect discovered and reported by Michael Abercrombie in 1954 [28]. He described it as "the phenomenon of a cell ceasing to continue moving in the same direction after contact with another cell" [29]. Pairwise CIL starts with cell-cell contact. Then the actin filament protrusion is inhibited; cells start to re-polarise in the opposite direction to avoid cell-cell contact; and finally, cells move apart. Fig. 1.4(a) shows the dynamics of CIL for binary collisions. One of the features shared by collective migration in various cell types is that cells at the leading edge are always strongly polarised and develop coordinated, persistent protrusion, and CIL may account for this effect [25]. For example, scanning electron microscopy has been applied to investigate neural crest cells in vitro and in vivo to unravel whether CIL causes this feature. In the experiment, neural crest cells were seeded and grouped into clusters. The peripheral cells moved away from the cluster by repolarising outwards. The internal cells moved randomly with no preferred direction. These internal cells regained their polarisation once they touched the free space after the outer cells were removed. These observations suggest that the establishment of leading edge polarisation is likely caused by CIL [30].

Polarisation-velocity alignment

The transition from a glassy state to a coherent, multi-cellular scale flocking state where all the cells move towards the same direction can be induced by RAB5A, an endocytic protein related to functions of cell-cell junction [26]. (Fig. 1.4 (b))[26, 31]. Combinations of experiments and computational physical models suggest that this effect may emerge from the alignment of polar forces to cell velocities, and a persistent alignment is necessary to account for the flocking state [31, 32].

Plithotaxis

Monolayer microscopy, traction force microscopy and phase contrast image analysis techniques have been applied to study the correlation between inter-cellular stresses, cell orientation and cell motility, suggesting that the angle between traction and the major axis of stress is correlated (Fig. 1.4(c)) [27, 33]. For example, there is evidence that cells polarise and tend to exert traction in the direction of minimum local shear stress, a phenomenon referred to as plithotaxis [27]. From the viewpoint of continuum modelling, this phenomenon may indicate the flow aligning parameter, which quantifies the alignment between polarisation and local strain is much larger than that in passive liquid crystals [34].

Nematic features such as half-integer defects and active turbulence induced by dipolar forces are important in controlling how cells move collectively, and these phenomena may not be captured by a polar forcing. It is natural that long and thin spindle-shaped fibroblast cells can behave as nematic particles [8, 11], and they demonstrate the emergence of active self-propelled $+1/2$ defects (Fig. 1.5(a)) [11]. Spontaneous shear flow for nematic particles confined in a channel is one of the well-known features for active nematics [11] [35]. Such a feature has been found for spindle shape fibroblasts confined in a channel (Fig. 1.5(c)). In addition, bifurcation in cell orientations was observed in the same experiment, implying nematic cell chirality. Interestingly, Madin-Darby canine kidney (MDCK) tissue, a naturally round epithelial cell, also manifests nematic behaviour by showing active half-integer defects. Moreover, the topological defects have been demonstrated to

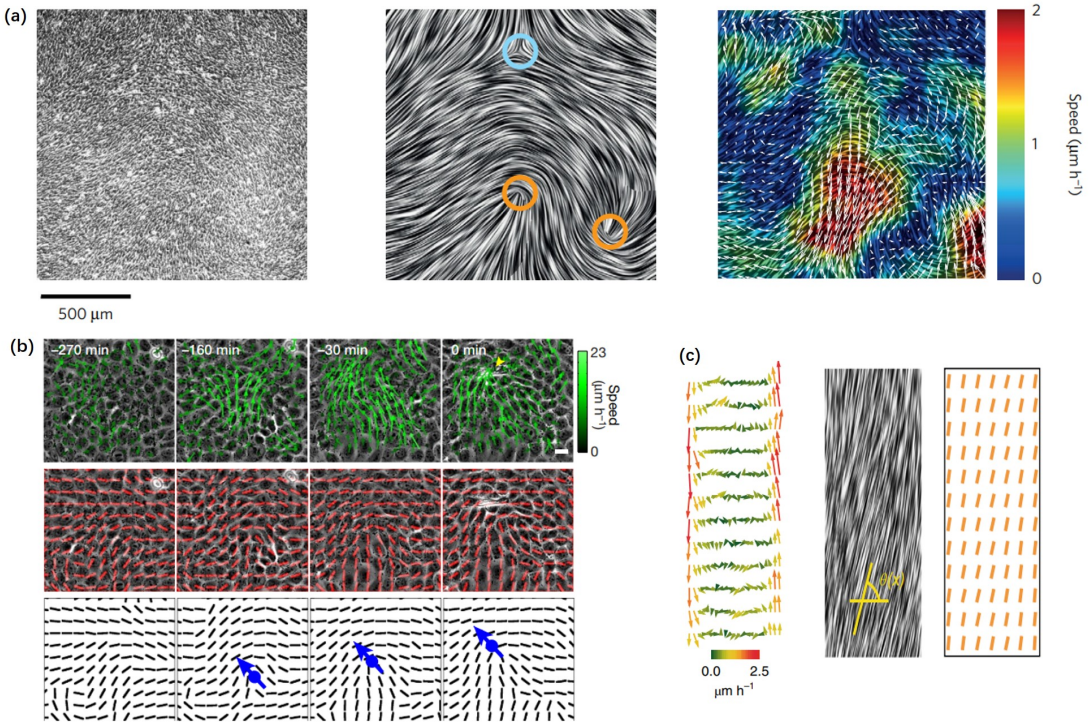


Figure 1.5: (a) Left: Phase contrast image of long and thin NIH 3T3 cells forming a monolayer. Middle: Field lines of the orientation field around +1/2 (orange) and -1/2 (cyan) defects circles. Right: Velocity field around the +1/2 defect. (b) Upper: the velocity field (green arrows) for MDCK cells. Middle: the orientation field (red bars). Lower: the motion of a +1/2 defect (blue dots, the arrows show the tail-to-head direction of motion) overlaid on the orientation field. (c) Left: velocity field of RPE1 cells confined in a strip; Middle: line integral convolution shows the orientation of cells; Right: orientation of the confined cells. (a), (b) and (c) are adapted from [11], [12] and [35].

link to biological functions: The defects in MDCK monolayers are hot spots of local pressure which control the release of yes-associated protein (YAP), a cell life-cycle-related chemical, and serve as a mechanical cue to indirectly influence the fate of cells [12]. Fig. 1.5(b) shows the motion of +1/2 defects in the MDCK monolayer. Experiments on the same type of cells suggest that cadherin-based cell-cell junctions play an important role in cell activity. The velocity of +1/2 defects changes from moving tail-to-head to moving head-to-tail when E-cadherin is knocked out [13]. Biologically, lamellipodia formation is usually suppressed in confluent cell layers, implying the inter-cellular interactions may account for the active turbulence.

In some experiments, active polar and nematic forces can coexist and compete

against each other, giving rise to interesting collective effects. For example, active wetting and dewetting transitions have been observed in a two-dimensional cluster of epithelial cells [36]. In contrast to its counterpart in nonactive systems, this transition is mainly driven by cell motility and contractility, which is observed by traction microscopy and tested by perturbation on E-cadherin-based junctions and myosin activity. An active polar gel model with inter-cellular contractility was used to investigate the physical mechanism. The authors interpreted the experiments in terms of active polar forces pointing outwards to the cell cluster drives the cells to move outwards, helping them to spread out and develop wetting. However, the contractility among cells drags cells inwards and prevents wetting.

The contractility and polar forces not only compete but can also appear to collaborate in other experiments. An example is collective durotaxis, the ability of cells to move up the stiffness gradient of the substrate. Durotaxis for individual cells is developed because cells form protrusions more significantly on a stiff substrate than on a soft substrate. Interestingly, multi-cellular scale, collective durotaxis has been observed in cases where isolated cells do not perform durotaxis [37]. Perturbations on $\alpha-$catenin molecules, a protein linking cadherin junctions and actin filaments, inhibits the collective durotaxis, showing that inter-cellular contractility is essential for this effect. The mechanism suggested, on the basis of experiments and accompanying modelling, is that the magnitude of traction at the two edges is equal, but the substrate on the soft edge deforms more than the stiff edges. As the tissue spans a scale much larger than a single cell, the stiffness varies significantly between the two edges, leading to a difference in substrate deformation more significant than a single cell can experience. Moreover, the contractility drags the cells behind the cells at the edges. Therefore, the tissue centre shift toward stiffer regions of the substrate, leading to the collective durotaxis.

A good way to understand cell mechanics is by implementing physical models which allow independent analysis of each component of the physical forces using computational or analytical approaches.

1.3 Physical models for collective cell motion

Several physical models have been built to investigate the underlying mechanisms of collective cell motions. In-silico models resolving individual cells have been applied to study tissue morphogenesis [38], wound healing [18] and tissue expansion [39]. Here, we briefly discuss some of the cellular-level models. The introduction of physical models from the cellular to continuum level can be found in [40].

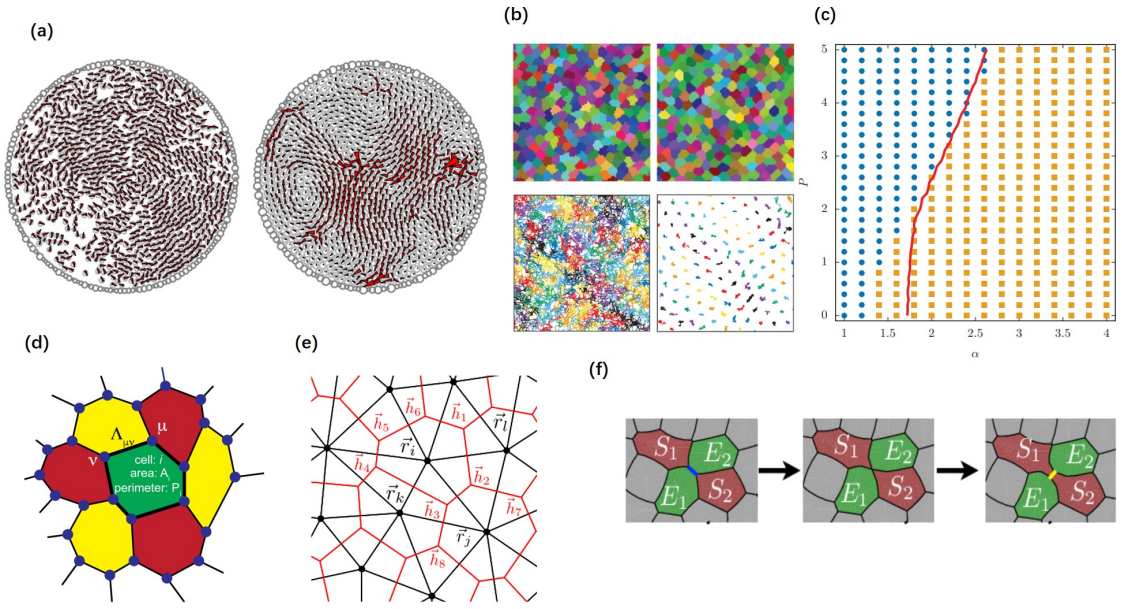


Figure 1.6: (a) **Disk model**: the jamming transition from an active polar liquid (left) to a jammed solid (right) by increasing the packing fraction in the disk model. The velocity of each cell is shown by the red arrows. **Cellular Potts Model**: (b) Simulation snapshots of a glassy state (upper right) with strong interfacial energy and a liquid state (upper left) with low interfacial energy in the cellular Potts model with active polar force. Neighbouring cells are labelled with different colours. The two subfigures at the bottom show the trajectories of cells corresponding to the glassy and liquid states. (c) The transition between the glassy state and the liquid state with respect to the interfacial tension, α, and the magnitude of the polar force, P. The regions in blue and yellow indicate the liquid state and the glassy state respectivly. **Vertex model and active Voronoi model** (d) A schematic of the vertex model. Cells are composed of a polygon with vertices labelled by blue dots. Each cell i is subject to an area (A_i) and perimeter constraint (P_i).The line tension between junction μ and ν is $\Lambda_{\mu\nu}$. (e) The network of Delaunay triangulation (black lines) is constructed by the centre of mass of cells $\vec{r}_i$. The Voronoi tessellation (red lines) represented by vertices $\vec{h}_i$ is developed from the Delaunay triangulation. (f) Left: a T1 transition is triggered when the edge (blue) length is shorter than the threshold. E1 and E2 are neighbours at this stage, but S1 and S1 are not. Middle: The intermediate state of a T1 transition. Right: After the T1 transition, S1 and S2 are neighbours, but E1 and E2 are not. (a), (d), (e) and (f) are adapted from [41], [42], [43] and [44] respectively. (b) and (c) are adapted from [45]

1.3.1 Disk model

Modelling cells as non-deformable disks or spheres is a straightforward way to study cell dynamics. Pairwise potential functions model the steric and adhesive interaction between disks. These models are efficient in studying the polarity of cells but focus less on the cell shapes. Angular relaxation processes can model polarisation dynamics such as CIL and polarisation-velocity alignment. For example, the jamming-to-unjamming transition as the packing fraction decreases is successfully modelled with polarisation-velocity alignments (Fig. 1.6(a)) [41]. Cells rotate collectively in circular confinement at low densities and jam at high densities. It has been shown in disk particle models that the competition between CIL alignment and noise gives rise to different states, ranging from a solid state and liquid state to a collective clustering state [46]. However, these models always neglect the information on how cell shape variation impacts the collective cell motion.

1.3.2 Cellular Potts model

Cellular Potts model was introduced by Graner and Glazier to study cell sorting by differential adhesion between different cell types [47, 48]. In these models, each lattice site i is assigned an index, $\sigma_i = 1...N$ for N cells. The index $\sigma_i = N+1$ represents the substrate. The Hamiltonian which models the cell-cell and cell-substrate interactions is

$$\mathcal{H} = \sum_{(i,j)} \alpha(1 - \delta_{\sigma_i,\sigma_j}) + K_a \sum_{\sigma=1}^{N} (A_\sigma - A_0)^2 - P \sum_{\sigma=1}^{N} \mathbf{X}_\sigma^{com} \cdot \mathbf{p}_\sigma.$$

The first term is the interfacial energy with the control parameter α between neighbouring cells where (i,j) labels neighbouring lattice sites. The interaction between cell and substrate ($\sigma = N+1$) is also included. The second term is an area constraint where $A_\sigma = \sum_i \delta_{\sigma_i,\sigma}$ is the area of cell σ, K_a is the area modulus and A_0 is the targeted area. The last term models the cell polarisation where $\mathbf{X}_\sigma^{com} = \sum_i \mathbf{x}_i \delta_{\sigma_i,\sigma}/A_\sigma$ is the centre of mass for cell σ. This term leads to a polar force $\mathbf{F}_\sigma^{polar} = P\ \mathbf{p}_\sigma$ where P and $\mathbf{p}_\sigma$ are the polar force magnitude and the polar vector for cell σ respectively. The system evolves in Monte-Carlo steps. Note that

an active polar force is included in the Hamiltonian, but its angular dynamics must be separately specified [40, 45]. These models have been applied to study the glassy state of cells. Fig. 1.6(b) shows a glassy state with strong interfacial energy and a liquid state with low interfacial energy for the cellular Potts model with an active polar force. Fig. 1.6(c) shows the transition between the glassy state and the liquid state with respect to the interfacial tension, α, and the magnitude of the polar force, P. The cellular Potts model has been extended to three-dimension and applied to study tumour growth and tumour invasion [49].

The cellular Potts model is able to describe cell shape and cell-cell adhesion relying on cell-cell contact. However, the maximum speed of cells in the model is limited by the Monte Carlo steps [49]. Also, the Monte Carlo process which depend on an artificial temperature parameter cannot be easily mapped to biological or physical measurements. How to include cell-cell interactions such as dipolar, nematic interactions in the cellular Potts model with Monte Carlo relaxations is also obscure.

1.3.3 Active vertex model and Voronoi model

In vertex models, cells are defined by polygons composed of vertices (Fig. 1.6(d)). The positions of vertices are taken as the degrees of freedom for the dynamics. The total energy is defined in terms of cell areas and perimeters, thus modelling the area constraint, cell-cell adhesion and cortex tension:

$$E = \sum_{c=1}^{N} [\frac{\kappa}{2}(A_c - A_0)^2 + \frac{\Gamma}{2}(P_c - P_0)^2] \tag{1.1}$$

where A_c and P_c are the area and perimeter of cell c respectively. A_0 and P_0 are the target area and perimeter. κ and Γ are control parameters for the area and perimeter constraint. The corresponding forces for each vertex are the derivatives of the total energy with respect to their positions $\mathbf{F}_i = -\nabla_{\mathbf{r}_i} E$.

In Voronoi models, the centres of cells are the degree of freedom, and the tissue is defined by a Voronoi tessellation developed from the centres of the cells (Fig. 1.6(e)). The total energy shares the same form as the vertex model. Active polar forces can be added to both models in a way similar to the particle-based

model. A force balance in an over-damped regime is typically chosen. To allow neighbour exchange events, T1 transitions are triggered when the length of an edge is smaller than a given threshold (see Fig. 1.6(f)).

Active vertex and Vornoi models that incorporate cell shape and motility are versatile and practically useful for studying polarisation dynamics and shape anisotropy during collective cell motions. How cell motility gives rise to a solid-to-liquid transition was studied using the self-propelled Voronoi model by Bi et al. [43]. The critical shape index (the mean value of the square root of cell areas over cell perimeters) $q* = 3.81$ for this transition has been shown to agree with cell experiments [50]. These models also allow differentiation in cell properties between different cell types or interactions between different species. They have been used to study how the differential tension between tissues shapes their boundaries [51]. The vertex model is also able to describe cells confined in different geometries. It has been applied to study the collective tissue elongation after an external stretch for a circular cluster of cells [52].

However, most of these models are only suitable for describing the confluent cell layers without gaps in the tissue. A modified Voronoi mode has been introduced to resolve this restriction [53]. Anisotropic nematic stress is typically not included in these models, but recent works have tried to address this [52]. Moreover, neighbour exchange events implemented by T1 transitions in the vertex model occur instantaneously once triggered. Such T1 transitions may not be physical since all biological and physical process has a finite time scale. By introducing a relaxation time for T1 transitions, more physical neighbour exchange events have been implemented in [54].

1.4 Overview of the thesis

This thesis studies polar and dipolar forcing in cell monolayers using a computational phase-field approach. Here, we briefly describe the contents of the thesis.

In Chapter 2, we introduce the active nematic theory, including the concept of the nematic order parameter and half-integer defects, and how the active stress

is derived from the active dipolar forces. Also, we discuss how the theories can be applied in our research on confluent cell layers.

In Chapter 3, we introduce the phase field model, an alternative model for cell motility. In contrast to disk models, which assume that cells are hard disks, the model is built on soft, deformable particles. We explain how to incorporate active polar and dipolar force densities into the model.

In Chapter 4, we investigate the interplay between the polar and dipolar contributions and compare the dynamics of a cell sheet when the polarity of the cells aligns to (i) their main axes of elongation, (ii) their velocity and (iii) when the polarity direction executes a persistent random walk. We find a transition from a jammed state to a liquid state occurs when either the polar or the dipolar activities are increased. In addition, we observe a flocking state for case (ii) only. The flocking state emerges with strong polar forces but disappears as the strength of the dipolar nematic activity increases.

In Chapter 5, we investigate the effects of the active contractile forces pulling on the cell junctions within a confluent layer of cells. Surprisingly, we find that the active, contractile, inter-cellular interactions lead to cell elongation, nematic ordering, and active turbulence. Extensile inter-cellular interactions, by contrast, result in frustration, and perpendicular cell orientations become more prevalent. Thus, our results provide a theoretical understanding of the collective nematic behaviour of deformable cells. Furthermore, we make the experimentally testable prediction that contractile behaviour can be changed to extensile behaviour by anisotropic fluctuations of inter-cellular forces.

In Chapter 6, we study the interplay between the passive properties and the inter-cellular forces for cells confined in a channel with a parallel anchoring condition. Such a configuration is a useful test system to study nematic features. We find a crossover from a collective oscillation state to a bidirectional shear flow by either increasing the negative surface tension-like cell-cell adhesion or the aspect ratio of cells, indicating a change from an elasticity-dominated regime to viscosity-dominated regime.

In Chapter 7, we summarise our results and discuss possible future research directions.

2

Active nematic theory

Before discussing the phase field model, we first introduce active nematic theory which is closely related to how we model the dipolar, nematic stress in the phase field model and the motion of active half-integer defects in confluent cell monolayers.

Elongated active particles with hydrodynamic interactions are called wet active nematic systems. A coarse-grained, continuum, active nematic theory has been applied to study the dynamics of bacterial swimmers and suspension of microtubles [4, 21]. More recently, this theory has also been applied to study the dynamics of confluent cell monolayers by treating elongated cells as nematic particles [12, 22], showing that the nematic features of cells may be described by wet active nematic theory. Moreover, active nematic stress has been applied in phase field simulations to investigate the role of inter-cellular interactions [13, 55–57]. Thus, we start this chapter with a general introduction to nematic liquid crystals and how dipolar forces in a low Reynolds number medium give rise to active stress. As discussed in Chapter 1, topological defects are often observed in confluent cell monolayers. They are essential in understanding the dynamics of active nematics. We describe the active stress induced motility of half-integer defects and how the motile defects are related to the ones observed in the experiments.

2.1 Liquid crystals

The states of matter can be classified based on the order of the system. Conventionally, solids have periodic crystal structures with long-range positional order (Fig. 2.1 (a)). Liquids are isotropic and disordered states (Fig. 2.1 (b)). By contrast, a liquid crystal is a state of matter between the liquid state and the solid state, which does not have positional order in all three dimensions but can show order in the orientations of the molecules. Materials in the liquid crystal state can show solid-like features such as elasticity and also liquid-like features such as fluidity [58]. Since they were reported in 1888 [59], liquid crystals has been studied extensively because their interesting symmetry properties and because of applications in display [58, 60].

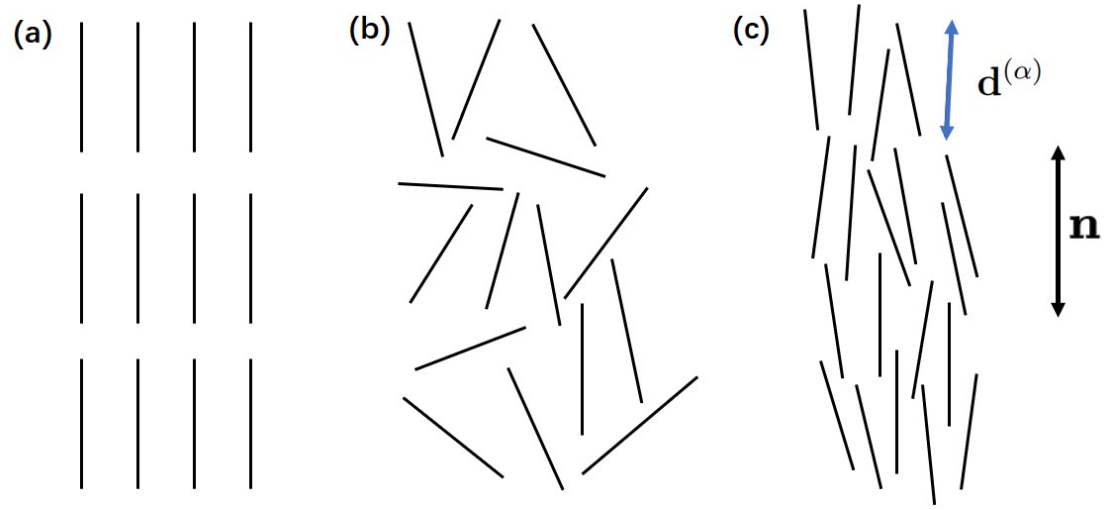


Figure 2.1: Schematics showing ordering in a solid (a), liquid (b) and nematic (c) phase. $\mathbf{n}$ is the nematic director, $\mathbf{d}^{(\alpha)}$ shows the long axis of nematic particle α

The type of liquid crystal that we are interested in is a nematic liquid crystal composed of long and thin rod-like particles. There are many examples of long and thin molecules such as para-Azoxyanisole. These particles align to their neighbours at a low temperature or high concentration, showing long-range orientational order. This orientation is described by the nematic director $\mathbf{n}$ which gives average elongation direction of a collection of nematogens (Fig. 2.1 (c)).

2.2 Nematic order parameter

As the rod-like particles are, on average, aligned along $\mathbf{n}$, we can define a scalar q to measure how good this alignment is. However, it is more convenient to specify a tensor order parameter which contains the information of both $\mathbf{n}$ and q. If the orientation of an individual rod-like particle α is described by a vector $\mathbf{d}^{(\alpha)}$ along its long axis, the order parameter can be defined as

$$\mathbf{Q} = \frac{1}{N}\sum_{\alpha}\mathbf{d}^{(\alpha)}\mathbf{d}^{(\alpha)} - \frac{1}{d}\mathbb{I} \tag{2.1}$$

where N is the number of particles, d is the dimension of the system, and $\mathbb{I}$ is the identity matrix. Note that $\mathbf{Q}$ is traceless (Tr $\mathbf{Q} = 0$) and symmetric ($\mathbf{Q} = \mathbf{Q}^T$). It quantifies the phase of the liquid crystal [61]. In an isotropic phase, $\mathbf{Q} = \mathbf{0}$. In a three-dimensional nematic phase where all the particles are perfectly aligned along the z-axis, $\mathbf{Q} = \mathrm{diag}(-1/3, -1/3, 2/3)$. In a three-dimensional, uniaxial nematic material, the eigenvector with the largest eigenvalue lies along the director $\mathbf{n}$. The nematic order parameter can be written as

$$\mathbf{Q} = S(\mathbf{nn} - \frac{1}{d}\mathbb{I}). \tag{2.2}$$

S is a scalar related to the scalar order parameter q. One of the advantages of using this order parameter is that $\mathbf{Q}$ preserves the head-tail symmetry of the nematogens: $\mathbf{Q}$ is invariant with the exchange between $\mathbf{n}$ and $-\mathbf{n}$.

As we focus on modelling two-dimensional cell monolayers, we note that the nematic order parameter in two dimensions can be written as

$$\mathbf{Q} = S(\mathbf{nn} - \frac{1}{2}\mathbb{I}) = \frac{S}{2}\begin{pmatrix}\cos 2\theta & \sin 2\theta \\ \sin 2\theta & -\cos 2\theta\end{pmatrix} \tag{2.3}$$

where $\theta = \arctan(n_y/n_x)$ and $\mathbf{n} = (\cos\theta, \sin\theta)^T$. This equation allows us to directly link the evolution of $\mathbf{Q}$ to the angle of $\mathbf{n}$.

2.3 Active nematics

Active nematics describe a wide range of out-of-equilibrium systems composed of individual units with neamtic symmetry, such as epithelial cell layers, bacterial suspensions, and microtubule and kinesin motor mixtures. A critical difference between passive and active systems is the self-propulsion ability of the individual entities. Now we describe the active stress that results from the forces exerted by active nematic particles.

In the low Reynolds number limit, the forces exerted by a self-propelled particle on the Stokes fluid medium are equal and opposite because of Newton's third law [62]. In the far-field limit, the size of the particle is negligible, and it can be simplified as a point that generates a force dipole made of a pair of equal and opposite forces. Accordingly, we can define two types of nematic particles, extensile and contractile nematics, by their forces. For contractile particles, the dipolar forces point inwards along the long axis (Fig. 2.2(a)). For extensile particles, the dipolar forces point outwards along the long axis (Fig. 2.2(b)).

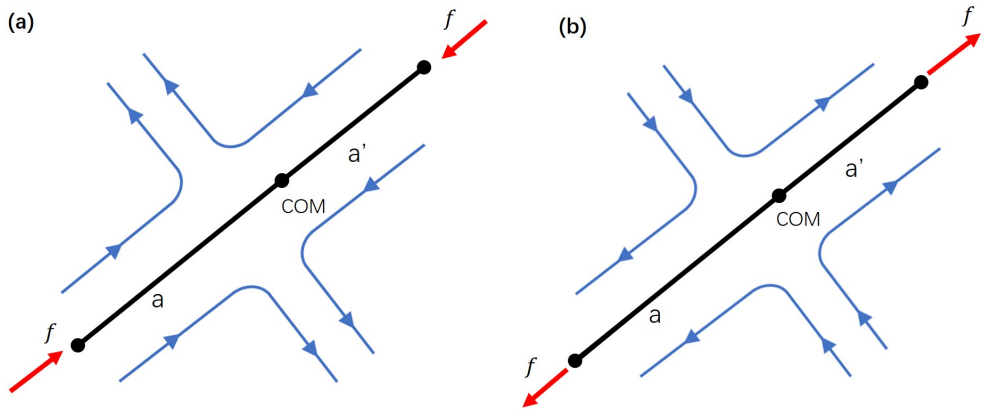


Figure 2.2: Schematic showing (a) a contractile particle exerting a pair of equal and opposite forces (red arrows) inwards along its long axis, (b) an extensile particle exerting a pair of equal and opposite forces (red arrows) outwards along its long axis. a and a' are the distance from the centre of mass (COM) to the two ends of the rod. The blue arrows show the flow field.

We can derive the active stress following the steps in [62]. We consider a collection of rod-like nematic particles with the centre of mass for particle α located at $\mathbf{r}^{(\alpha)}$. Each particle exerts a force dipole composed of two equal and opposite forces, $f\mathbf{d}^{(\alpha)}$ and $-f\mathbf{d}^{(\alpha)}$ along its long axis at $\mathbf{r}^{(\alpha)} - a\mathbf{d}^{(\alpha)}$ and $\mathbf{r}^{(\alpha)} + a'\mathbf{d}^{(\alpha)}$. The resultant force density for these particles is

$$\nabla \cdot \sigma^{act} = \mathbf{f}^{act} = f \sum_i \mathbf{d}^{(\alpha)}[\delta(\mathbf{r} - \mathbf{r}^{(\alpha)} + a\mathbf{d}^{(\alpha)}) - \delta(\mathbf{r} - \mathbf{r}^{(\alpha)} - a'\mathbf{d}^{(\alpha)})] \tag{2.4}$$

where σ^{act} is the active stress. For apolar particles $a = a'$. For polar particles $a \neq a'$.

The expansion of Eq. 2.4 around $\mathbf{r}^{(\alpha)}$ gives

$$\nabla \cdot \sigma^{act} \approx \frac{a + a'}{2} f \nabla \cdot \sum_\alpha \mathbf{d}^{(\alpha)}\mathbf{d}^{(\alpha)}\delta(\mathbf{r} - \mathbf{r}^{(\alpha)}) + O(\nabla\nabla) \tag{2.5}$$

By comparing this equation to the definition of the nematic director, we define a coarse-grained shear stress

$$\sigma^{act} = -\frac{a + a'}{2} f c(\mathbf{r})(\mathbf{nn} - \frac{\mathbb{I}}{3}) + O(\nabla) \tag{2.6}$$

where $c(\mathbf{r})$ is the concentration of the nematic particle. The term $\frac{a+a'}{2}$ shows that apolar and polar particles behave in the same way to the first order of the expansion. We can collect the prefactors into a single parameter ζ named the activity which measures the strength of the active stress.

$$\sigma^{act} = -\zeta \mathbf{Q} \tag{2.7}$$

ζ takes a positive value for extensile and a negative value for contractile activities.

2.4 Topological defects

Topological defects are discontinuities in the orientation field $\mathbf{n}$, which can form different structures such as point defects, disclination lines or walls in three-dimensional liquid crystals. As we aim to study the dynamics of cells in a two-dimensional monolayer, only point defects are discussed in this thesis. The charge of a topological defect is defined as

$$m = \frac{1}{2\pi} \oint_C d\theta \tag{2.8}$$

where C is a closed-path enclosing the defect core, and θ is the orientation angle of the director field $\mathbf{n} = (\cos\theta, \sin\theta)^T$. m shows how many times the director rotates around the defect core.

In general, the orientation angle of nematogens around a defect can be written as $\theta = m(\phi + \theta_0)$, where ϕ is the polar angle to the x-axis, and θ_0 is a constant offset angle. Fig. 2.3 shows the structures of topological defects with different charges. In two-dimensional nematic systems, half-integer defects predominate [21]. It is important to note that the emergence of the half-integer defects in the orientation field cannot be reconciled by smoothly rearranging the director field. It is only possible to remove these defects by creating and annihilating other defects under the constraint that the total charge is conserved [58].

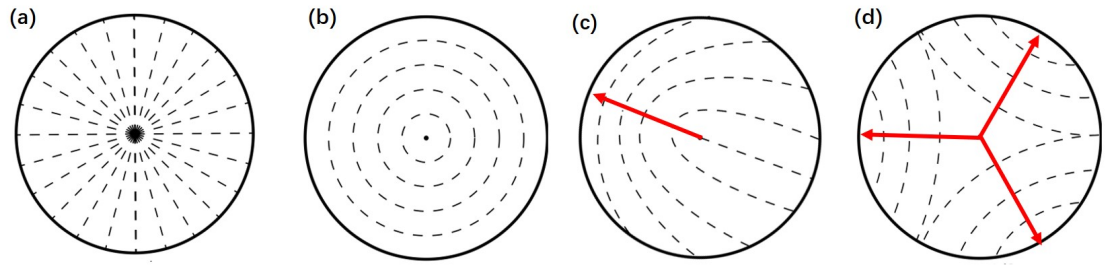


Figure 2.3: Directors (dashed black line) around defects for (a) an aster defect with m = 1, (b) a vortex defect with m=1, (c) a comet-like defect with m= +1/2 and (d) a trefoil-like defect with m = -1/2. The red arrows label the orientation of half-integer defects.

Moreover, the orientation of half-integer defects for two dimensional nematics can be measured by a unit vector $\mathbf{u} = (-\cos\psi, -\sin\psi)$. The orientation angle is

$$\psi = \frac{m}{1-m} \arctan\left[\frac{\langle \mathrm{sgn}(m)\partial_x Q_{xy} - \partial_y Q_{xx}\rangle}{\langle \partial_x Q_{xx} + \mathrm{sgn}(m)\partial_y Q_{xy}\rangle}\right], \tag{2.9}$$

where $\mathrm{sgn}(m)$ is the sign of the charge m, which takes the value +1 or -1, and $\langle\cdot\rangle$ denotes an average along the shortest available loop enclosing the defect core [63]. Because of the three-fold symmetry, the angle ψ for a 1/2 defect is uniquely defined in $-\pi/3 \leq \psi \leq \pi/3$. For a +1/2 defect, $\mathbf{u}$ points in its tail-to-head direction. In this thesis, we will keep this convention. The convention where the head-to-tail direction is defined as the +1/2 defect orientation may be used in other literature [63, 64].

2.4.1 Active half-integer defects

The motility of active nematic particles makes the properties of the defects different from their passive counterparts. This feature of active defects can be shown by the flow field around them. The flow field can be obtained by considering the active forces exerted on an incompressible, zero Reynolds number fluid. Thus, the velocity field, $\mathbf{v}$, obeys the following equations

$$\eta\nabla^2\mathbf{v} - \nabla p + \mathbf{f} = 0, \tag{2.10}$$

$$\nabla \cdot \mathbf{v} = 0 \tag{2.11}$$

where η is the viscosity, and $\mathbf{f} = \nabla \cdot \sigma^{act}$ is the active force density. The first line is the balance between viscous dissipation, the pressure gradient and the active force. The second line is the compressibility condition. The flow field can be calculated from the Green's function:

$$\mathbf{v}(\mathbf{r}) = \int d^2r' \mathbf{G}(\mathbf{r} - \mathbf{r}') \cdot \mathbf{f}(\mathbf{r}'). \tag{2.12}$$

For a two-dimensional infinite system where the velocity decays to zero as $\mathbf{r} \to \infty$, the Green's function is called the two-dimensional Oseen tensor [65].

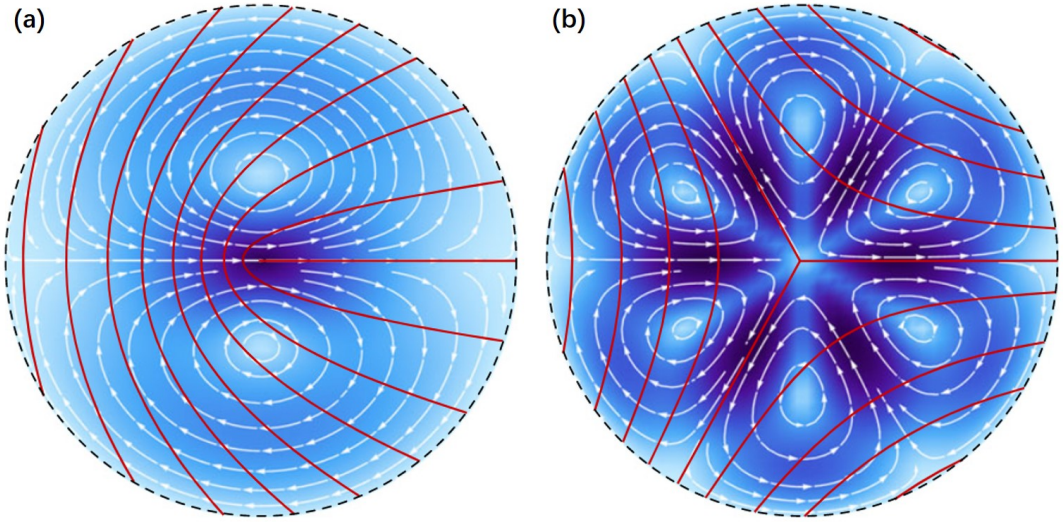


Figure 2.4: The director fields and velocity fields around (a) +1/2 and (b) -1/2 defects for a contractile system. The intensity of the blue background indicates the magnitude of the local velocity. Both (a) and (b) are adapted from [66].

Following [66], the active force density calculated from the active stress (Eq. 2.7) around half-integer defects where $\mathbf{n} = (\cos m\theta, \sin m\theta)$, $m = \pm\frac{1}{2}$, is

$$\mathbf{f} = -\frac{\zeta}{2r}\begin{cases}\hat{\mathbf{x}}, & m = +\frac{1}{2} \\ -\cos(2\theta)\hat{\mathbf{x}} + \sin(2\theta)\hat{\mathbf{y}}, & m = -\frac{1}{2}\end{cases} . \tag{2.13}$$

Substituting this active force into Eq. 2.12 gives the flow field

$$\mathbf{v}_{+1/2}(r,\theta) = -\frac{\zeta}{12\eta}\{[3(R-r) + r\cos 2\theta]\hat{\mathbf{x}} + r\sin 2\theta\hat{\mathbf{y}}\} \tag{2.14}$$

and

$$\mathbf{v}_{-1/2}(r,\theta) = -\frac{\zeta r}{12\eta R}\{[(\frac{3}{4}R - r)\cos 2\theta - \frac{R}{5}\cos 4\theta]\hat{\mathbf{x}} + [(\frac{3}{4}R - r)\sin 2\theta + \frac{R}{5}\sin 4\theta]\hat{\mathbf{y}}\} \tag{2.15}$$

for +1/2 and -1/2 defects respectively, where R is the size of the confining domain. At the defect core, $\mathbf{v}_{+1/2}(r=0,\theta) = -\frac{\zeta R}{4\eta}\hat{\mathbf{x}}$ and $\mathbf{v}_{-1/2}(r=0,\theta) = \mathbf{0}$, showing that +1/2 defects self propel along their symmetrical axis, but -1/2 defects do not. Note that the symmetry of the flow field around the defects does not vary with the boundary conditions [66], implying that self-motility is an intrinsic property for +1/2 defects.

The wet active nematic theory which models the dynamics of coarse-grained, continuous nematic order parameter field in viscous Stokes media, has been applied to study the dynamics of active defects in a confluent monolayer of epithelial cells [12]. For extensile and contractile particles, a +1/2 defect moves actively along its tail-to-head and head-to-tail direction respectively. This difference in the motility of +1/2 defects provides us with a possible method to identify whether a cell colony is extensile or contractile. It is technically challenging to study the active stress in a confluent cell monolayer in experiments, but a method relying on tracking the defect motion is possible because the only information needed is the cell orientations which can be obtained by applying a structure tensor method to contrast images of cells [8, 12, 67]. For example, C2C12 cells can be identified as contractile as the +1/2 defects move along their head-to-tail direction. However, the tail-to-head motion of defects in an NPC cell monolayer suggests that they are extensile [8]. Another interesting result is that the direction of motion of +1/2 defects changes

after E-cadherin based cell-cell junctions are knocked out in MDCK monolayers, implying that the behaviour changes from extensile to contractile [13]. We will investigate the properties of active defects in confluent cell monolayers using the phase-field model and propose that the change from extensive to contractile may be caused by anisotropic fluctuations of the nematic director.

3
Phase Field Model

Contents

3.1 Phase field dynamics 28
3.2 Passive forces 29
3.3 Active forces 33
3.3.1 Polar force 33
3.3.2 Dipolar forces: self elongation and inter-cellular forces . 36
3.4 Implementation of the model 40
3.5 Recent progress in modelling cells using the phase field model 40

A competent physical model should be able to capture the critical properties of cell behaviours, such as cell deformation and motility. We can introduce a computational phase field model to study the collective behaviour of cells. The phase field model allows single-cell properties, such as cell deformability or cell polarity and inter-cellular interactions, to be varied independently. Technically, it is convenient to couple complicated force densities into the phase field model because force is defined on each lattice site, allowing flexibility in its implementation. For example, a dipolar force can be distributed over the cell, controlling cell deformation. The ability to model deformable, soft cells and modify force distribution on cells makes the phase field model an attractive option for cell mechanics simulations.

In this chapter, we first discuss the equation of motion for the phase fields

and how the passive forces take part in the dynamics. Then, we discuss how we model polar and dipolar contributions to the active forces. Finally, we review recent progress in modelling cells using phase field methods.

3.1 Phase field dynamics

The phase field method was initially designed for studying the interfacial dynamics in solidification [68]. It also has been used to investigate various process in material science such as the stress-induced instability in liquid-solid interface [69], morphological and microstructure evolution [70], fracture mechanics [71–73], liquid metal dealloying [74, 75] and radiation damage in nuclear materials [76]. By incorporating the dynamics of fluids, it has been applied in studying the morphology of biological vesicles [77, 78] and cells [79]. These applications have demonstrated that the phase field method is flexible and versatile in modelling different systems.

In the spirit of the dynamics of binary or multi-phase fluids [80], each cell i is described by a phase field $\varphi^{(i)}$ which takes values 1 and 0 inside and outside the cell. At the interface of each cell, $\varphi^{(i)}$ changes continuously from 1 to 0. The motion of each phase field is governed by a local velocity field, $\mathbf{v}^{(i)}(\mathbf{x})$, according to the equation of motion

$$\partial_t \varphi^{(i)}(\mathbf{x}) + \mathbf{v}^{(i)}(\mathbf{x}) \cdot \nabla \varphi^{(i)}(\mathbf{x}) = -J_0 \frac{\delta \mathcal{F}}{\delta \varphi^{(i)}(\mathbf{x})} \tag{3.1}$$

where $\mathcal{F}$ is a free energy functional, and $-J_0 \frac{\delta \mathcal{F}}{\delta \varphi^{(i)}(\mathbf{x})}$ describes the dissipation relaxation dynamics of the cells to a free energy minimum at a rate J_0. The Reynolds number of cells is typically $\sim 10^{-4}$, so the dynamics are over-damped, and the velocity $\mathbf{v}^{(i)}(\mathbf{x})$ of a cell is determined by a local force density,

$$\xi \mathbf{v}^{(i)}(\mathbf{x}) = \mathbf{f}^{(i)}_{\text{tot}}, \tag{3.2}$$

where ξ is a friction coefficient and $\mathbf{f}^{(i)}_{\text{tot}}$ is the total force exerted on cell i. We consider two contributions to the force acting on each cell, $\mathbf{f}^{(i)}_{\text{tot}} = \mathbf{f}^{(i)}_{\text{passive}} + \mathbf{f}^{(i)}_{\text{active}}$, a passive force accounting for equilibrium cell properties such as compressibility, deformability, and the strength of cell-cell repulsion, and an active force describing polar or dipolar contributions of the activity.

3.2 Passive forces

The passive force stems from an effective free energy; if a cell deviates from equilibrium, the passive thermodynamic force will drive it towards a lower free energy state. We write the free energy as $\mathcal{F} = \mathcal{F}_{\text{CH}} + \mathcal{F}_{\text{area}} + \mathcal{F}_{\text{rep}} + \mathcal{F}_{\text{adh}}$ [55, 56]. The first contribution, defined as

$$\mathcal{F}_{\text{CH}} = \sum_i \frac{\gamma}{\lambda} \int d\mathbf{x} \left\{ 4\varphi^{(i)}(\mathbf{x})^2 (1 - \varphi^{(i)}(\mathbf{x}))^2 + \lambda^2 [\nabla \varphi^{(i)}(\mathbf{x})]^2 \right\}, \tag{3.3}$$

is a Cahn-Hilliard free energy that encourages $\varphi^{(i)}$ to take values 1 or 0 inside or outside a cell. $[\nabla \varphi^{(i)}]^2$ term models the surface tension between the two phases (Fig. 3.1(a)) . It is motivated by the theory of binary fluid phase separation [80]. We choose to locate the cell boundary at $\varphi^{(i)} = 1/2$, and it has width $\sim \lambda$, set by the gradient term. γ/λ is an energy scale. The Cahn-Hilliard free energy controls the deformability of individual cells.

To estimate the interface width, we consider a one-dimensional phase field $\varphi(x)$. The equilibrium profile of φ, which minimises the Cahn-Hilliard free energy, is obtained by setting its functional derivative to 0.

$$\frac{\delta \mathcal{F}_{CH}}{\delta \varphi} = \frac{8\gamma}{\lambda} \varphi(1 - \varphi)(1 - 2\varphi) - 2\gamma\lambda \frac{d^2\varphi}{dx^2} = 0.$$

Assuming boundary conditions $\varphi(x \to -\infty) = 1, \varphi(x \to +\infty) = 0$ gives

$$\varphi(x) = \frac{1}{2}(1 - \tanh \frac{x}{\lambda}).$$

This result shows that the Cahn-Hillard energy leads to a "tanh" interfacial profile with an interfacial width 2λ (Fig. 3.1(b)). Although cell-cell interactions change the interface profile of cells, the interfacial width $\sim \lambda$ remains a good approximation.

The interfacial width of a phase field is important as it not only measures the sharpness of the cell boundaries but is also related to interfacial interactions between cells. Cells with very sharp interfaces allow only a small amount of cell-cell overlap under steric interactions, behaving more like hard disks.

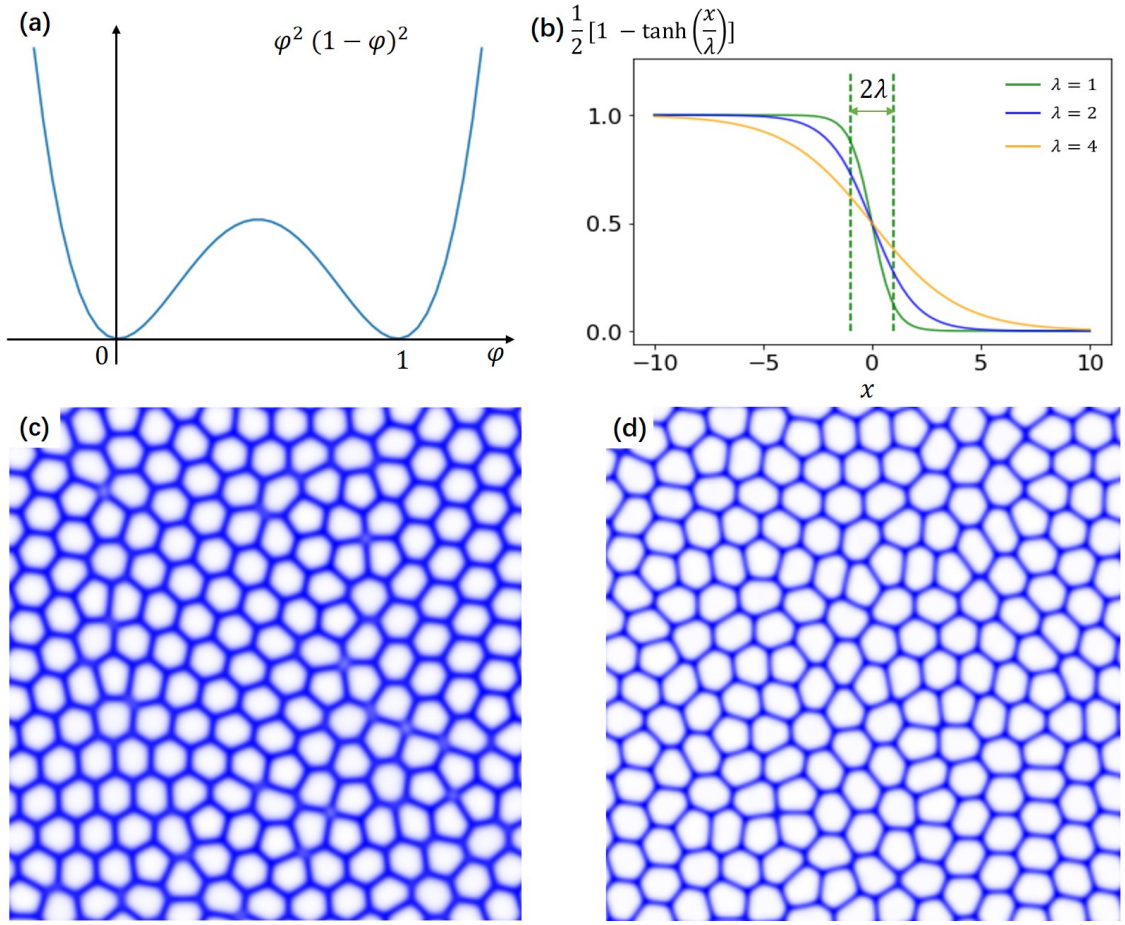


Figure 3.1: (a)The free energy favours $\varphi = 0$ or $\varphi = 1$. (b) The profile of the interface is obtained by minimising the Cahn-Hillard energy. Simulation snapshots for passive systems without cell-cell adhesion (c) and with strong cell-cell adhesion (d). In (d), the shape of individual cells becomes more elongated, and the interface is sharper compared to (c).

In addition to the cell deformability, we account for the cell compressibility using a free energy term

$$\mathcal{F}_{\text{area}} = \sum_i \mu \left\{ 1 - \frac{1}{\pi R^2} \int d\mathbf{x}\, \varphi^{(i)}(\mathbf{x})^2 \right\}^2, \tag{3.4}$$

which imposes a soft constraint of strength μ, restricting the area of each cell to πR^2. Therefore, in the absence of any active forces or cell-cell interactions, the cells will relax to circles.

The passive contributions to cell-cell interactions are introduced through repulsive and adhesive free energies as

$$\mathcal{F}_{\text{rep}} = \sum_i \sum_{j \neq i} \frac{\kappa}{\lambda} \int d\mathbf{x}\, \varphi^{(i)}(\mathbf{x})^2 \varphi^{(j)}(\mathbf{x})^2, \tag{3.5}$$

which penalises overlap between cells with an energy scale κ/λ, and

$$\mathcal{F}_{\text{adh}} = \sum_i \sum_{j \neq i} \omega\lambda \int d\mathbf{x}\ \nabla\varphi^{(i)} \cdot \nabla\varphi^{(j)}, \tag{3.6}$$

which is a term favouring cell-cell adhesion. Note that $\lambda \int d\mathbf{x} \nabla\varphi^{(i)} \cdot \nabla\varphi^{(j)}$ scales as the length of contact line between two cells and ω/λ is an energy scale. It is important to note that cell-cell adhesion makes the cell interface sharper.

Up to now we have discussed isotropic cells. However, fibroblasts are spindle-shaped cells that play a critical role in biological functions, such as wound healing. To model these naturally elongated cells, we define an additional term in the free energy to account for the aspect ratio.

$$\mathcal{F}_{shape} = K_g \sum_i [\varphi^{(i)}(\mathbf{x}) - e^{-(\mathbf{x}-\mathbf{x}^{(i)}_{com})^T \mathbf{A} (\mathbf{x}-\mathbf{x}^{(i)}_{com})}]^2 \tag{3.7}$$

where

$$\mathbf{A} = \frac{\mathbb{I} + 2\mathbf{Q}^{(i)}}{(R\sqrt{AR_0})^2} + \frac{\mathbb{I} - 2\mathbf{Q}^{(i)}}{(R/\sqrt{AR_0})^2} \tag{3.8}$$

and

$$\mathbf{Q}^{(i)} = \frac{1}{2} \begin{pmatrix} \cos 2\theta^{(i)}_n & \sin 2\theta^{(i)}_n \\ \sin 2\theta^{(i)}_n & -\cos 2\theta^{(i)}_n \end{pmatrix} \tag{3.9}$$

$\mathbf{x}^{(i)}_{com}$ is the centre of mass position of cell i. $\theta^{(i)}_n$ and the nematic director $\mathbf{n}^{(i)} = (\cos\theta^{(i)}_n, \sin\theta^{(i)}_n)^T$ models the long axis of the cell corresponding to the orientation of the stress fibres. This free energy forces the cell to elongate to the anisotropic Gaussian field along $\mathbf{n}^{(i)}$ with target aspect ratio AR_0. We apply this $\mathcal{F}_{shape}$ term only in Chapter 6 where we consider elongated cells. We remark that the Q-tensor is also related to the active dipolar stress of cells, and we will discuss more about this in Sec. 3.3.2.

We now show that the passive force is related to the variation of free energy. This relation is described by the virtual work principle. If we take an arbitrary and infinitesimal virtual displacement field $\delta\mathbf{r}(\mathbf{x})$ at the position $\mathbf{x}$, then the induced shift for each phase field is $\varphi^{(i)}(\mathbf{x}) \to \varphi^{(i)}(\mathbf{x} - \delta\mathbf{r})$. The induced change for each phase field is $\delta\varphi^{(i)} = \varphi^{(i)}(\mathbf{x} - \delta\mathbf{r}) - \varphi^{(i)}(\mathbf{x}) \approx -\delta\mathbf{r} \cdot \nabla\varphi^{(i)}$. The total free energy variation is

$$\delta\mathcal{F} = \sum_i \int d\mathbf{x} \frac{\delta\mathcal{F}}{\delta\varphi^{(i)}}\ \delta\varphi^{(i)} = -\sum_i \int d\mathbf{x} \frac{\delta\mathcal{F}}{\delta\varphi^{(i)}}\ \delta\mathbf{r} \cdot \nabla\varphi^{(i)}.$$

The virtual work due to the free energy variation is

$$\delta\mathcal{W} = -\delta\mathcal{F} = \sum_i \int d\mathbf{x} \frac{\delta\mathcal{F}}{\delta\varphi^{(i)}} \nabla\varphi^{(i)} \cdot \delta\mathbf{r}.$$

But the virtual work is, by definition, the dot product between the passive force density and the virtual displacement field. As a result, the passive force density is

$$\mathbf{f}^{(i)}_{\text{passive}}(\mathbf{x}) = \frac{\delta\mathcal{F}}{\delta\varphi^{(i)}} \nabla\varphi^{(i)}. \tag{3.10}$$

We list the functional derivatives that are used to calculate the passive force:

$$\frac{\delta\mathcal{F}_{CH}}{\delta\varphi^{(i)}} = \frac{8\gamma}{\lambda}\varphi^{(i)}(1-\varphi^{(i)})(1-2\varphi^{(i)}) - 2\gamma\lambda\nabla^2\varphi^{(i)}, \tag{3.11}$$

$$\frac{\delta\mathcal{F}_{area}}{\delta\varphi^{(i)}} = \frac{4\mu}{\pi R^2}\varphi^{(i)}[1 - \frac{1}{\pi R^2}\int d\mathbf{x}\ \varphi^{(i)}(\mathbf{x})^2], \tag{3.12}$$

$$\frac{\delta\mathcal{F}_{rep}}{\delta\varphi^{(i)}} = \frac{2\kappa}{\lambda}\sum_{j\neq i}\varphi^{(i)}(\mathbf{x})\varphi^{(j)}(\mathbf{x})^2, \tag{3.13}$$

$$\frac{\delta\mathcal{F}_{adh}}{\delta\varphi^{(i)}} = -\omega\lambda\sum_{j\neq i}\nabla\varphi^{(i)}(\mathbf{x})\cdot\nabla\varphi^{(j)}(\mathbf{x}) \tag{3.14}$$

$$\frac{\delta\mathcal{F}_{shape}}{\delta\varphi^{(i)}} = 2K_g[\varphi^{(i)}(\mathbf{x}) - e^{-(\mathbf{x}-\mathbf{x}^{(i)}_{com})^T\mathbf{A}(\mathbf{x}-\mathbf{x}^{(i)}_{com})}]. \tag{3.15}$$

Note that the relaxation term $-J_0\frac{\delta\mathcal{F}}{\delta\varphi^{(j)}}$ in Eq. 3.1 does not enter the passive force, because it models dissipation to the environment. As a result, J_0 is chosen to be a small number ($J_0 << \frac{1}{\xi\lambda^2}$) to make sure the passive dynamics dominate over the dissipation. Moreover, a strong cell-cell adhesion can leads to numerically unstable behaviour. To address this, we add a constraint function on the cell-cell adhesive force (see Appendix C for more details).

The passive dynamics should drive the system into a lower free energy state. This feature can be shown by calculating the time derivative of the free energy [81].

$$\begin{aligned}
\frac{d\mathcal{F}}{dt} &= \sum_j \frac{\delta\mathcal{F}}{\delta\varphi^{(j)}}\frac{\partial\varphi^{(j)}}{\partial t} \\
&= -\sum_j \frac{\delta\mathcal{F}}{\delta\varphi^{(j)}}[\mathbf{v}^{j)}(\mathbf{x})\cdot\nabla\varphi^{(j}(\mathbf{x}) + J_0\frac{\delta\mathcal{F}}{\delta\varphi^{(j)}}] \\
&= \sum_j -\frac{1}{\xi}[\frac{\delta\mathcal{F}}{\delta\varphi^{(j)}}\nabla\varphi^{(j)}]^2 - J_0[\frac{\delta\mathcal{F}}{\delta\varphi^{(j)}}]^2 \leq 0
\end{aligned}$$

where we used Eq. 3.1 to get the second line and applied Eq. 3.2 and Eq. 3.10 to get the third line. Under the passive dynamics, an arrangement similar to hexagonal packing appears when the cell-cell adhesion is absent (Fig. 3.1 (c)). As the cell-cell adhesion increases, the shape of individual cells becomes more elongated on average, and the interface width of a cell decreases (Fig. 3.1 (d)). However, cells are active, self-motile systems, driven out of equilibrium by chemical processes. Therefore, we next describe how we account for active forces.

3.3 Active forces

Active forces model the ability of the cell to consume energy and do mechanical work on its environment, and they drive the system out of equilibrium. As we discussed in Chapter 1, cell motility is closely related to the actin-myosin activity. Here, we use a simplified model which overlooks the internal dynamics, such as how biochemical processes trigger the actin protrusion, but focus on describing the physical forces generated by these processes. Force densities can be decomposed into the superposition of different contributions by a multipole expansion approach. Among these contributions, polar and dipolar forces are of leading importance compared to higher order effects. We discuss each of them in the following sections.

3.3.1 Polar force

The active polar contribution models the force acting on an individual cell due to actin treadmilling. In this process, cells are polarised. Thus, we associate each cell with a polarisation vector $\mathbf{p}^{(i)} = (\cos\theta_p^{(i)}, \sin\theta_p^{(i)})$. The corresponding force density is distributed over the basal surface of the cell, which adhered to the substrate. To model this, we introduce a uniformly distributed force density over a cell acting in the direction of the cell polarisation, (Fig. 3.2(a)),

$$\mathbf{f}_{pol}^{(i)}(\mathbf{x}) = \alpha\varphi^{(i)}(\mathbf{x})\mathbf{p}^{(i)}, \tag{3.16}$$

where the coefficient α controls the strength of the polar force generated by individual cells. The most physical way to choose the direction of the polarisation vector $\mathbf{p}^{(i)}$

is unclear [40]. Therefore we compare the following possibilities with the aim of uncovering any differences in behaviour that might be observable in experiments:

- **aligning the polarisation with the velocity of the cell (*velocity*)**

  We assume that $\mathbf{p}^{(i)}$ relaxes towards the centre of mass velocity of cell i, $\mathbf{v}^{(i)}_{\mathrm{COM}}$. The alignment dynamics reads

  $$\frac{d\theta^{(i)}_p}{dt} = -J_{\mathrm{pol}}|\mathbf{v}^{(i)}_{\mathrm{COM}}|\angle(\mathbf{p}^{(i)}, \mathbf{v}^{(i)}_{\mathrm{COM}}) + D_{\mathrm{pol}}\ \eta^{(i)} \tag{3.17}$$

  where $\eta^{(i)}$ is a Gaussian noise with unit standard deviation and strength D_{pol}, $\angle(\mathbf{p}^{(i)}, \mathbf{v}^{(i)}_{\mathrm{COM}})$ is the signed angle from $\mathbf{v}^{(i)}_{\mathrm{COM}}$ to $\mathbf{p}^{(i)}$, chosen to lie in the interval $[-\pi, \pi)$ and J_{pol} controls the rate of alignment. Fig. 3.2(b) shows the schematic of this polarisation alignment scheme. This form of the polarity alignment is motivated by considering the cell-substrate interaction which, in the over-damped dynamics of the cell motion, can favour the alignment of polarity to the cell velocity [49, 82]. While some experiments have reported mis-alignment of polarity and velocity [33, 83], a recent study has shown that such an alignment occurs, albeit with a well-defined time delay [84].

- **aligning the polarisation with the cell elongation (*shape)***

  To quantify the cell elongation, we first calculate the deformation tensor that quantifies the shape of a cell.

  $$\begin{aligned}\mathcal{D}^{(i)} &= -\int d\mathbf{x}\left\{\nabla\varphi^{(i)}\nabla\varphi^{(i)^T} - \frac{\mathbb{I}}{2}\mathrm{Tr}(\nabla\varphi^{(i)}\nabla\varphi^{(i)^T})\right\} \\ &= \sqrt{(\mathcal{D}^{(i)}_{xx})^2 + (\mathcal{D}^{(i)}_{xy})^2}\ (\mathbf{d}^{(i)}_{\parallel}\mathbf{d}^{(i)^T}_{\parallel} - \mathbf{d}^{(i)}_{\perp}\mathbf{d}^{(i)^T}_{\perp}) \\ &= 2\sqrt{(\mathcal{D}^{(i)}_{xx})^2 + (\mathcal{D}^{(i)}_{xy})^2}\ (\mathbf{d}^{(i)}_{\parallel}\mathbf{d}^{(i)^T}_{\parallel} - \frac{1}{2}\mathbb{I})\end{aligned} \tag{3.18}$$

  where $\mathbf{d}^{(i)}_{\parallel} = (\cos\theta^{(i)}_d, \sin\theta^{(i)}_d)^T$, $\mathbf{d}^{(i)}_{\perp} = (-\sin\theta^{(i)}_d, \cos\theta^{(i)}_d)^T$ and $\theta^{(i)}_d = \frac{1}{2}\arctan(\mathcal{D}^{(i)}_{xy}/\mathcal{D}^{(i)}_{xx})$. $\mathbf{d}^{(i)}_{\parallel}$ and $\mathbf{d}^{(i)}_{\perp}$ are the orthonormal eigenvectors of the $\mathcal{D}^{(i)}$ corresponding to the positive and negative eigenvalues, along and perpendicular to the elongation

axis of the cell respectively (see Appendix B for more details of the derivation). They are normalised so that $\mathbf{d}_{\parallel}^{(i)}\mathbf{d}_{\parallel}^{(i)^T} + \mathbf{d}_{\perp}^{(i)}\mathbf{d}_{\perp}^{(i)^T} = \mathbb{I}$. Then, the deformation tensor can be written as a nematic-like tensor (the third line of Eq. 3.18). We take the polarisation to relax towards $\mathbf{d}_{\parallel}^{(i)}$, the long axis of the cell,

$$\frac{d\theta_p^{(i)}}{dt} = -J_{\text{pol}} D^{(i)} \angle(\mathbf{p}^{(i)}, \mathbf{d}_{\parallel}^{(i)}) + D_{\text{pol}}\, \eta^{(i)}, \tag{3.19}$$

where $\angle(\mathbf{p}^{(i)}, \mathbf{d}_{\parallel}^{(i)})$ is the signed angle from $\mathbf{d}_{\parallel}^{(i)}$ to $\mathbf{p}^{(i)}$.

$D^{(i)} = 2\sqrt{(\mathcal{D}_{xx}^{(i)})^2 + (\mathcal{D}_{xy}^{(i)})^2}$ measures the deformation of a cell. Due to its head-tail symmetry there is a freedom for the choice of $\mathbf{d}_{\parallel}^{(i)}$ or $-\mathbf{d}_{\parallel}^{(i)}$. We choose the one that forms an acute angle with the polarisation ($\mathbf{d}_{\parallel}^{(i)} \cdot \mathbf{p}^{(i)} \geq 0$). Fig. 3.2(c) shows a schematic of this polarisation alignment scheme. This form of the polarity alignment, which follows from assuming that the internal acto-myosin machinery of the cell tends to align with the direction of the cell elongation, has been employed in a number of previous models [85, 86].

- **active Brownian motion (***Brownian)*

For comparison, we also simulate cell layers where the polarisation direction follows a persistent random walk,

$$\frac{d\theta_p^{(i)}}{dt} = D_{\text{pol}}\, \eta^{(i)}. \tag{3.20}$$

$\eta^{(i)}$ is Gaussian noise with unit standard deviation and strength D_{pol}. Fig. 3.2(d) shows the schematic of this polarisation alignment scheme. This form of the polarity alignment has been used in previous models [81, 87]. However, while the motion of cells in a tissue is undoubtedly subject to a considerable amount of noise, a purely stochastic alignment mechanism is debatable in the light of experimental studies that have directly evaluated cell polarity alignments in epithelial tissues [33, 83, 84].

Collective behaviour such as the jamming to unjamming transition and the flocking state can emerge from different polarization alignment schemes. We will discuss these effects in Chapter 4.

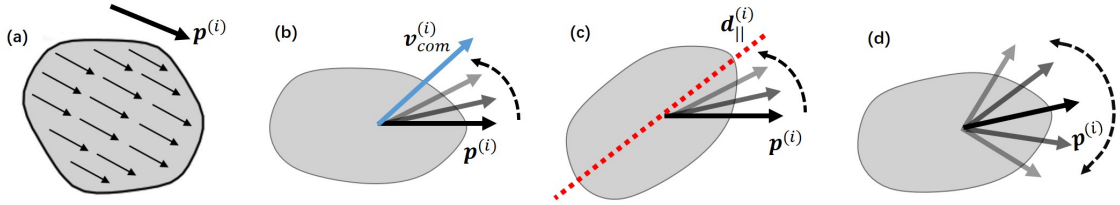


Figure 3.2: (a) Schematic for polar force density (the thin arrows inside the cell). The polarisation dynamics for the cells align to (b) their velocity (case: *velocity*), (c) their main axis of elongation (case: *shape*) and (d) when the polarity direction executes a persistent random walk (case: *Brownian*). The polarisation ,$\mathbf{p}^{(i)}$, centre of mass velocity ,$\mathbf{v}_{com}^{(i)}$, and the elongation axis ,$\mathbf{d}_{\parallel}^{(i)}$, of the cells are indicated by the black arrow, the blue arrow and the red dashed line respectively.

3.3.2 Dipolar forces: self elongation and inter-cellular forces

A single cell deforms when crawling on a substrate. This self-deformation stems from the activity of actin filaments, and it can be modelled by balanced, dipolar forces where the sum over all the forces is zero. As cells group together, cell-cell junctions are developed. The dipolar forces can be transmitted through cell-cell junctions, forming active inter-cellular forces.

To formulate the active contribution to the dipolar force density, we define a director, $\mathbf{n}^{(i)}$ associated with each cell i. It models the average orientation of the stress fibres inside cell i.

- **Aligning the nematic director with the cell elongation**

  A reasonable choice for the nematic director is $\mathbf{n}^{(i)} = \mathbf{d}_{\parallel}^{(i)}$ because actin filament tends to align to the elongation axis of cells [27]. Moreover, stochastic relaxation can be introduced in a model for this alignment, giving a more physical description.

$$\frac{d\theta_n^{(i)}}{dt} = -J_{\text{nem}} \angle(\mathbf{n}^{(i)}, \mathbf{d}_{\parallel}^{(i)}) + D_{\text{nem}}\, \eta^{(i)}, \tag{3.21}$$

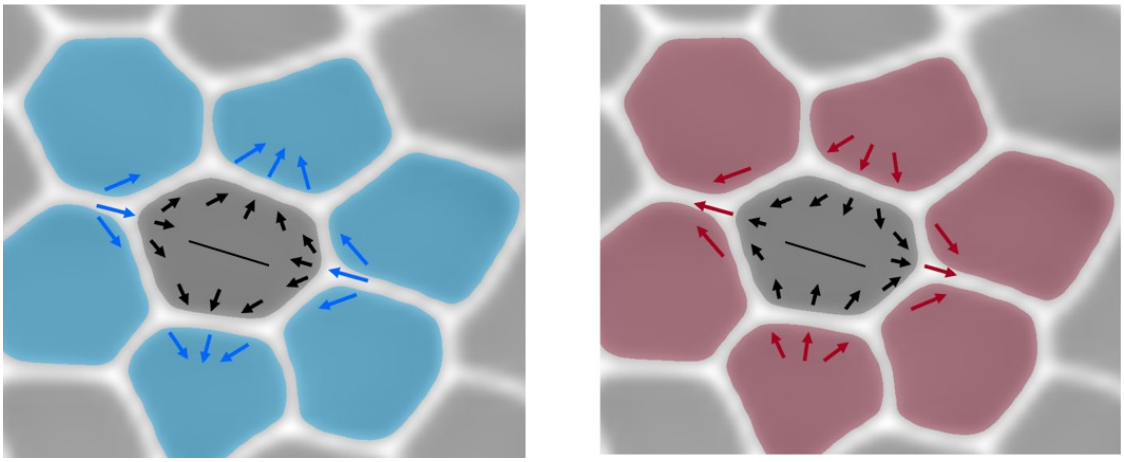


Figure 3.3: Left: Schematic for contractile inter-cellular (blue arrows) and contractile self-deformation (black arrows) force density. The inter-cellular contractile force is exerted on the neighbouring cells (cells in blue). **Right:** The schematic for extensile inter-cellular (red arrows) and extensile self-deformation (black arrows) force density. The centring cell exerts the inter-cellular extensile force on the neighbouring cells (cells in red). The black lines at the centre of the cells indicated the nematic directors.

where $\theta_n^{(i)}$ is the orientation angle for the nematic director $\mathbf{n}^{(i)} = (\cos\theta_n^{(i)}, \sin\theta_n^{(i)})$, and $\angle(\mathbf{n}^{(i)}, \mathbf{d}_\parallel^{(i)})$ is the signed angle from $\mathbf{d}_\parallel^{(i)}$ to $\mathbf{n}^{(i)}$. Due to the symmetry of $n^{(i)}$ and $\mathbf{d}_\parallel^{(i)}$, there is a freedom for the choice of $\mathbf{d}_\parallel^{(i)}$ or $-\mathbf{d}_\parallel^{(i)}$ and also $\mathbf{n}^{(i)}$ or $-\mathbf{n}^{(i)}$.We choose the one that forms an acute angle between the two (headless) vectors ($\mathbf{d}_\parallel^{(i)} \cdot \mathbf{n}^{(i)} > 0$). J_{nem} controls the time scale of the angular relaxation. $\eta^{(i)}$ is a Gaussian noise centred at zero with a unit standard deviation.

- **Anisotropic fluctuations of the nematic director around the cell elongation**

  In Eq. 3.21, $\mathbf{n}^{(i)}$ aligns to $\mathbf{d}_\parallel^{(i)}$ under a uniform rotational noise. However, the inter-cellular force can fluctuate not only orientationally but also in its magnitude. Moreover, the fluctuations of $\mathbf{n}^{(i)}$ can be anisotropic, as they depend on the distribution of the stress fibres. Thus, we can introduce another stochastic process to model these anisotropic fluctuations.

$$\frac{d\mathbf{n}^{(i)}}{dt} = J_n(\mathbf{d}_\parallel^{(i)} - \mathbf{n}^{(i)}) + \boldsymbol{\eta}^{(i)}(t) \tag{3.22}$$

where J_n controls the time scale of relaxation. We assume anisotropic, Gaussian noise, uncorrelated between cells, with

$$\begin{aligned} &\langle \boldsymbol{\eta}^{(i)}(t)\rangle = \mathbf{0}, \\ &\langle \boldsymbol{\eta}^{(i)}(t)\boldsymbol{\eta}^{(i)}(t')^T\rangle = \delta(t-t')(D_\parallel \mathbf{d}_\parallel^{(i)}\mathbf{d}_\parallel^{(i)^T} + D_\perp \mathbf{d}_\perp^{(i)}\mathbf{d}_\perp^{(i)^T}). \end{aligned} \tag{3.23}$$

The variance of the noise couples to the shape of the cell and can take different values for fluctuations along $\mathbf{d}_\parallel^{(i)}$ or $\mathbf{d}_\perp^{(i)}$. In this case, $\langle \mathbf{n}^{(i)}\rangle \approx \mathbf{d}_\parallel^{(i)}$ for time longer than the relaxation time scale of cell shape but the magnitude of $\mathbf{n}^{(i)}$ is not fixed in time.

For a eukaryotic cell, the internal stress fibre unit serves as the constitute nematic particle, and the nematic director for a cell is the average direction of these units. Thus, we can define the Q-tensor for a cell by

$$Q_{\alpha\beta}^{(i)} = \mathbf{n}_\alpha^{(i)}\mathbf{n}_\beta^{(i)} - \frac{|\mathbf{n}^{(i)}|^2}{2}\delta_{\alpha\beta}. \tag{3.24}$$

In the absence of any unbalanced active forces, the leading order contribution to the active stress acting on cell i is related to the nematic order parameter [62]. The coarse-grained active stress which account for cell deformation caused by its internal forces is

$$\sigma_{self}^{(i)} = -\zeta_{\text{self}}\ \varphi^{(i)}\mathbf{Q}^{(i)}. \tag{3.25}$$

As the cell-cell junctions transmit forces to neighbouring cells, the stress generated by cell j can act on its neighbouring cells with activity ζ_{inter}, this results in an inter-cellular stress acting on cell i,

$$\sigma_{\text{inter}}^{(i)} = -\zeta_{\text{inter}}\sum_{j\neq i}\mathbf{Q}^{(j)}\varphi^{(j)}. \tag{3.26}$$

So the total active, dipolar stress is

$$\sigma_{\alpha\beta}^{(i)}(\mathbf{x}) = -\zeta_{\text{self}}\ Q_{\alpha\beta}^{(i)}\ \varphi^{(i)}(\mathbf{x}) - \zeta_{\text{inter}}\sum_{j\neq i} Q_{\alpha\beta}^{(j)}\ \varphi^{(j)}(\mathbf{x}). \tag{3.27}$$

The nematic, dipolar force density is

$$\mathbf{f}_{\text{nem}}^{(i)} = \nabla \cdot \sigma^{(i)} \tag{3.28}$$

$$= -\zeta_{\text{self}}\, \mathbf{Q}^{(i)} \cdot \nabla\varphi^{(i)}(\mathbf{x}) - \zeta_{\text{inter}} \sum_{j\neq i} \mathbf{Q}^{(j)} \cdot \nabla\varphi^{(j)}(\mathbf{x}) \tag{3.29}$$

Note that there is no need to identify the neighbours of cell i in the summation in Eq. 3.29, because the advection term, $\mathbf{v}^{(i)} \cdot \nabla\varphi^{(i)}$, in Eq. 3.1 is nonzero only at the cell interface, and forces which are not generated by cell i or its neighbours vanish automatically in the dynamics of $\varphi^{(i)}$.

We distinguish between the stress acting on cell i due to internal forces, of strength ζ_{self}, and that due to other cells, of strength ζ_{inter}. Fig. 3.3 shows the self-deformation and inter-cellular components of contractile and extensile dipolar force density. The contractile force density contracts the cell itself along the direction of $\mathbf{n}^{(i)}$ and extends the cell along the perpendicular direction with strength $\zeta_{\text{self}} < 0$, and this contractile force can be further transmitted to the cell's neighbours with strength $\zeta_{\text{inter}} < 0$ (Fig. 3.3 **Left**). The self and inter-cellular extensile forces ($\zeta_{\text{self}} > 0$ and $\zeta_{\text{inter}} > 0$) works in a similar way but extend the cell along $\mathbf{n}^{(i)}$ (Fig. 3.3 **Right**). Biologically, ζ_{self} is linked to the activity of intracellular myosin motors whereas ζ_{inter} models the active pushing and pulling from neighbouring cells through cadherin-based cell-cell junctions. Therefore, ζ_{self} and ζ_{inter} are not necessarily the same.

It is reasonable to assume that inter-cellular forces can be the leading effect on cell dynamics in a confluent tissue. Extending the idea of contact inhibition of locomotion, cells in a confluent layer tend to reduce polarisation and the associated self-deformation forces because they have contacts on all sides. Other evidence that inter-cellular forces can be the leading effect on cell dynamics in a confluent tissue includes sub-cellular traction force measurements for MDCK cells, which show that the cell-cell forces surrounding the inner cells are stronger than their traction forces [88] and measurements showing that the traction stress in the middle of a cell colony nearly vanishes after the development of cell-cell junctions in a high calcium environment [89]. These observations show that inter-cellular forces can dominate over other contributions in a confluent cell monolayer.

3.4 Implementation of the model

To calculate the dynamics of the phase field, we use a finite difference method to calculate the spatial derivatives and the predictor and corrector method to update each phase field in time. The stochastic processes, such as Eq. 3.19, Eq. 3.17, Eq. 3.20, Eq. 3.21 and Eq. 3.22 are implemented using the Euler–Maruyama method. The details of these numerical methods are given in Appendix A. Measures, such as cell deformation and centre of mass velocities, are necessary for implementing the model. The details about these measurements are given in Appendix B.

3.5 Recent progress in modelling cells using the phase field model

Before focusing on our results, we summarise the literature on using the phase field approach to model cells. The dynamics of single-cell migration has been studied by treating cells as active polar droplets. The phase field dynamics are coupled to a continuous polar field, a vector field modelling the polarisation of actin filaments. These models can give a more detailed description of single-cell behaviour. For example, the shape and velocity oscillations of a single cell crawling has been modelled [90, 91]. Also, the three-dimensional shape of cell crawling for different cells can be controlled by changing the parameter for the contractility, the treadmilling rate and the anchoring between the polarisation and the gradient of the phase field [92].

The multicellular system where cells are represented as different phase fields was first modelled by Nonomura to study the effect of cell division and how cells respond to external forces [93]. In this work, the passive effects include volume constraints, cell-cell adhesion and steric repulsion, but the active forces are neglected.

The phase field model has been developed to incorporate self-propulsion and applied to study the elasticity mismatch between motile cells in a confluent cell monolayer. The model includes the translation velocity of each cell induced by passive forces and active cell motility. The passive free energy was modelled similarly

to [93]. Moreover, the authors assumed that cells move actively in the manner of a persistent random walk and thus model the active velocities by fixing their magnitude but allowing them to rotate randomly. The simulation results show that the elasticity mismatch between a soft cancer cell and the ordinary cells can significantly increase cancer cell motility. A similar model was applied in studying the solid-to-liquid transition and the overlap between cells [94].

A phase field model of motile cells with a phenomenological polarisation alignment scheme was developed to match the experimental results [84]. In the experiments, the polarisation was found to align with the traction of a cell, the force exerted by the substrate on the cell. This feature was investigated by adding stochastic orientational alignment between the polar force and the traction on top of a phase field model similar to the one in [81]. The simulation results showed that this polarisation mechanism can lead to a sustained oscillation in a confluent cell monolayer. However, various polarisation alignment schemes have been observed in experiments. In Chapter 4, we compare different possible polarisation mechanisms and their interplay with the dipolar forces using the phase field model.

In contrast to the coarse-grained multicellular models we described above, where the internal mechanisms are overlooked, efforts have been made to study the internal dynamics, such as the chemical and polarisation fields, using the phase field model. The condition of persistent rotational motion for a pair of cells has been investigated by introducing continuous scalar fields for Rho GTPase, a protein controlling actin dynamics, and a fluctuating inhibitor which controls the persistence of cell polarisation [95]. Moreover, the cell nucleus is modelled as an extra phase field inside the phase field representing the cell body in [95]. The simulation results show that the polarisation dynamics strongly influence the collective rotation, and the existence of nuclei makes the collective rotation more stable.

The approach that models a single cell as an active polar droplet has been extended to model multiple cells and applied to study collective cell migration. Löber et al. have reported that flocking and collective rotation states emerge in periodic boundary and circular confinements, respectively, and cell-cell adhesion

weakens these features. Moreover, the formation of multicellular moving bands and tissue-like structures appeared at intermediate and high cell densities [86]. Also, this model has been modified and applied in studying the hydrodynamic interactions of cells and the cellular structures in collective cell migrations [96, 97]. However, extra effort may be necessary to incorporate the cell-wise coordinated polarisation dynamics as we described in Chapter 1, Section 1.2.2 into these models.

As more and more observations suggest that nematic features are relevant in confluent cell layers, dipolar, nematic forces have been incorporated into the phase field dynamics. Mueller et al. have studied the emergence of half-integer defects in cell orientation for confluent cell monolayers by coupling a nematic stress to cell deformation [55]. The emergence of half-integer defects in the orientation field shows the features of active turbulence, a well-known characteristic of active nematics with hydrodynamic interactions. Moreover, the velocity field around the defects contains symmetric vortices, resembling the flow field around defects in active nematics. In Chapter 5, we decouple the inter-cellular and intra-cellular dipolar activity and investigate the effect of the inter-cellular force only. We also introduce the anisotropic fluctuations in inter-cellular forces and predict that contractile behaviour can be changed to extensile behaviour by such fluctuations. We further, in Chapter 6, investigate the interplay between passive properties and the active inter-cellular forces by confining cells in a channel by introducing walls.

4

Active dipolar and polar forces in collective cell motility

Contents

4.1 Introduction 43
4.2 Simulation method 44
4.3 Results 45
4.3.1 Unjamming 45
4.3.2 Cell deformations 48
4.3.3 Cell speed and flocking 51
4.4 Discussion 53

4.1 Introduction

In Chapter 1, we discussed that polar and dipolar forcing could give rise to different collective behaviours of confluent cell monolayers, such as the jamming-to-unjamming transition, flocking motion and active turbulence. However, the mechanisms behind the collective motion of cells are still unclear even though considerable theoretical understanding has been recently achieved using two-dimensional simplified model systems of confluent cell layers [14, 40]. In particular, the importance of dipolar forces and their interplay with cell polarity remain largely unknown. We use the phase field model of a confluent cell sheet to investigate

these questions and show how different forcing can lead to a range of collective cell behaviours: jamming, a liquid state, and flocking. We focus on the interplay between dipolar and polar contributions and compare the dynamics of a cell sheet when the polarity of the cells aligns to (i) their main axis of elongation, (ii) their velocity, and (iii) when the polarity direction executes a persistent random walk (Fig. 3.2 shows the schematic of these polarisation dynamics). We find out that increasing either the polar or the dipolar forces can give rise to a sharp liquid-to-jamming transition. For case (ii) only, a flocking (solid or liquid) state where most cells move in the same direction is observed. This state appears at strong polar forces but is destroyed as the strength of the dipolar activity is increased.

4.2 Simulation method

To simulate the collective behaviour of the confluent cell monolayer, we compute the dynamics of phase field using Eq. 3.1 and Eq. 3.2. The passive force (Eq. 3.10) and free energy (Eq. 3.3-3.6) excluding the $\mathcal{F}_{shape}$ term (Eq. 3.7) in Section 3.2 are applied. As we discussed in Section 3.3.1 , different polarisation dynamics are modelled by Eq. 3.17 (*velocity*), Eq. 3.19 (*shape*) and Eq. 3.20 (*Brownian*). We follow [55] and couple the dipolar stress to the cell deformation by setting $\mathbf{Q}^{(i)} = \mathcal{D}^{(i)}$. The polar and nematic force are calculated by Eq. 3.16 and Eq. 3.29 respectively. As the both the polarisation-induced self-deformation and inter-cellular interactions are presented in our simulations, we have $\zeta_{\text{inter}} \neq 0$ and $\zeta_{\text{self}} \neq 0$. For simplicity we use one parameter, ζ, for the dipolar activity and set $\zeta = \zeta_{\text{inter}} = \zeta_{\text{self}}$. As the MDCK cells show extensile behaviour [12], we choose extensile active stresses, $\zeta > 0$.

We simulate the dynamics of 233 cells of radius $R = 4$ in a periodic domain of size 108×108 in simulation units. Initially, cells with radius $R/2$ are placed randomly, but with the constraint that the distances of neighbouring centres $> 0.8R$. They are then relaxed for 2000 time steps under passive dynamics to reach confluence. The simulations then start with the randomly oriented polarisation of magnitude α. They are run for 30000 time steps, and data is collected after 10000 time

steps. Parameter values are $\lambda = 1.5$, $\gamma = 0.055$, $\kappa = 0.4$, $\mu = 6$, $\xi = 1$ and $D_{\mathrm{pol}} = 0.005$ unless otherwise specified.

Typically the average diameter of MDCK cells $\sim 10\mu m$, the velocity $\sim 20\mu m/h$, measured by Particle Image Velocimetry, and the pressure $\sim 100Pa$, measured by Traction Force Microscopy [12]. For these values, the simulation units can be mapped to physical units using $\Delta x \sim 1\mu m$ as the spatial interval, $\Delta t \sim 1s$ as the time step, and $\Delta F \sim 2.5nN$ as the force unit. The polarity alignment rate J_{pol} is chosen to give alignment on the time scale taken by a cell to translate through the size of a cell, 2R.

4.3 Results

In order to understand the role of active forces in collective cell dynamics, we focus on the interplay between dipolar active stresses, which are defined based on the cell deformations, and the active polar forces, proportional to the polarisation of each cell. The strength of the former is controlled by the parameter ζ, while the parameter α controls the latter. Fig. 4.1 shows pictorial examples of the simulation results which are summarised in the stability diagrams in Fig. 4.2. In Fig. 4.2(a) the polarisation of a cell aligns to its long axis (case *shape*) and there is an unjamming transition as either the polar or the dipolar forces are increased. Active Brownian dynamics of the polarisation (case *Brownian*) gives a very similar stability diagram (Fig. 4.2(c)). However, if the polarisation of a cell aligns to its velocity (case *velocity*) we obtain the stability diagram in Fig. 4.2(b). This shows a similar unjamming transition but also, for large polar forces, flocking where the cells move coherently in the same direction. We now describe the results in more detail.

4.3.1 Unjamming

A clear feature of the cell dynamics is the crossover from a jammed state, where for small active forcing the cells do not move relative to each other, to a liquid state, in which rearrangements can take place, as either the dipolar active stress ζ or the polar force α are increased. This is illustrated in Fig. 4.3(a),(b) where the trajectories of the cell centres are compared in typical jammed and liquid configurations. Similar

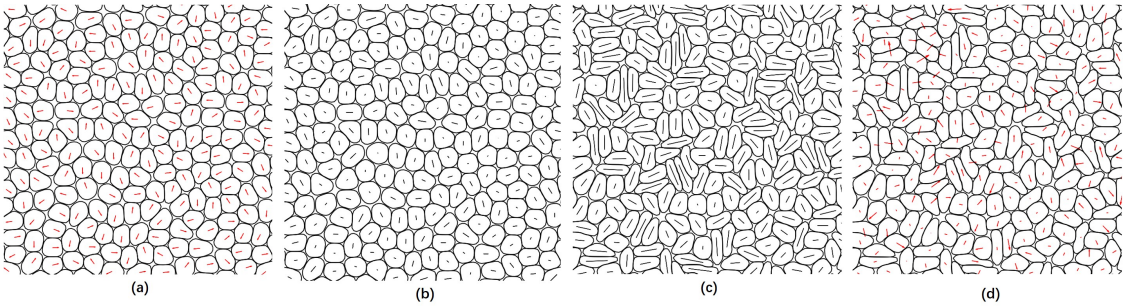


Figure 4.1: Snapshots from the simulations: (a) and (b) are from the simulation for strong polar forcing (case *shape*) with $\alpha = 0.062, \zeta = 0.0, \omega = 0.01$; (c) and (d) are from the simulation for strong dipolar forcing with $\alpha = 0.0, \zeta = 0.044, \omega = 0.01$. In (a) and (d) the red arrows indicate the centre of mass velocity of the cell. In (b) and (c) the solid lines denote the long axis of the cell. All the frames are cropped into a 100×100 domain.

unjamming transitions have been predicted as a function of cell shape using a vertex model [98] and cell motility using a self-propelled Voronoi model [43].

The transition between the two regimes can be investigated quantitatively by plotting the average number of cells that change neighbours at each time step. Fig. 4.3(c) and (d) show how this quantity changes as a function of the strengths of the active dipolar and polar forces, ζ and α, respectively. For a fixed value of the polar force α, Fig. 4.3(c) shows a sharp crossover between jammed and liquid dynamics as a function of ζ. α is small so the dynamics of the polarisation alignment is irrelevant here. On the other hand, for a fixed value of the dipolar activity ζ, as the magnitude of the polar force is increased, there is a much smoother increase in the rearrangement rate (Fig. 4.3(d)). The definition of the polarisation dynamics has only a small quantitative influence on the results: the cells unjam a little more easily if the polarisation aligns to the cell velocity.

The rather sharp increase in the rearrangement rate due to increasing dipolar forces compared to the smoother increase due to increasing polar forces stems from the fundamentally different mechanisms by which these two sources of activity drive the monolayer out of equilibrium. For polar forces, increasing the force results in an increase in the velocity of each individual cell, therefore continuously enhancing cell displacement to overcome the caging effect in the jamming state. On the other hand, dipolar forces need to overcome the energy barrier set by the elasticity of the cells

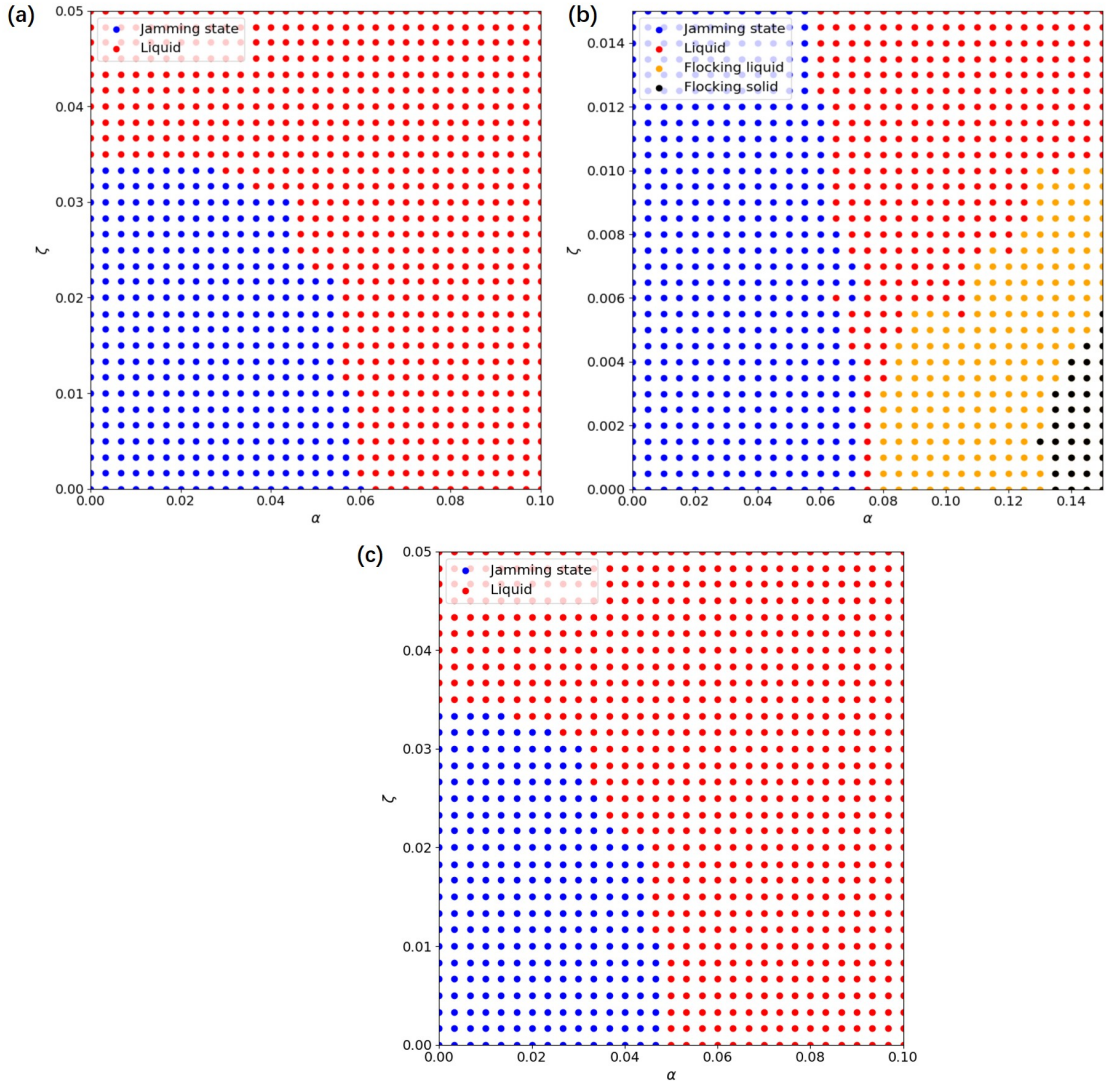


Figure 4.2: Stability diagrams: Modelling the active force densities acting on a cell: Stability diagram for (a) case *shape* (polarisation aligns to long axis of the cell; (b) case *velocity* (polarisation aligns to the velocity of the cell) for $J_{\mathrm{pol}} = 0.1$ and $\omega = 0.005$. (c) case *Brownian* for $D_{\mathrm{pol}} = 0.1$ and $\omega = 0.005$. Jammed states are identified by a rearrangement rate < 0.15. Liquid states have a rearrangement rate > 0.15. Flocking states have a Viscek order parameter $V_a > 0.15$; Note the different scales in (a), (b)and (c).

to be able to deform the cell boundaries. As such, the cell displacement only sets in once the dipolar forces are strong enough to deform the cells in the monolayer.

This is summarised in the stability diagram in Fig. 4.2(a), where we choose a cell rearrangement rate of 0.15 as the boundary between the jammed and liquid phases. These results are for case *shape*, polar force aligned with the long axis of the cell (see Sec. 3.3.1). However, as is clear from the rearrangement rates plotted

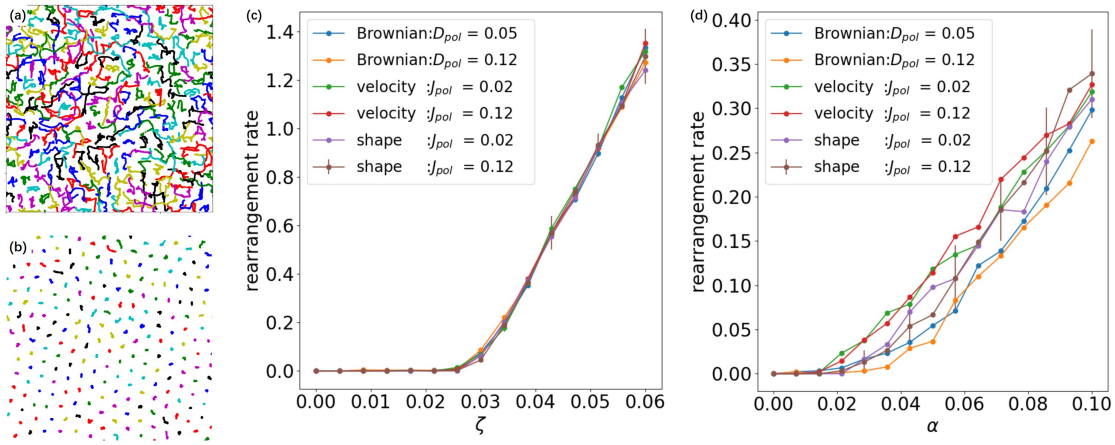


Figure 4.3: Unjamming: Trajectories of cells in (a) the jammed state with $\omega = 0.005, \alpha = 0.02, \zeta = 0.00$ and (b) the liquid state with $\omega = 0.005, \alpha = 0.00, \zeta = 0.04$. Trajectories are followed for 2100 time steps and in both (a) and (b) the polarisation of a cell aligns to the long axis (case *shape* in Sec. 3.3.1). Rearrangement rate as a function of the strength of (c) the dipolar force ζ for α=0.01, (d) the polar force α for ζ=0.06, comparing different definitions of the polarisation alignment. $\omega = 0.01$ in both frames.

in Fig. 4.3, very similar behaviour is seen for all choices of the polarity alignment.

We next investigate the properties of the liquid state in more detail. Fig. 4.4(a) shows a typical snapshot of the velocity field which is characterised by localised bursts of higher velocities. Fig. 4.4(b) shows the vorticity field with vortices on the scale of a few cells. The other panels in the figure display this phenomenon more quantitatively by showing the vorticity-vorticity and velocity-velocity correlation functions for layers driven by dipolar driving (c), (d) or polar forcing (e), (f). Correlations persist over $\sim$ 4 cell diameters and are largely independent of the details or strength of the active forces suggesting that the range of the correlations is set by the passive forces. Polar forces result in larger velocities and there is a tendency of dipolar active forces to elongate the cells. Therefore we now measure the dependence of cell deformations on the active driving.

4.3.2 Cell deformations

In the absence of active forcing the ground state is a honeycomb lattice with the cells taking a hexagonal shape. We investigate how they are stretched by the

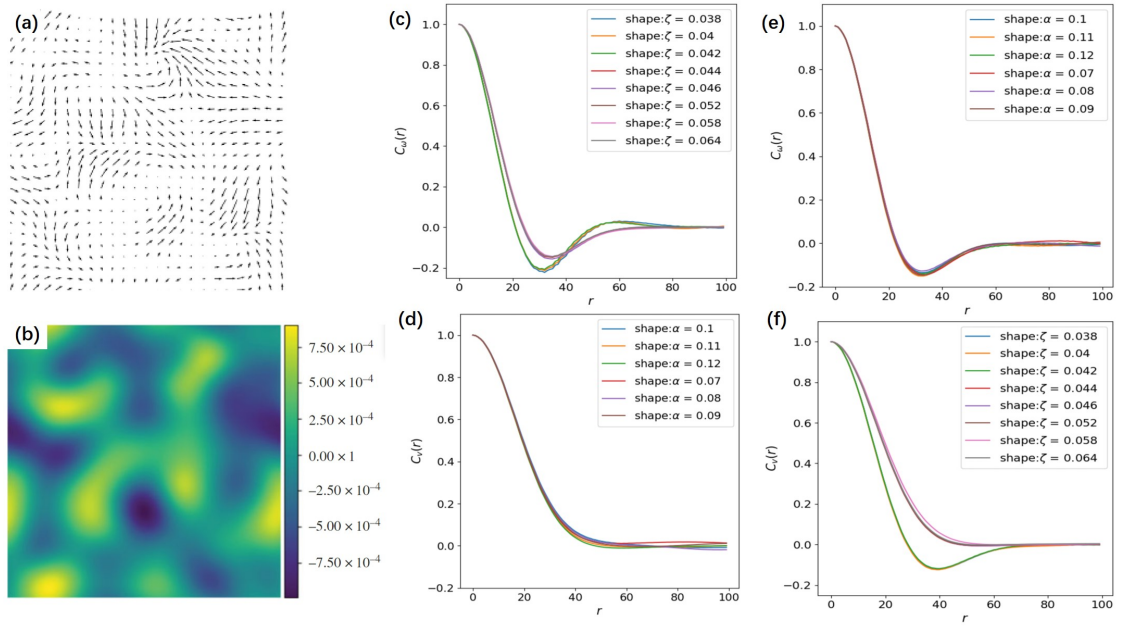


Figure 4.4: Liquid state: Snapshot showing a typical (a) velocity field, (b) vorticity field in the liquid state. The colour bar in (b) indicates the magnitude of the vorticity field. (c) Vorticity-vorticity and (d) velocity-velocity correlation functions for $\alpha = 0$ and different values of the dipolar driving ζ. (e) Vorticity-vorticity and (f) velocity-velocity correlation functions for $\zeta = 0$ and different values of the polar driving α. $\omega = 0.005$.

activity by measuring the average cell deformation,

$$D = \left\langle \sqrt{\mathcal{D}_{xx}^{(i)}(t)^2 + \mathcal{D}_{xy}^{(i)}(t)^2} \right\rangle_{\mathrm{t,i}}, \tag{4.1}$$

where $\mathcal{D}_{xx}^{(i)}$ and $\mathcal{D}_{xy}^{(i)}$ are the xx and xy components of the deformation tensor $\mathcal{D}^{(i)}$ (Eq. 3.18) for cell i and the average is taken over cells and time. Note that $D \leq 0.5$ corresponds to isotropic cells and $D = 3$ to cells with an aspect ratio $\sim$1.75 for the simulation parameter used in this work.

In all the models we consider, changes in cell elongation are most marked in response to changes in the dipolar active forcing ζ. For $\zeta > 0$, these forces contribute to the deformation by elongating individual cells, and also by aligning neighbouring cells. The variation of D with ζ is displayed in Fig. 4.5(a) showing that the dynamics of the polarisation is unimportant in determining how the cells are stretched. Note that for small polar forces the increase of D with ζ is particularly pronounced around $\zeta = 0.025$ which corresponds to the crossover from the jammed to the liquid state.

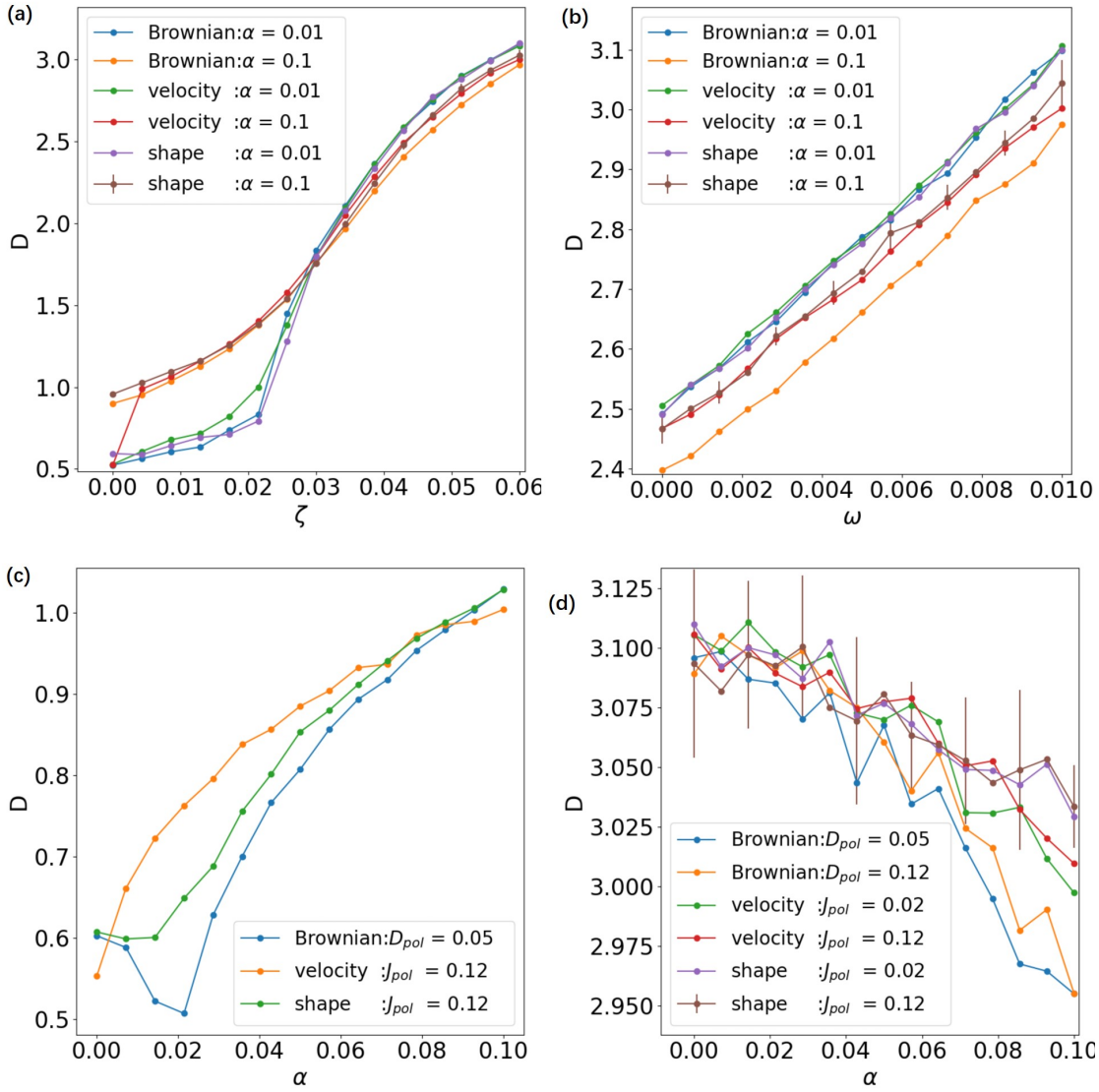


Figure 4.5: Cell shape: Average cell deformation D as a function of (a) the active dipolar force ζ for $\omega = 0.01$; (b) the passive adhesion force ω for $\zeta = 0.06$, and the polar force α for (c) small active, dipolar forces ζ=0.005, (d) large active, dipolar forces $\zeta = 0.06$. $J_{\mathrm{pol}} = 0.12$ and $D_{\mathrm{pol}} = 0.12$ in (a) and (b). $\omega = 0.01$ in (c) and (d).

The passive adhesion force between the cells also steadily increases the cell deformation (Fig. 4.5(b)) but to a lesser extent. This is because this term in the free energy (Eq. 3.6) acts as an effective negative line tension thus mimicking a preference of the cells to increase the length of cell-cell junctions.

Fig. 4.5 also illustrates the changes in cell shape with the strength of the polar force α. For small values of ζ where deformation due to dipolar forces is small (Fig. 4.5(c)), the polar forces can themselves cause significant elongations of the

cells. However, when ζ is large and the cells are already significantly stretched, adding polar forces has the opposite effect of reducing D (Fig. 4.5(d)). This is because the cells tend to move apart more quickly, reducing their tendency to align with, and further extend, their neighbours.

Note that for small α the deformation can be greater than 0.5. This is because the cells remain stuck in the initial jammed state where some cells are deformed. Weak active forces help the cells to move towards a state of hexagonal packing with minimum free energy and low deformation.

4.3.3 Cell speed and flocking

To further characterise the coordinated motion of cells we next measured the averaged cell speed

$$V = \left\langle \sqrt{v_{com,x}^{(i)}(t)^2 + v_{com,y}^{(i)}(t)^2} \right\rangle_{\mathrm{t,i}} \tag{4.2}$$

where $v_{com,x}^{(i)}$ and $v_{com,y}^{(i)}$ are the x and y component of the centre of mass velocity of cell i. Fig. 4.6(a) shows that the cell speed increases linearly with the strength of the polar force α as expected. However, note that the cell speed also increases with the strength of the active dipolar forcing with a sharp change in the rate of increase around $\zeta \sim 0.25$, again corresponding to the transition from a jammed state to a liquid (Fig. 4.6(b)).

We recall the different equations of motion governing the direction of the cell polarisation, introduced in Sec. 3.3.1: *shape*, relaxing to the long axis of the cell; *velocity*, relaxing to the direction of the cell velocity; and *Brownian*, undergoing a persistent random walk. The cell speed, and indeed all other parameters we have considered so far, have had only a small quantitative dependence on the definition used. However, as the strength of the polar force is increased, a new dynamical phase appears, just for the case *velocity*. This is flocking, where large numbers of neighbouring cells move in the same direction.

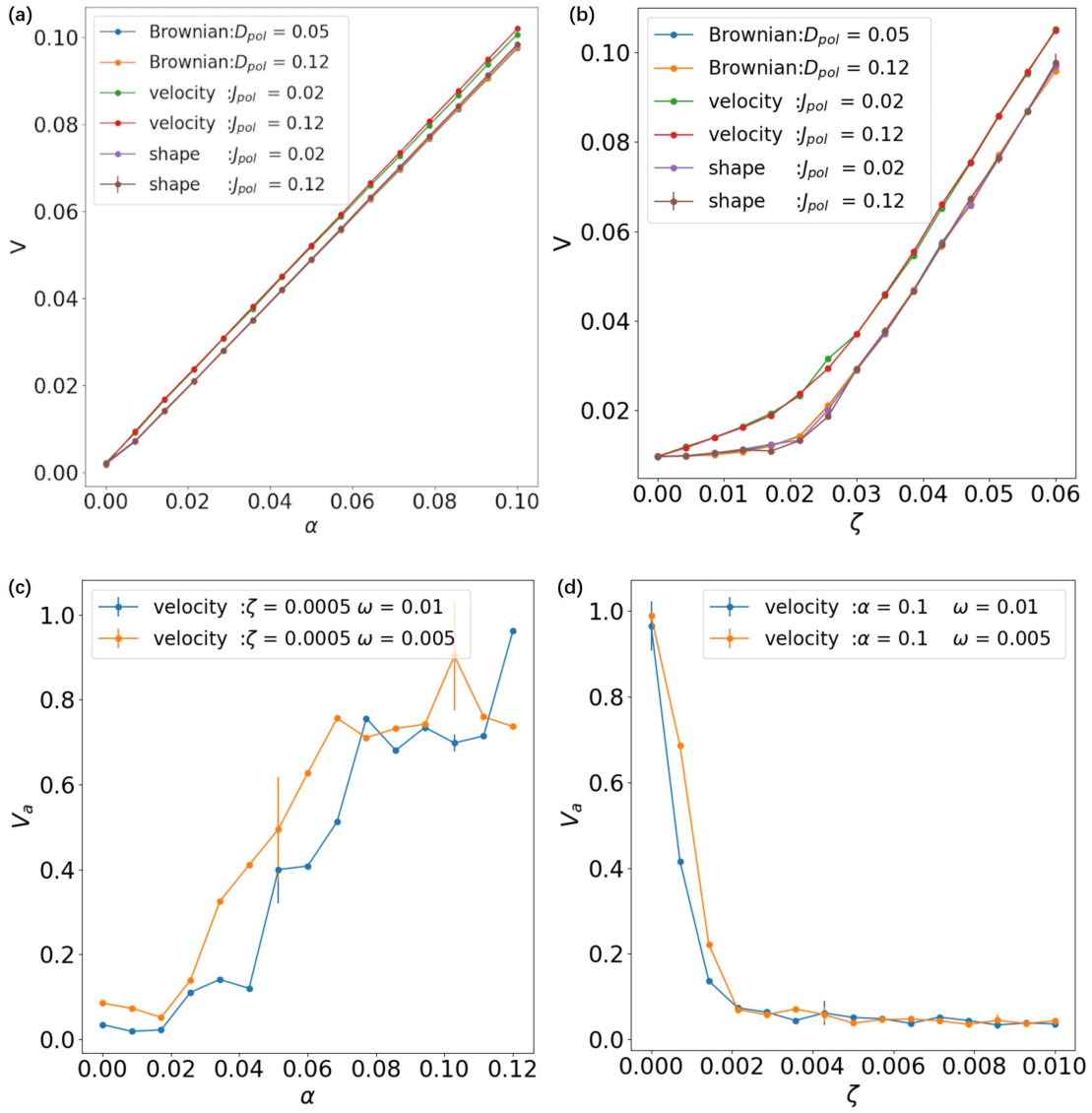


Figure 4.6: Cell movement: Average cell speed V as a function of the strength of (a) the polar force α for $\zeta = 0.005$ and $\omega = 0.01$, (b) the dipolar force ζ for $\alpha = 0.01$ and $\omega = 0.01$. Vicseck order parameter as a function of the strength of (c) the polar force α, (d) the dipolar force ζ. $J_{pol} = 0.12$ in both cases. The large error bars on the data in (c) are a consequence of the strong fluctuations in the flocking state.

To quantitatively characterise the flocking behaviour we define the Vicseck order parameter

$$V_a = \left\langle \frac{1}{N} \left| \sum_i \frac{\mathbf{v}_{\text{com}}^{(i)}}{\left|\mathbf{v}_{\text{com}}^{(i)}\right|} \right| \right\rangle_t \tag{4.3}$$

where $V_a = 1$ corresponds to all the cells moving in the same direction and $V_a = 0$ for random motion. Fig. 4.6(c) shows that flocking occurs as the polar force increases.

However, for a given α, Fig. 4.6(d) indicates that dipolar driving acts to destroy the flocking. This occurs because, as the dipolar active forces increase, the overall repulsive interaction between cells which is needed to stabilise flocks [99, 100] becomes weaker because the effective adhesion arising from the dipolar interactions becomes stronger. As a result, the flocking state disappears, but there are still local clusters inside which the velocities of cells align.

Fig. 4.2(b) shows the phase diagram for the case *velocity* where the polarisation aligns to the direction of the cell velocity. We define flocking states as those with a Viscek order parameter $V_a > 0.15$. The flocking state can be either liquid-like where cells rearrange within the flock or, for larger polar forces, solid-like where they retain their positions.

4.4 Discussion

Using our phase field model in confluent layer of cells, we investigate the relative importance of active polar forces, resulting from lamellopodia pulling on the substrate, with active dipolar forces, resulting from force self-deformation and transmission across cell junctions, in determining the cell dynamics. We compare different possibilities for defining the dynamics of the cell polarisation: *shape*, relaxing to the long axis of the cell; *velocity*, aligning to the direction of the cell velocity; and *Brownian*, undergoing a persistent random walk.

Independent of the way in which the polarity is implemented, a predominant feature of the dynamics is a crossover from a jammed state, where any cell rearrangements are strongly suppressed, to a liquid, where the cells can move relative to each other [43]. The transition can be driven either by polar or by dipolar forces, and in both cases the liquid shows localised bursts of velocity as well as vorticity correlations over several cells, which are phenomena characteristic of the active turbulence observed in active nematics [21]. Correlations are largely independent of the details or strength of the active forces, suggesting that they are mainly controlled by passive forces and are rather insensitive to the exact form of the active driving.

Surprisingly, different mechanisms of polarity alignment not only result in similar patterns of collective motion but even lead to close quantitative measures of cell rearrangement rates, averaged cell deformation, and averaged cell velocity in the monolayer. However, a striking exception is when the polarity aligns to the cell velocity, in which case the cells transition to a flocking state at strong polar forcing. The flocking state is destroyed as the strength of the dipolar forces is increased. This agrees well with the experimental results presented in [33], suggesting that for human mammary epithelial MCF-10A cells the polarity of the cells aligns closely to their velocities.

It is of interest to compare the phase field approach we use here to vertex models; in particular a jamming transition is predicted by both methods [43, 50, 94, 98]. There are some common features shared by the two approaches, for example the cell-cell adhesion is modelled as a negative line tension, quadratic area constraint terms are applied and the form of polar forces is similar to active vertex models. However, in the vertex model, the unjamming transition can be achieved when the relative value of contractility and cell-cell adhesion leads to a vanishing energy barrier of neighbour exchange. In our model, the dipolar forces fluidise the tissue. In both the phase field and the active vertex models, the strength of polar forces affects the details of the unjamming transition.

In vertex models the target shape index is a control parameter. This shape index is defined as

$$q = \left\langle \frac{P^{(i)}}{\sqrt{A^{(i)}}} \right\rangle_{\mathrm{t,i}}$$

where $P^{(i)}$ is the perimeter of cell i which is the contour length at $\varphi^{(i)} = 0.5$ and $A^{(i)}$ is the area enclosed by this contour in our model.

To more directly compare our results to the vertex model we measured the variation in shape index as a function of the strength of the dipolar force ζ and the polar force α (Fig. 4.7). The trend observed for the cell shape index is very similar to the average cell deformation D (Fig. 4.5(a) and Fig. 4.5(c)). For very small polar forces the unjamming transition is at $\zeta \approx 0.03$ (although the value

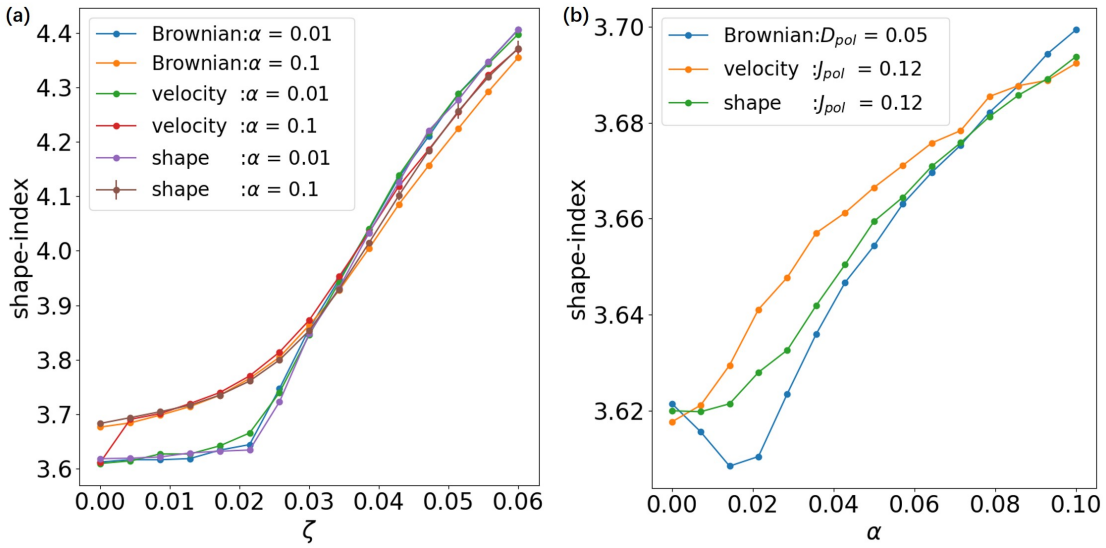


Figure 4.7: Cell shape index as a function of (a) the active dipolar force ζ; (b) the polar force α for small active dipolar forces $\zeta = 0.005$. $\omega = 0.01$ in both frames.

depends on the threshold in rearrangement rate that we choose to correspond to the transition). This corresponds to a shape index $q \approx 3.85$ (Fig. 4.7(a)), which is consistent with the critical shape index of the unjamming transition $q* = 3.81$ under no polar force in the vertex model [43, 98].

The way we choose to implement the forcing in the model, and the parameter values we consider, will undoubtedly need modification in the light of future theoretical and experimental results. For example, we have chosen a polar force that is uniformly distributed over a cell, and it would be interesting to investigate how moving the centre of mass of this force distribution towards the front of a cell changes the dynamics.

The force distribution within cell monolayers has been measured experimentally using traction force microscopy and monolayer stress microscopy [27, 33, 101]. However, it is not yet clear how the forces should be divided into passive or active, or into polar and dipolar contributions. Indeed, it would be of particular interest to vary the polar forces acting on cells by varying the stiffness of substrates [37] or using drug treatments on the kinases such as ROCK which are involved in actin filament protrusion [14]. The strength of dipolar stresses could be modified by controlling the levels of mechanosensors such as α-catenin at the cell-cell junctions [12].

Comparing the force density in different situations, both experimentally and in models such as the one presented here, will provide a framework which will help to interpret current and future measurements, leading to an improved understanding of tissue mechanics in confluent cell layers and epithelia.

In this Chapter, we have concentrated on extensile dipolar forcing that acts to increase the extension of a cell. In the next chapter, we will consider the contractile case. As we described in Chapter 1, topological defects characterise the nematic feature of tissue monolayers. However, we did not observe this behaviour clearly in the result we presented in this chapter. In Chapter 5, we will investigate how inter-cellular interactions can give rise to active turbulence and topological defects.

5

Active forces in confluent cell monolayers

Contents

5.1 Introduction 57
5.2 Simulation method 59
5.3 Inter-cellular contractile forces without fluctuations . 59
5.4 Inter-cellular extensile forces without fluctuations . . . 60
5.5 Fluctuations 62
5.6 Discussion 63

5.1 Introduction

Motile topological defects have been identified in confluent layers of cells, showing the nematic features of the cell monolayers [8, 12, 13, 102]. This is reminiscent of active turbulence, which is the dynamical behaviour of many active nematic materials. However, the appearance of active turbulence requires elongated particles [21] and therefore it is somewhat surprising to identify topological defects even in assemblies of e.g. MDCK cells that are on average isotropic in shape [12]. Moreover the comet defects can move towards their head, corresponding to extensile driving [66], even though individual cells are contractile [13]. Indeed, experiments and simulations have shown that the defect motion changes direction - indicating a change from extensile to contractile behaviour - as the cell-cell adhesion is varied.

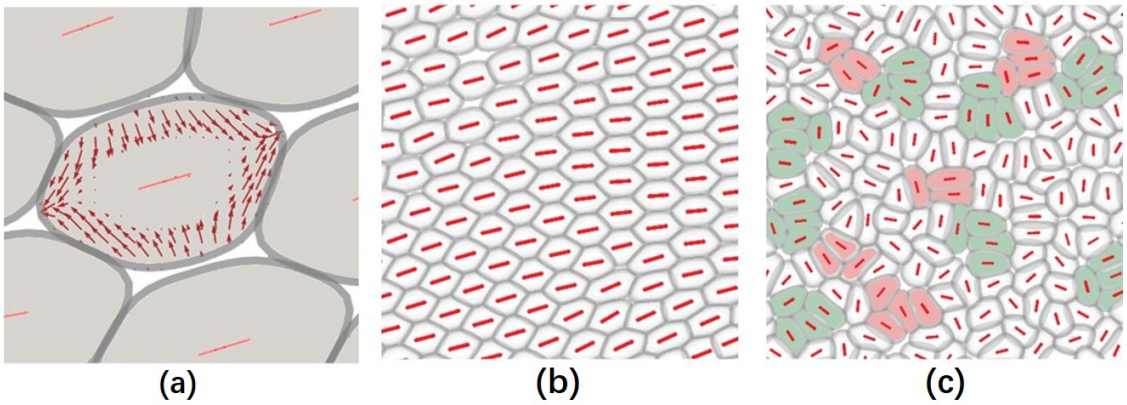


Figure 5.1: (a) inter-cellular contractile forces act on the central cell as a self-extensile force (b) nematic ordering in tissue with contractile inter-cellular forces ($\omega = 0.5, \zeta_{\text{inter}} = -0.6$ for (a) and (b)) (c) 'capped line' structures (distinguished as red and green regions) in tissue with extensile inter-cellular forces. Red bars indicate cell elongation axes.

Other theoretical work has shown that fluctuating polar (unbalanced) forces can result in extensile defects [103–105].

These observations raise questions about the identity of the physical forces governing collective cell motility. The formation of lamellopodia is suppressed in confluent cell layers, as contact inhibition of locomotion suggests the absence of any persistent, unbalanced (polar) forces [106, 107] (also see Section 3.3.2 for explanations in more detail). Therefore balanced, dipolar forces must be acting to drive the cellular dynamics. The most likely physical origin for these features is the contractility generated from the cytoskeleton which acts through inter-cellular junctions to pull on the cell's neighbours (see Chapter 3, Section 3.3.2).

In this Chapter, we present analytical arguments and simulations based on a two-dimensional, coarse-grained, phase field model of cell motility, to show that active, contractile interactions between cells, mediated through cell junctions, lead to the cells elongating and lining up to give nematic ordering. Decreasing cell-cell adhesion leads to flows which destabilise the nematic order, resulting in active turbulence and contractile topological defects.

We further show that anisotropic fluctuations of the inter-cellular forces can change the direction in which the defects move.

5.2 Simulation method

We calculate the dynamics of $\varphi^{(i)}$ using Eq. 3.1 and Eq. 3.2. The passive force (Eq. 3.10) and free energy (Eq. 3.3-3.6) in Section 3.2 excluding the $\mathcal{F}_{shape}$ term (Eq. 3.7) are applied. The active inter-cellular force is modelled by Eq. 3.27 and Eq. 3.29. We choose $\zeta_{\text{self}} = 0$ to study the effect of the inter-cellular forces alone, but our arguments are not changed qualitatively by a self-contractility that is small compared to the inter-cellular term (see Fig. C.1). In Section 5.3 and 5.4, we assume instantaneous alignment of the director to the elongation axis of the cell $\mathbf{n}^{(i)} = \mathbf{d}_{\parallel}^{(i)}$ (see Eq. 3.18 for the definition of the deformation tensor, $\mathcal{D}^{(i)}$, $\mathbf{d}_{\parallel}^{(i)}$ and $\mathbf{d}_{\perp}^{(i)}$). To investigate the anisotropic fluctuation in the active inter-cellular force, we model the dynamics of $\mathbf{n}^{(i)}$ using Eq. 3.22 and Eq. 3.23 (see Appendix A for the numerical implementation).

We simulate the dynamics of 360 cells of radius $R = 8$ in a periodic domain of size 280×280 lattice sites. Initially, cells with radius $R/2$ are placed randomly, but with the constraint that the distances of neighbouring centres $> 0.8R$. They are then relaxed for 3000 time steps under passive dynamics to reach confluence. The simulations then start with a randomly oriented nematic director. They are run for 30000 time steps and data is collected after 3000 time steps. Parameter values are $\lambda = 2.0$, $\gamma = 1.4$, $\kappa = 1.5$, $\mu = 120$, $\xi = 3.0$ and $J_0 = 0.005$. We use $J_n = 0.1$ for a fast relaxation scheme when solving Eq. 3.22 for fluctuating inter-cellular forces. Details of defect detection are given in Appendix B.

5.3 Inter-cellular contractile forces without fluctuations

Individual cells are contractile, so a plausible physical picture is that a cell feels the contractile forces from its neighbours, transmitted through cell-cell junctions. Therefore, we first investigate contractile, inter-cellular forces ($\zeta_{\text{inter}} < 0$), assuming instantaneous relaxation of the director to the elongation axis of the cell ($\mathbf{n}^{(i)} = \mathbf{d}_{\parallel}^{(i)}$).

Fig. 5.1(a) shows the typical force density acting on a given cell due to its contractile neighbours. Surprisingly, the cell is *stretched*.

This can be explained by considering Eq. 3.29. The gradient of a phase field, $\nabla\varphi^{(i)}$, points perpendicular to a cell boundary towards the cell centre. In addition, in a confluent monolayer with strong cell-cell adhesion, cells nestle closely sharing common interfaces. These properties allow us to approximate $\nabla\varphi^{(j)} \approx -\nabla\varphi^{(i)}$ at cell-cell overlap (measured by $\varphi^{(i)}\varphi^{(j)}$) for the dominant contributions in Eq. 3.29 (with $\zeta_{self} = 0$), so the active inter-cellular force can be written

$$\mathbf{f}^{(i)}_{\text{active}}(\mathbf{x}) \approx +\zeta_{\text{inter}}\, \mathbf{Q}^{(i)}_{\text{eff}} \cdot \nabla\varphi^{(i)}(\mathbf{x}) \tag{5.1}$$

in terms of an effective $\mathbf{Q}$-tensor field, $\mathbf{Q}^{(i)}_{\text{eff}} = \varphi^{(i)} \sum_{j\neq i} \mathbf{Q}^{(j)}\varphi^{(j)}$.

The change in sign shows that a cell with contractile neighbours will be subject to an extensile-like, self-deformation force density (Fig. 3.3) which stretches the cell (Fig. 5.1(a)). Moreover, Eq. 5.1 shows that each cell tends to align along the average elongation direction of its neighbours which, following the usual mean-field argument, is expected to result in nematic ordering. We check and extend this argument by solving the phase field model numerically for 360 cells. For strong cell-cell adhesion, $\omega = 0.5$, the cells are extended and aligned and become jammed in the configuration shown in Fig 5.1(b). Decreasing the cell-cell adhesion to zero weakens the alignment and allows the cells to move collectively. We observe the well-known splay instability that characterises contractile active nematics, and which leads to active turbulence. Topological defects are continually created and destroyed. These move towards their tail confirming that they result from contractile forces (Fig. 5.2(a)-(d)).

5.4 Inter-cellular extensile forces without fluctuations

Although a contractile, inter-cellular force is more physical, it is interesting to compare extensile forcing ($\zeta_{\text{inter}} > 0$). In this case, the perpendicular orientation of neighbouring cells is favoured, and the alignment due to effective self-interactions is frustrated (the configuration where each pair of neighbours are perpendicular to each

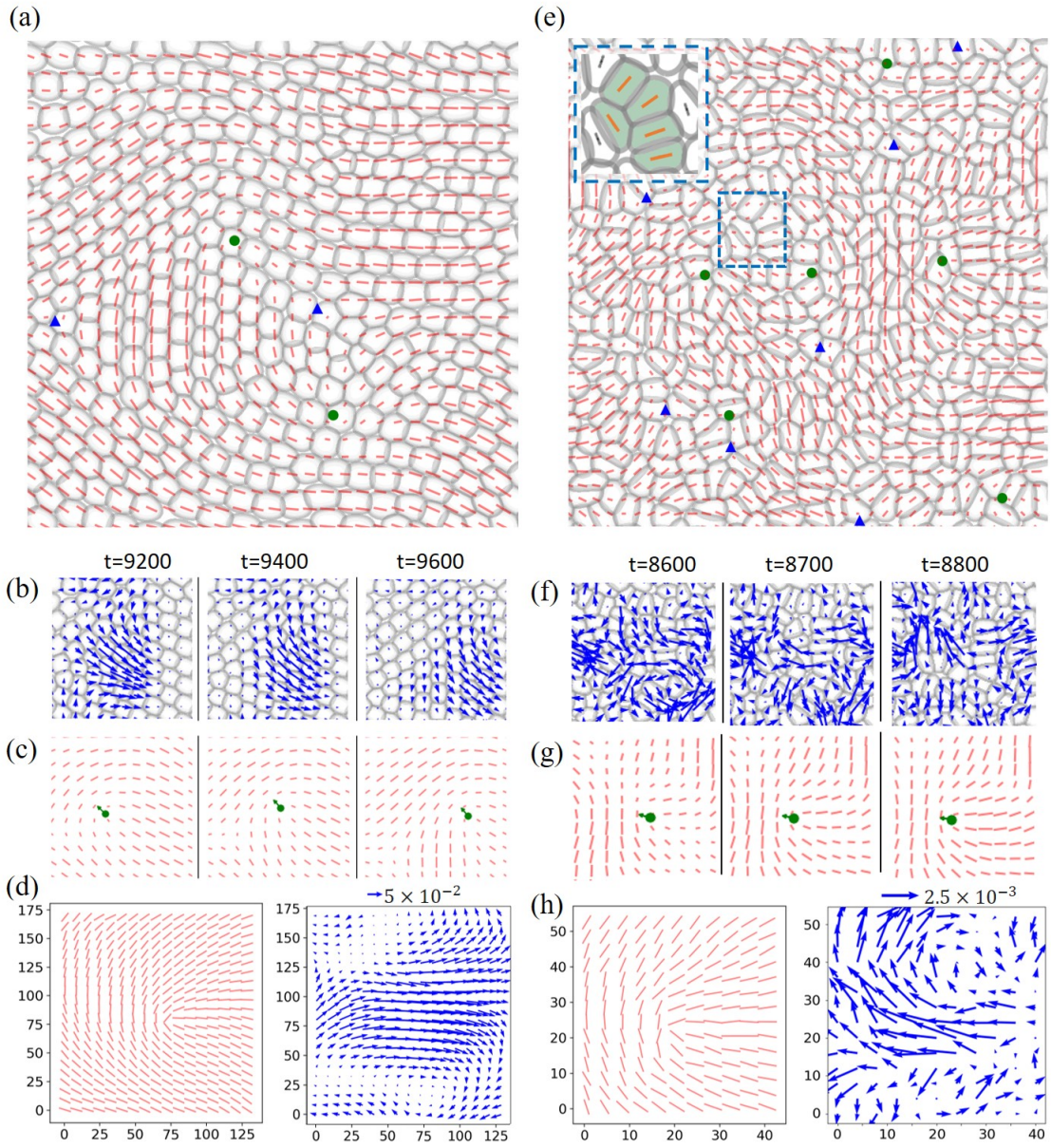


Figure 5.2: Cell and defect dynamics driven by inter-cellular forces. Left column: contractile inter-cellular forces, $\zeta_{\text{inter}} = -0.6$, $\omega = 0$. Right column: extensile inter-cellular forces, $\zeta_{\text{inter}} = +0.4$, $\omega = 0$. (a),(e) Simulation snapshots. Red lines indicates the coarse-grained field of elongation axes. Green dots and blue triangles indicate +1/2, comet-like, and -1/2, trefoil-like, defects. The sub-frame of (e) shows the 'capped line' cell configuration. (b),(f) Cell configuration around a +1/2 defect with imposed velocity field (blue arrows) at successive times. (c),(g) Corresponding images showing the elongation axes field, and the defect motion. The defect moves towards its tail (head) in the contractile (extensile) system. (d),(h) Averaged cell elongation axes (left) and velocity (right) fields in the vicinity of a defect(86 and 325 +1/2 defects are averaged for (d) and (h), respectively). Note the scale change between the contractile and extensile cases. Similar results for -1/2 defects are given in Fig. C.2.

other cannot be achieved globally). Thus, there is no long-range ordering. Instead, cells tend to arrange themselves locally, at the scale of a few cells, in a *capped line* structure (Fig. 5.1(c), Fig. 5.2(e)). Measuring the average velocity field around defects confirms that they move tail to head as expected in an extensile system (Fig. 5.2(e)-(h)). Defects form more easily, and are more localised and less persistent than in the contractile case (note the different scales of Fig. 5.2(d) and (h)).

It is of interest that similar capped line structures are seen in simulations of hard rods, driven by a polar force [108, 109].

5.5 Fluctuations

We next model the strong fluctuations in cell shape that are observed in many epithelial cell layers by including the anisotropic noise term, defined in Eq. 3.23, in the equation governing the relaxation of a cell director, Eq. 3.22. This leads to anisotropic fluctuations of the inter-cellular forces. If the relaxation of the director to the long axis of a cell is rapid compared to the time scale of cell reorientation, Eq. 3.22 can be integrated to give

$$\mathbf{n}^{(i)} = \mathbf{n}_0^{(i)} e^{-J_n t} + \mathbf{d}_\parallel^{(i)}(1 - e^{-J_n t}) + \int_0^t ds\ \boldsymbol{\eta}(s) e^{-J_n(t-s)} \tag{5.2}$$

where $\mathbf{n}_0^{(i)}$ is the director of cell i at $t = 0$. Note that $\langle \mathbf{n}^{(i)} \rangle \approx \mathbf{d}_\parallel^{(i)}$ for times longer than the relaxation time scale. Thus, $\mathbf{n}^{(i)}$ is not of unit length (this is only true for its mean value) but fluctuates around $\mathbf{d}_\parallel^{(i)}$, the unit vector along the elongation axis. Using this expression in Eqs. (3.24) and (3.29) the averaged inter-cellular force follows as

$$\langle \mathbf{f}_{\text{active}}^{(i)}(\mathbf{x}) \rangle \approx -\zeta_{\text{inter}}(1 + \frac{D_\parallel - D_\perp}{2J_n}) \sum_{j \neq i} (\mathbf{d}_\parallel^{(j)} \mathbf{d}_\parallel^{(j)^T} - \frac{1}{2}\mathbb{I}) \cdot \nabla \varphi^{(j)}(\mathbf{x}).$$

Hence fluctuations in cell shape along $\mathbf{d}_\perp$ tend to change the sign of the activity.

This is confirmed in Fig. 5.3 where we plot the defect velocity against $D_\perp - D_\parallel$, showing a change from contractile to extensile behaviour (see also Fig. C.3). Further evidence for a crossover is presented in Fig. 5.4 where the distribution of the angles between the long axes of neighbouring cells is plotted. With increasing $D_\perp$ there

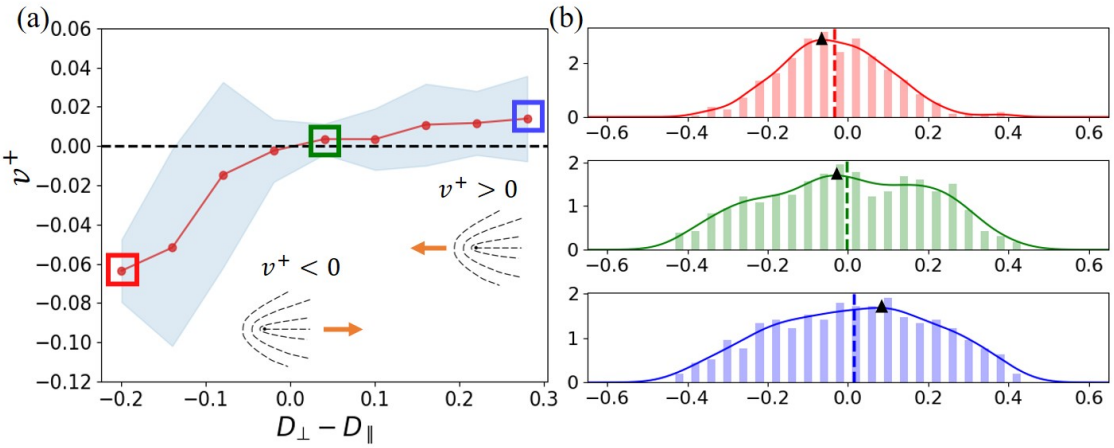


Figure 5.3: (a) Velocity of the +1/2 defects along their tail to head direction, v^+, as the magnitude of the fluctuations along the short axis of the cells, $D_\perp$, is varied. The red line is the average velocity and the light blue background denotes the standard error. (b) Histogram of v^+ for 201(red), 401(green), 305(blue) defects corresponding to framed points in (a). Vertical dashed lines: mean value. Black triangles: maximum of the smoothed histogram. $\zeta_{\text{inter}} = -0.6, D_\parallel = 0.2, \omega = 0.0$
.

is a crossover from a peak at 0^o signalling nematic ordering to two weaker peaks at 0^o and 90^o indicating the capped line state. Note that anisotropic fluctuations can also allow the reverse process, a change from extensile behaviour to contractile behaviour. When extensile and contractile influences balance (green square in Fig. 5.3), a jammed phase emerges where the shape of cells is round on average, but fluctuates strongly.

5.6 Discussion

Our work gives an explanation for why cells that are, on average, circular can exhibit nematic ordering and active turbulence in terms of fundamental, active, interactions between the cells. It also shows that the direction of motion of active defects can vary. We argue that intercellular forces mediated through cell-cell junctions can lead to contractile behaviour. Anisotropic fluctuations in these forces (perpendicular to the long axis of the cell) can then drive the system extensile.

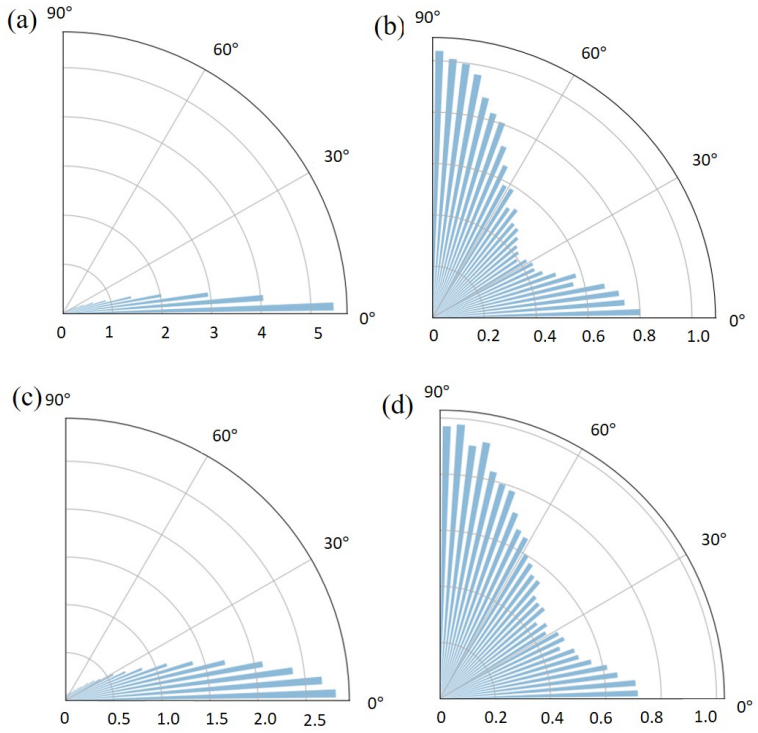


Figure 5.4: Distributions of the elongation axes of neighbouring cells. (a) contractile forces, $\zeta_{\text{inter}} = -0.6$. (b) extensile forces, $\zeta_{\text{inter}} = +0.4$. (c) contractile forces with fluctuations, $\zeta_{\text{inter}} = -0.4, D_{\parallel} = 0.2, D_{\perp} = 0.0$. (d) contractile forces with anisotropic fluctuations that lead to effective extensile behaviour, $\zeta_{\text{inter}} = -0.4, D_{\parallel} = 0.0, D_{\perp} = 0.6$. In (a) and (c), most of the cells line up with their neighbours except for cells around defects. In (b) and (d), a "capped line" structure is favoured. Therefore, the distribution peaks at 90^o and 0^o.

By contrast, work in [103–105] has shown that fluctuating *polar* forces can result in extensile, but not contractile, stress.

Our prediction that the activity of confluent cell layers depends on anisotropic fluctuations of inter-cellular forces and hence on cell shape could be tested experimentally by analysing the dynamical evolution of monolayers. Moreover, the method we have applied in this chapter can be extended to study other nematic features. In the next chapter, we will investigate the nematic instability of cells confined in a channel.

6

The interplay between tissue viscoelasticity and active inter-cellular forces

Contents

6.1 Introduction 65
6.2 Boundary conditions and simulation method 67
6.2.1 Boundary conditions 67
6.2.2 Simulation method 67
6.3 Results 68
6.3.1 Transitions between jammed, oscillatory shear and shear flow states 68
6.3.2 Jammed, nematic state 70
6.3.3 Active instability induced oscillation and wave-like behaviour 70
6.3.4 Spontaneous shear flow 73
6.3.5 The effects of the cell aspect ratio 74
6.4 Discussion 75

6.1 Introduction

We have investigated how nematic features, such as topological defects, emerge from inter-cellular interactions in Chapter 5. Other nematic features such as nematic instability-induced shear flow also have been observed for cells confined in a channel [35]. A viscous continuum model has been used to study the shear

flow. However, how to model this effect using a cellular level model is not clear. Moreover, epithelial cells show not only viscous behaviours, but also elastic features, which viscous models may not easily capture. Rheology experiments on tissue monolayers show biphasic stress relaxation. They find that monolayer mechanics contain an elastic and a viscous component by fitting the stress relaxation data to the viscoelastic rheology model [110]. Interestingly, cross-linked cell monolayers share similar rheology properties to a single cell, indicating that cell-cell junctions link the cell and transmit forces. Stokes experiments on MDCK cells demonstrate that cell flows like Maxwell material [111]. In both these experiments, a perturbation of myosin motors, the motor protein accounting for cell contractility, significantly changes the material relaxation time. These observations demonstrate that the individual cell properties and inter-cellular interactions contribute to tissue-level viscoelasticity. Moreover, transitions from solid behaviour to liquid behaviour can be observed not only in the strain-relaxation process but also can be triggered by active fluctuations of cell-cell tensions, active Brownian dynamics of cell polarisation and long-range interactions among cells [112].

Although these experiments have demonstrated the viscoelastic properties of cells, little is known about how these tissue-level properties emerge from cell-level mechanics. Also, how the inter-cellular forces affect the viscoelasticity of the cell monolayer is not clear. To address these questions, we use the computational phase field model to study the collective behaviour of cells confined in a channel with a strong parallel anchoring as a model system. We observe different collective behaviours, indicating the jammed state, contractile inter-cellular force inducing spontaneous bidirectional shear flow and an oscillatory state in both the cell velocity and the nematic director, showing that the viscous and elastic properties of cells can be controlled by their properties, such as repulsive, and adhesive interactions and the aspect ratio. We also show that increasing the length of the system leads to a transition between oscillation and a mechanical wave.

6.2 Boundary conditions and simulation method

6.2.1 Boundary conditions

To model the confinement, we define walls by using a passive, fixed, phase field $\varphi_{wall}(x, y) = e^{-(y-L_y)/d} + e^{-y/d}$ located at the top and the bottom of the channel, where d is the thickness of the wall and $L_x \times L_y$ is the size of the system. The free energy between walls and cells is

$$\mathcal{F}_{walls} = \sum_i \frac{\kappa_{wall}}{\lambda} \int d\mathbf{x}\ \varphi^{(i)}(\mathbf{x})^2 \varphi_{wall}(\mathbf{x})^2 + \sum_i \omega_{wall}\ \lambda \int d\mathbf{x}\ \nabla\varphi^{(i)} \cdot \nabla\varphi_{walls}. \quad (6.1)$$

Periodic boundary conditions are implemented at the left ($x = 0$) and right ($x = L_x$) edges of the simulation domain as shown in Fig. 6.1.

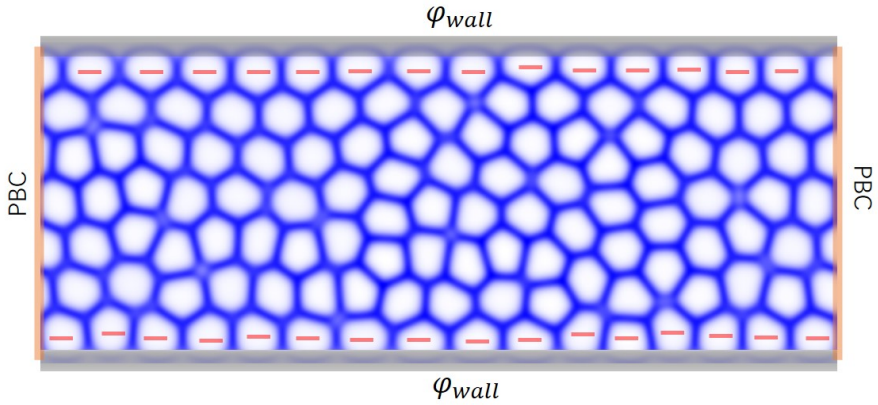


Figure 6.1: Schematic for cells confined in a channel: Cells are confined in a channel by φ_{wall} (the regions in grey). We apply the periodic boundary conditions at the left and right edges of the channel (the region in orange). Parallel anchoring (the red bars) is imposed for cells at the top and bottom of the channel.

Experiments with a similar geometry show a parallel anchoring at the long edges of the channel [35, 113]. To account for this, we impose a strong parallel anchoring for cells located at the top or the bottom of the channel by forcing $\theta_n^{(j)} = 0$ if $y_{\text{com}}^{(j)} < 2R$ or $y_{\text{com}}^{(j)} > L_y - 2R$, where $y_{\text{com}}^{(j)}$ is the y-coordinate for the centre of mass of cell j (see Fig. 6.1).

6.2.2 Simulation method

We calculate the dynamics of $\varphi^{(i)}$ using Eq. 3.1 and Eq. 3.2. The passive force (Eq. 3.10) and free energy (Eq. 3.3-3.7) from Section 3.2 are applied. We remark

that the aspect ratio is incorporated by employing the $\mathcal{F}_{shape}$ term (Eq. 3.7) in the free energy. The active inter-cellular force is modelled by Eq. 3.27 and Eq. 3.29. Eq. 3.21 is applied to model the angular dynamics where the nematic director of a cell aligns with its elongation axis.

We simulate the dynamics of 112 cells of $R = 8$ in a domain of size $L_x \times L_y = 256 \times 112$ lattice sites. We remark that for round cells, $AR_0 = 1$, and cells are forces by the $\mathcal{F}_{shape}$ term to elongate to an elliptical shape whose semi-major and semi-minor axis equal $R\sqrt{AR_0}$ and $R/\sqrt{AR_0}$ respectively. Initially, elliptical cells with semi-major and semi-minor axis $0.5R\sqrt{AR_0}$ and $0.5R/\sqrt{AR_0}$ are placed randomly, and orientation angles $\theta_n^{(i)}$ are randomly drawn from $(-\pi, \pi)$, but with the constraint that there is no overlap between the bounded boxed of these ellipses. They are then relaxed for 3000 time steps under passive dynamics to reach confluence. The simulations are run for 80000 and 180000 time steps for circular ($AR_0 = 1$) and elongated cells ($AR_0 > 1$). Data is collected after 40000 time steps for circular cells and after 140000 time steps for elongated cells. Parameter values are $\zeta_{\text{inter}} = -1.2$, $\lambda = 3.5$, $\gamma = 2.0$, $K_g = 0.8$, $\kappa = 1.5$, $\mu = 120$, $\xi = 3.0$, $J_0 = 0.005$, $J_{\text{nem}} = 0.1$, $D_{\text{nem}} = 0.01$, $d = 3.0$, $\kappa_{wall} = 3.0$ and $\omega_{wall} = 0.6$ unless otherwise specified. We remark that we only study the inter-cellular forces, and the self-deformation force is disabled by setting $\zeta_{\text{self}} = 0$.

6.3 Results

6.3.1 Transitions between jammed, oscillatory shear and shear flow states

In this section, we focus on naturally isotropic cells ($AR_0 = 1$) with fixed contractile activity ($\zeta_{\text{inter}} = -1.2$). We first probe the motion of cells by examining their velocities. To quantify the oscillatory state and the shear flow, we measure two parameters ΔV_x and ΔV_x^{abs} which are defined as

$$\Delta V_x = \frac{1}{\Delta t} \left| \int_{t_0}^{t_0+\Delta t} dt \int_0^{L_y/2} dxdy \; v_x(x, y + L_y/2) - v_x(x, y) \right| \tag{6.2}$$

$$\Delta V_x^{abs} = \frac{1}{\Delta t} \int_{t_0}^{t_0+\Delta t} dt \int_0^{L_y/2} dxdy \; \left| v_x(x, y + L_y/2) - v_x(x, y) \right|, \tag{6.3}$$

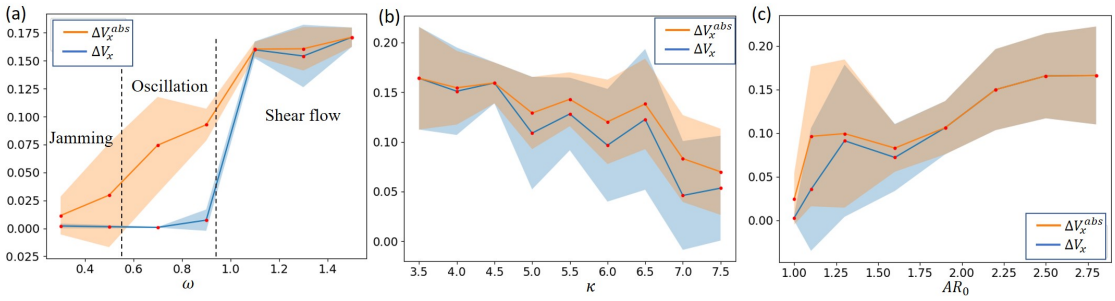


Figure 6.2: ΔV_x and ΔV_x^{abs} are measures of different states ΔV_x and ΔV_x^{abs} as a function of (a) cell-cell adhesion control parameter ω, (b) repulsion coefficients κ and (c) the natural aspect ratio AR_0. For (a), $\kappa = 4.0$ and $AR_0 = 1.0$. For (b), $\omega = 1.2$ and $AR_0 = 1.0$. For (c), $\kappa = 2.0$ and $\omega = 0.6$.

where $v_x(x, y)$ is the x-component of the velocity field. ΔV_x and ΔV_x^{abs} measure the accumulation of signed and absolute shear velocity in time respectively. In the nematic, jammed states, cells elongate in parallel with their neighbours with low cell velocity, and both ΔV_x and ΔV_x^{abs} are nearly zero as the cells are nearly static. For oscillatory shear states, the cells in the upper half of the channel move in the opposite direction to those in the lower half of the channel, they then move back and forth in time, generating oscillatory shear. The oscillatory shear pattern oscillates in time and cancels in the calculation of ΔV_x but accumulates in ΔV_x^{abs}. Thus, in this state $\Delta V_x^{abs} > \Delta V_x > 0$. For steady shear flow states, cells in the upper half of the channel move oppositely to those in the lower half of the channel and do not change direction, both ΔV_x^{abs} and ΔV_x increase, and thus we have $\Delta V_x^{abs} \approx \Delta V_x > 0$.

The nematic instability in a wet, viscous medium can give rise to the shear flow [114]. On the other hand, the elasticity resists strain and restores the material from deformation. The interplay between these two effects can give rise to different states. We first explore the transition between these states by changing the cell-cell adhesion. Fig. 6.2(a) shows a transition from a jammed state to oscillatory shear as the cell-cell adhesion control parameter ω increases from 0.3 to 0.75. As ω further increases, a sharp transition from shear oscillation to steady shear flow is observed. These transitions not only result from the active inter-cellular forces but also indicate a change from elastic to viscous behaviour. From this point of view, Fig. 6.2(a) shows that cell-cell adhesion causes a crossover from elastic to the viscous behaviour.

As the repulsive forces play an opposite role to the adhesive forces, we would expect that the elasticity will be enhanced at a high repulsion. To test this, we increase the control parameter of the repulsive force, κ, and find that both ΔV_x and ΔV_x^{abs} decrease (Fig. 6.2(b)), revealing that the system becomes jammed as we expected. A large κ gives rise to a hard-sphere-like behaviour for cells, thus leading to a high elastic modulus of the tissue. We describe these states in more detail in the following sections.

6.3.2 Jammed, nematic state

Inter-cellular contractility can elongate a cell and gives rise to the nematic state where most of the cells elongate in the same direction [57]. The cell elongation is along the channel as the confluent tissue layer is confined with parallel anchoring. At the same time, the nematic instability is restrained by the elasticity of the cell at a low cell-cell adhesion, and the speed of the cell motion is slow, indicating a jammed state. However, as the cell-cell adhesion increases, the inter-cellular contractile forces make the tissue behaves less elastically, and the jammed state changes to a collective cell oscillation. This seems counter-intuitive, but we note that the cell-cell adhesion is a negative line-tension-like term in our model, which prefers cell-cell contact but does not prevent the bidirectional shear.

6.3.3 Active instability induced oscillation and wave-like behaviour

In the oscillating state, the nematic directors of cells in the middle of the channel tilt at a small angle. However, the nematic directors for cells at the top and the bottom of the channel are parallel to the channel walls as imposed by the boundary condition. Therefore, splay patterns are formed near the walls (Fig. 6.3(e)), leading to a shear flow where cells at the top of the channel move in one direction and cells at the bottom move oppositely due to the inter-cellular activity. However, this shear flow pattern is not sustained; the cells move back to their equilibrium position after they reach a maximum displacement and a maximum tilt angle.

They then move in the opposite direction and set up an oscillation. A full cycle completes when the cells move back to their initial position again. Fig. 6.3(e), (f) and (g) show the snapshots of the cell oscillation.

To quantify the oscillations, we plot the average velocity for the strip of cells near the top of the channel ($L_y - 5R < y^{(i)}_{com} < L_y - 2R$) and the bottom of the channel ($2R < y^{(j)}_{com} < 5R$),

$$V_x^{top}(t) = \frac{1}{N_{top}} \sum_i v^{(i)}_{com,x}, \tag{6.4}$$

$$V_x^{bot}(t) = \frac{1}{N_{bottom}} \sum_j v^{(j)}_{com,x}, \tag{6.5}$$

and the averaged angle of the nematic directors excluding cells located at the long edges ($2R < y^{(k)}_{com} < L_y - 2R$)

$$\Theta_n(t) = \frac{1}{N_{mid}} \sum_k \theta_n^{(k)} \tag{6.6}$$

where N_{top}, N_{bottom} and N_{mid} are the number of cells whose center of mass is located within the top strip, the bottom strip and the middle region respectively, and $v^{(i)}_{com,x}$ is the x-component of the centre of mass velocity for cell i. Fig. 6.3(a) shows bV_x^{top} and V_x^{bot} as a function of time, and Fig. 6.3(b) shows the oscillation of the tilt angle of the nematic directors. The oscillatory states of Θ_n, V_x^{top} and V_x^{bot} have the same frequency as the inter-cellular, nematic force that induces the shear. To explore the time scale of the oscillation, we plot the oscillation period, T, as a function of the cell-cell adhesion (Fig. C.4 in Appendix C.3) and find that T increases with the cell-cell adhesion.

This oscillation can also be reflected by the variation of the free energies in time. To investigate the role of energy variation in the oscillation, we rescale the repulsive energy, adhesive energy and the magnitude of the velocity, denoted as $\tilde{E}_{rep}$, $\tilde{E}_{adh}$ and $|\tilde{V}_x^{top}|$ respectively, to be in the range between zero and one and plot them together. Note that although V_x^{top} and V_x^{bot} are out of phase, their absolute values are in phase, so we only plot $|\tilde{V}_x^{top}|$. Fig. 6.3 (c) and (d) show that the variations of the repulsive energy and the adhesive energy are out of phase and in phase with the oscillation of $|\tilde{V}_x^{top}|$ respectively. When the adhesive energy is at its minimum,

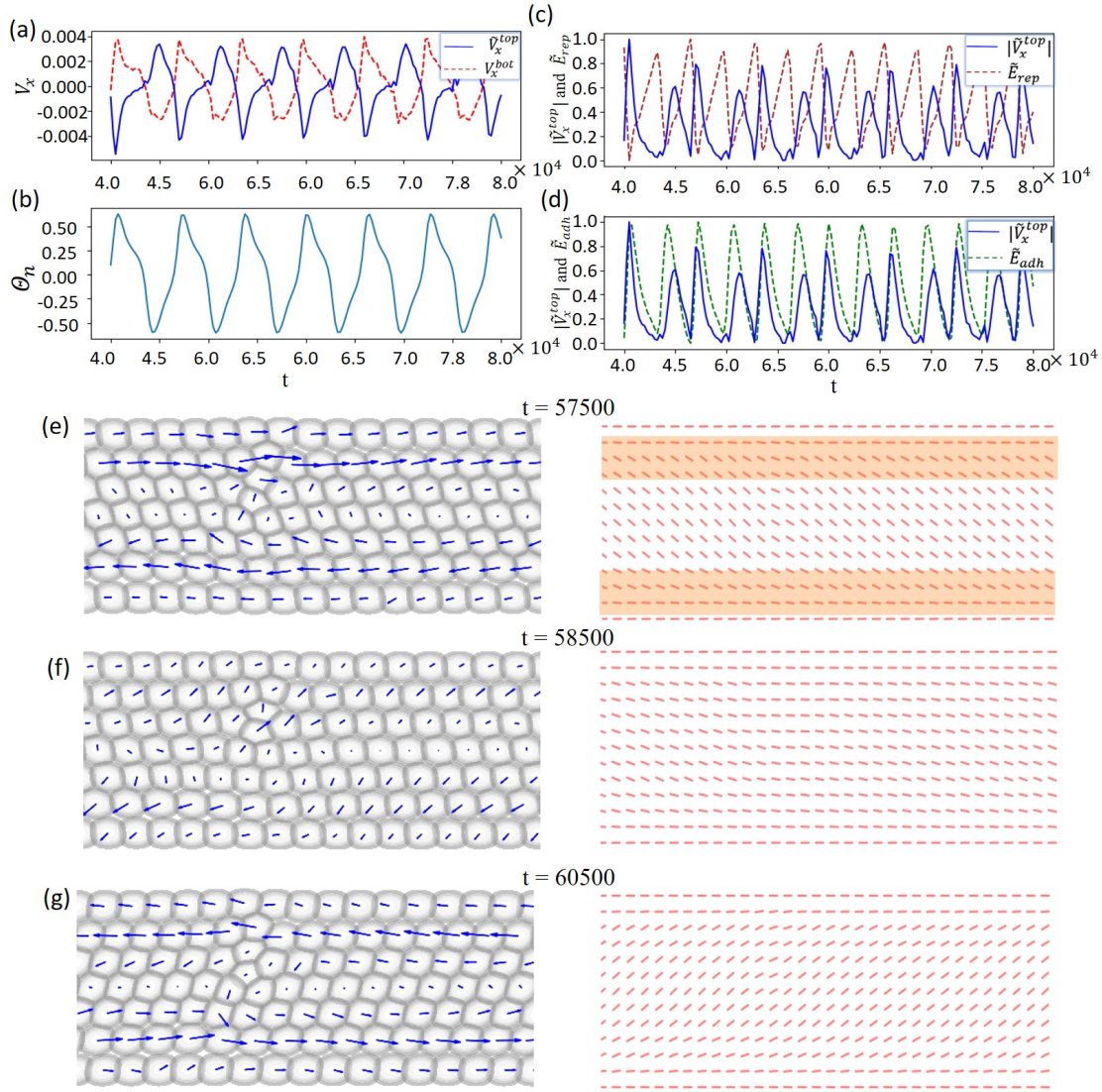


Figure 6.3: Oscillations: (a) average velocity for cells at the top strip, V_x^{top} (red, dashed line), and the bottom strip V_x^{bot} (blue, solid line). (b) average nematic angle, Θ_n, for cells in the middle part of the channel. (c) Rescaled repulsive energy, $\tilde{E}_{rep}$ (brown, dashed line), and rescaled average velocity for cells in the top strip, $\tilde{V}_x^{top}$ (blue, solid line). (d) Rescaled adhesive energy, $\tilde{E}_{adh}$ (green, dashed line), and rescaled average velocity for cells at the top strip, $\tilde{V}_x^{top}$ (blue, solid line). The left subfigures of (e), (f), (g) show snapshots of the cell oscillation (blue arrows show the centre of mass velocity of cells), and the subfigures on the right of (e), (f), (g) show the coarse-grained nematic director field (red bars). In (e), orange Region highlights the strong splay.

the tissue is in a nematic state with $\Theta_n \approx 0$ where the adhesive force is low and the splay of nematic directors is insignificant, but the tissue is at a high strain and a maximum of the repulsive energy (Fig. 6.3(f)). Therefore, the system is dominated by repulsive forcing. Then, the system returns to a state of a lower strain driven by the repulsion, implying that the repulsive forces restore the strain and contribute to the elasticity of the tissue. Similarly, the cell-cell adhesion diminishes the tissue elasticity and allows the tissue to create high strains. These results are consistent with our findings in Section 6.3.1. that the elasticity is enhanced at a high repulsion, and the tissue behaves more like an active viscous fluid with high cell-cell adhesion.

Interestingly, as we triple the length of the channel ($L_x \times L_y = 768 \times 112$) and keep the number density of cells the same, a wave-like pattern where the shear pattern propagates emerges. To investigate this feature, we plot the kymograph for the average velocity (Fig. 6.4) defined as $V_x = \int_0^{L_y} dy v_x(x, y)$. In the kymograph, the yellow and blue regions representing high velocities along the x (right) or $-x$ (left) direction propagate in time, indicating a mechanical wave behaviour.

To investigate the local properties for cells during this wave-like behaviour, we calculate the average velocity and orientation angle for cells in two windows located in the upper half and lower half of the channel respectively. Fig. 6.4 shows that the average velocity in the two windows is out of phase, but their orientation angles are in phase, revealing a local shear pattern.

6.3.4 Spontaneous shear flow

Spontaneous shear flow emerges as we increase the adhesive control parameter, ω, indicating a transition to the active-fluid-like behaviour (Fig. 6.5(a)). This state has been predicted by linear stability analysis and numerical calculations for active nematics in a viscous medium [114]. Different to the oscillating state, this shear flow pattern is in a sustained direction. Note that the cell-cell adhesion acts as a negative line tension term in our model, which prefers cell-cell contact but does not prevent the bidirectional shear flows.

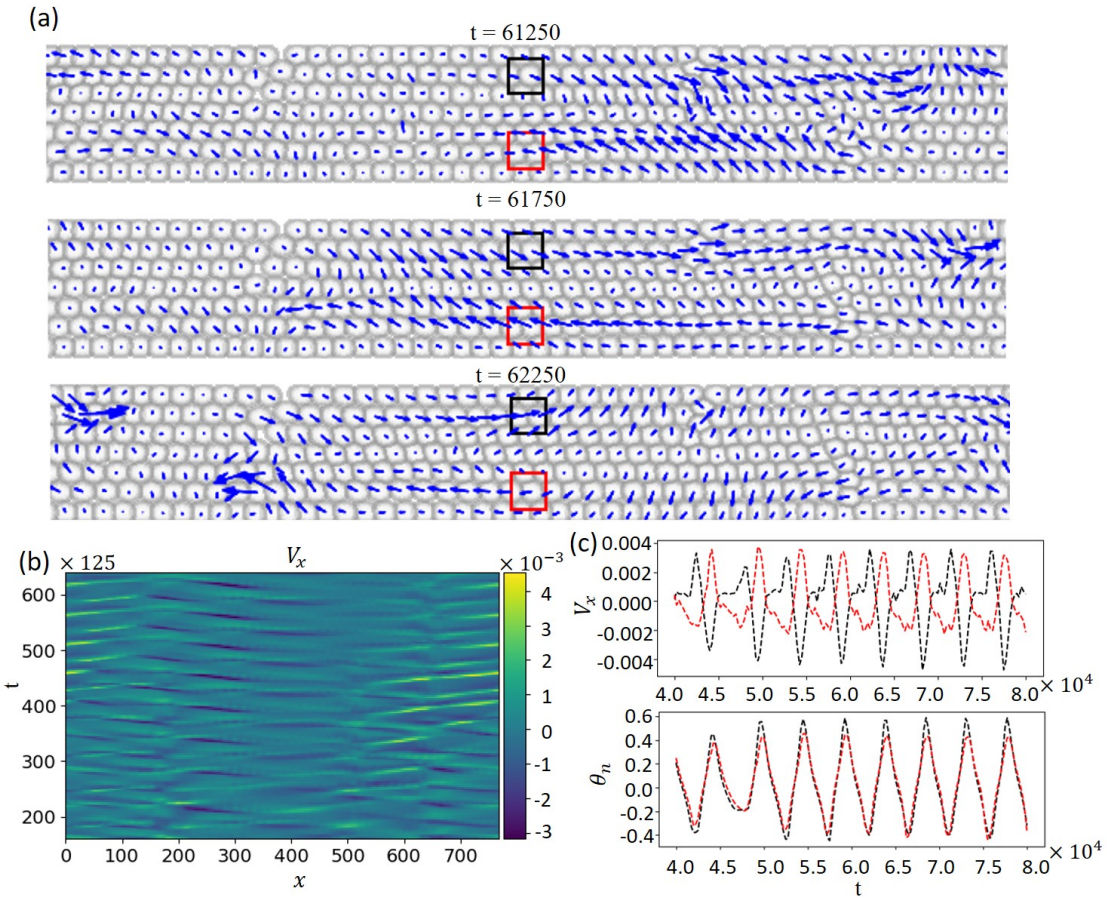


Figure 6.4: Wave-like behaviour: (a) Snapshots for the wave-like behaviour (b) kymograph for the velocity averaged over the y direction, V_x (c),(d) The average velocity and angle of directors for cells inside the windows of size 28 whose centres are located at (382,86) (the black square in (a))and (386,26) (the red square in (a)). $AR_0 = 1.0$, $\kappa = 4.0$ and $\omega = 0.7$ for this figure.

6.3.5 The effects of the cell aspect ratio

The aspect ratio of individual constituent elliptical colloids can change the rheology of the material [115]. For confluent tissue layers, various types of cells range from MDCK cells of isotropic shape to fibroblast cells with an aspect ratio larger than two. Here, we study the impact of the aspect ratio on the collective behaviour of cells in a channel. We first vary the target aspect ratio, AR_0, and calculate ΔV_x and ΔV_x^{abs}. Fig. 6.2(c) shows that both ΔV_x and ΔV_x^{abs} increase with AR_0 when $AR_0 < 1.2$, then ΔV_x and ΔV_x^{abs} plateau when $1.25 < AR_0 < 1.75$; they then further increase when $AR_0 > 1.75$. This result shows that a high aspect ratio makes

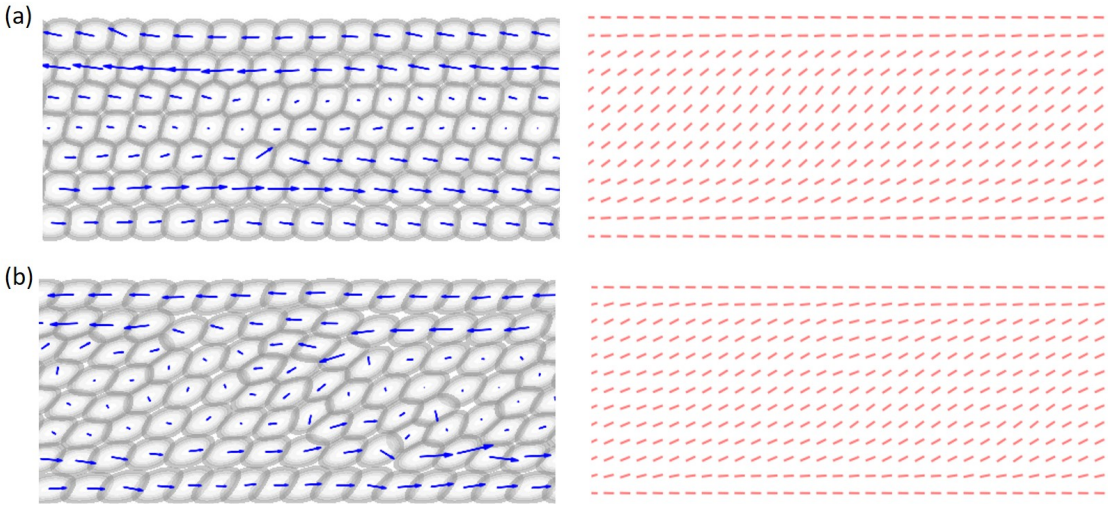


Figure 6.5: The shear flow state Snapshots for the shear flow states of (a) circular cells where $AR_0 = 1.0, \omega = 1.05$ and $\kappa = 4.0$ (b) naturally elongated cells where $AR_0 = 2.2, \omega = 0.6$ and $\kappa = 2.5$. The blue arrows show the centre of mass velocities. The subfigures on the right show the coarse-grained nematic director field (red bars).

the cells behave more like the wet active nematics as long and thin particles better resemble the nematic particles with better neighbour alignment.

Fig. 6.6 summarises the phase transitions between shear flow, oscillation and the jammed state for elliptical cells. Note that the oscillations only appears at $AR_0 \sim 1$. As the cell-cell adhesion parameter, ω, or the target aspect ratio, AR_0, increases, the spontaneous shear flow state emerges. A snapshot of the simulation is shown in Fig. 6.5(b).

6.4 Discussion

We have used a computational phase field model to study the dynamics of cells confined in a channel. A jammed, nematic state, cell oscillation and shear flow are observed, implying that the viscoelastic properties of the confluent cell layer can be changed by the interplay between active inter-cellular forcing and passive factors such as cell-cell repulsion, cell-cell adhesion and the natural aspect ratio of the cell. We find that high cell-cell repulsion drives the system to a jammed state. However, the negative line-tension-like, cell-cell adhesion and a high aspect ratio facilitate the formation of shear flow, showing a viscous, active nematic

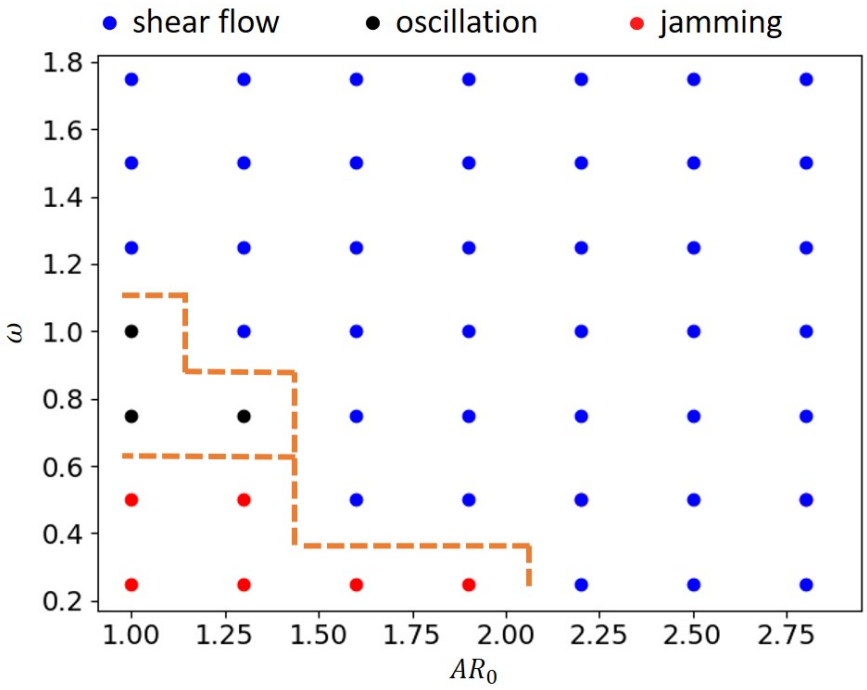


Figure 6.6: Phase diagram as a function of ω and AR_0 Simulations with $\Delta V_x^{abs} < 0.04$, $\Delta V_x < 0.04$ are classified as jammed states. Simulations with $\Delta V_x^{abs} > 0.065$, $\Delta V_x < 0.04$ are classified as oscillations, Simulations with $\Delta V_x > 0.065$ are classified as shear flow states. $\kappa = 3.0$ for this figure.

behaviour. The oscillatory shear state emerges for round cells ($AR_0 \sim 1$) as a result of the competition between the elasticity and the active inter-cellular force. Interestingly, this oscillatory behaviour changes to wave-like behaviour as the length of the channel significantly increases.

We focus on the nematic effects that emerge from inter-cellular forces. However, the polar force can give rise to oscillation and wave-like behaviour. In [116], a transition from oscillation to wave-like behaviour in confinement was observed in MDCK monolayers and was studied computationally by the vertex model. The polar force with neighbour alignment accounts for the emergence of these states in the vertex model [116]. A recent work studying feedback between the viscoelastic components of a fluid and the active nematic forcing using simplified equations based on hydrodynamic active nematic equations also predicts an oscillatory state [117].

In materials science, viscoelasticity can be studied by investigating the response of stress to shear strain. To probe this property, we apply a sinusoidal, dynamical

shear strain to a passive tissue ($\zeta_{\text{inter}} = 0$). The tissue stress lags the strain by a phase difference $\delta \approx 0.603$ (34.56^o) which is between 0 and $\pi/2$, the phase lag for purely elastic and viscous materials respectively, showing the passive tissue is viscoelastic (See Appendix C.4). However, the active inter-cellular force can change the viscoelastic behaviour of tissue [110, 111]. Quantitative measurements of strain-stress relations with the interplay between the active and passive forces remain to be explored in the future.

Our study gives a framework of how viscoelastic behaviours can result from inter-cellular forces and give rise to different dynamical behaviours. Although it is difficult to link the model parameters, such as cell-cell adhesion (ω) and repulsion (κ), directly to biological properties, the repulsion and adhesion may be varied by perturbing the properties of the plasma membrane [118].

7 Discussion

In this thesis, we studied how polar and dipolar forces contribute to the collective behaviour of confluent cell monolayers. Section 7.1 summarises the main results of this thesis. Section 7.2 provides a perspective for future research extending the methods we presented in this thesis.

7.1 Summary

In Chapter 1, we give the background about active matter and cell mechanics and briefly discuss how in-silico models are applied to study the collective behaviours of cell layers. We turn to the active nematic theory in Chapter 2. We first introduce the nematic order parameter describing nematic liquid crystals and then derive the active stress corresponding to a force dipole. We also discuss the self-propulsion ability of active defects and their significance in cell mechanics measurements. After presenting the theoretical background, we describe how we model the collective cell behaviour using the phase field model in Chapter 3. We introduce how the free energy captures the passive properties, such as deformability, cell-cell adhesion, cell-cell repulsion and area soft constraints. We then focus on modelling the polar and dipolar forces and propose different possible mechanisms for the dynamics

of the polarisation and the nematic directors. Moreover, we distinguish the self-deformation and inter-cellular dipolar forces and allow them to vary independently to investigate collective cell behaviours.

In Chapter 4, we investigate the interplay between the polar and dipolar forces by incorporating them into the active force density in the phase field model. We also compare the dynamics of a confluent cell monolayer when the polarity of the cells aligns to (i) their main axes of elongation, (ii) their velocity and (iii) when the polarity direction carries out a persistent random walk. We find that the cell velocity and neighbour rearrangement rate increase with either the polar or the dipolar activity, causing a transition from a jammed state to a liquid state. This transition is observed in all three ways to implement the polarisation dynamics. Moreover, different mechanisms of polarity alignment also lead to close measures of cell rearrangement rates, averaged cell deformation, and averaged cell velocity in the monolayer. A special type of collective motion where all the cells move in almost the same direction, the flocking state, is observed only for case (ii). The flocking state emerges with strong polar forces but disappears as the strength of the dipolar nematic activity increases.

We next turn to study how inter-cellular forces affect cell motility. Cells pull their neighbours through the cell-cell junctions by exerting contractile forces, which contribute to the collective behaviour of the cell sheet. We model these inter-cellular forces and investigate the nematic features of the monolayer in Chapter 5. We find that the active, contractile, inter-cellular interactions lead to cell elongation, nematic ordering, and active turbulence. However, extensile inter-cellular interactions favour perpendicular cell orientations. Also, we show that contractile behaviour could be changed to extensile behaviour by anisotropic fluctuations in inter-cellular forces.

We follow up the research on the inter-cellular forces in the previous chapter and study the interplay between the viscoelasticity and the inter-cellular contractile force in Chapter 6. A jammed, nematic state, collective cell oscillations and shear flow are observed, implying the viscoelasticity of the confluent cell layer can be changed by the interplay between active inter-cellular forcing and passive properties

such as cell-cell repulsion, cell-cell adhesion and the natural aspect ratio of the cell. The transitions between the jammed nematic state, oscillations and spontaneous shear flow emerge as the cell-cell adhesion increases. The cell-cell repulsion makes the system more jammed, and cells of a high aspect ratio favour the shear flow state. Moreover, wave-like behaviour is observed as the length of the channel increases in the regime where oscillations are observed.

7.2 Outlook

This thesis discusses several aspects of polar and dipolar contributions to collective cell behaviours in a confluent cell layer. It will be possible for future investigations in the open questions in cell mechanics by extending the framework we provided in this thesis. Here, I propose three interesting research questions for the future.

7.2.1 Mechanical waves during cell spreading

Collective cell spreading plays a significant role in tissue remodelling and wound healing. During the tissue expansion, a mechanical wave that propagates across the monolayer via inter-cellular force transmission has been reported in [119]. We propose that the interplay between the polar force at the two open ends of the tissue and the inter-cellular force in the bulk of the monolayer may account for this mechanical wave behaviour. To model the tissue expansion, we can modify the simulation configuration by introducing walls and obstacles to mimic the stencils where cells are cultured in the experiments and then study the cell spreading by removing them later in the simulations. We can use the polar and inter-cellular dipolar force described in Chapter 3 to explore this problem computationally with the phase field model.

7.2.2 Mechanochemical Coupling

Biological functions, such as the morphogenesis of cells, are driven by different mechanical properties, such as the pressure, density, and deformation of cells. Cells can adjust their mechanical properties via chemical morphogen signalling. How the

coupling between chemical and mechanical cues gives rise to morphogenesis remains unclear [120]. For example, experiments have shown that the feedback of cell area and ERK, a contractility-related chemical morphogen, gives rise to the propagation of ERK waves spanning the cell layer, which helps the cell spreading [121, 122]. We can model this mechanochemical coupling by defining the local ERK concentrations of each cell in our phase field model. Then we may model the feedback between ERK concentration and the cell area using appropriate differential equations.

7.2.3 Cell sorting by active inter-cellular force

Cell sorting is a process where cells separate or aggregate spatially by their types. The well-known differential adhesion hypothesis, where cell-cell adhesion is different among different species, was proposed to explain the mechanism [123]. In this scenario, cell sorting can be treated as a thermal process where cells of the same type aggregate together to minimise the free energy of the whole system. However, recent experiments [13] suggest that differentiation in active inter-cellular forces can also give rise to cell sorting. It is interesting to study whether anisotropic fluctuations in the inter-cellular forces can explain this effect. We expect that varying fluctuations among different cell species may give rise to effective contractile or extensile behaviours, which may lead to cell sorting.

Appendices

A

Implementaion of the model

Contents

A.1 Finite difference 85
A.2 Predictor-corrector method 86
A.3 Euler-Maruyama method 86

In this thesis, we calculate the phase-field dynamics using Eq. 3.1. These calculations are implemented using a finite difference method for the spatial derivatives and a predictor-corrector method for the update in time. The stochastic relaxation processes in Section 3.3.2 and 3.3.1 are implemented using Euler-Maruyama method. In this section, we discuss these methods in detail.

A.1 Finite difference

We use the second-order finite difference method to calculate the spatial derivatives. The first order spatial derivative is calculated by

$$\frac{\partial \varphi^{(i)}(x,y,t)}{\partial x} = \frac{1}{2h}[\varphi^{(i)}(x+h,y,t) - \varphi^{(i)}(x-h,y,t)] + O(h^2), \tag{A.1}$$

$$\frac{\partial \varphi^{(i)}(x,y,t)}{\partial y} = \frac{1}{2h}[\varphi^{(i)}(x,y+h,t) - \varphi^{(i)}(x,y-h,t)] + O(h^2). \tag{A.2}$$

The Laplacian of $\varphi^{(i)}$ is

$$\nabla^2\varphi^{(i)}(x,y,t) = \frac{1}{h^2}[\varphi^{(i)}(x,y+h,t) + \varphi^{(i)}(x,y-h,t) \tag{A.3}$$

$$+ \varphi^{(i)}(x+h,y,t) + \varphi^{(i)}(x-h,y,t) - 4\varphi^{(i)}(x,y,t)] + O(h^2) \tag{A.4}$$

where h is the lattice grid spacing.

A.2 Predictor-corrector method

The predictor-corrector method is used to update the phase field in time. The phase-field $\varphi^{(i)}$ is updated by the corrector step.

$$\varphi^{(i)}(x,y,t+\Delta t) \approx \varphi^{(i)}(x,y,t) + \frac{1}{2}(\Delta\varphi^{(i)} + \Delta\tilde{\varphi}^{(i)}) \tag{A.5}$$

where $\Delta\varphi^{(i)}$ is the first order difference in time,

$$\Delta\varphi^{(i)} = -\Delta t[\mathbf{v}^{(i)}(\{\varphi^{(n)}(x,y,t)\})\cdot\nabla\varphi^{(i)}(x,y,t) + J_0\frac{\delta\mathcal{F}(\{\varphi^{(n)}(x,y,t)\})}{\delta\varphi^{(i)}(x,y,t)}]. \tag{A.6}$$

$\Delta\tilde{\varphi}^{(i)}$ is the difference in time predicted by the predictor $\tilde{\varphi}^{(i)}(x,y,t+\Delta t)$, which is defined as

$$\Delta\tilde{\varphi}^{(i)} = -\Delta t[\mathbf{v}^{(i)}(\{\tilde{\varphi}^{(n)}(x,y,t+\Delta t)\})\cdot\nabla\tilde{\varphi}^{(i)}(x,y,t+\Delta t) - J_0\frac{\delta\mathcal{F}(\{\tilde{\varphi}^{(n)}(x,y,t+\Delta t)\})}{\delta\tilde{\varphi}^{(i)}(x,y,t+\Delta t)}] \tag{A.7}$$

The predicted phase-field is defined as

$$\tilde{\varphi}^{(i)}(x,y,t+\Delta t) = \varphi^{(i)}(x,y,t) + \Delta\varphi^{(i)} \tag{A.8}$$

Note that here we write the local velocity field as a function of the phase-field.

A.3 Euler-Maruyama method

One of the simplest approximation methods for the stochastic process is the Euler-Maruyama update [124]. We use it to calculate the equations related to the dynamics of polarisation and the nematic directors. We calculate Eq. 3.17 numerically by

$$\theta_p^{(i)}(t+\Delta t) \approx \theta_p^{(i)}(t) - J_{\mathrm{pol}}|\mathbf{v}_{\mathrm{COM}}^{(i)}(t)|\angle(\mathbf{p}^{(i)}(t), \mathbf{v}_{\mathrm{COM}}^{(i)}(t)) + D_{\mathrm{pol}}\sqrt{\Delta t}\,\eta^{(i)}(t). \tag{A.9}$$

We calculate Eq. 3.19 numerically by

$$\theta_p^{(i)}(t+\Delta t) \approx \theta_p^{(i)}(t) - J_{\mathrm{pol}} D^{(i)}(t) \angle(\mathbf{p}^{(i)}(t), \mathbf{d}_{\parallel}^{(i)}(t)) + D_{\mathrm{pol}} \sqrt{\Delta t}\, \eta^{(i)}(t). \quad \text{(A.10)}$$

We calculate Eq. 3.20 numerically by

$$\theta_p^{(i)}(t+\Delta t) \approx \theta_p^{(i)}(t) + D_{\mathrm{pol}} \sqrt{\Delta t}\, \eta^{(i)}(t). \quad \text{(A.11)}$$

We calculate Eq. 3.21 numerically by

$$\theta_n^{(i)}(t+\Delta t) \approx \theta_n^{(i)}(t) - J_{\mathrm{nem}} \angle(\mathbf{n}^{(i)}(t), \mathbf{d}_{\parallel}^{(i)}(t)) + D_{\mathrm{nem}} \sqrt{\Delta t}\, \eta^{(i)}(t). \quad \text{(A.12)}$$

To calculate Eq. 3.22 numerically, we first decompose the anisotropic noise vector by

$$\boldsymbol{\eta}^{(i)}(t) = \sqrt{D_{\parallel}} x_1^{(i)}(t) \mathbf{d}_{\parallel}^{(i)} + \sqrt{D_{\perp}} x_2^{(i)}(t) \mathbf{d}_{\perp}^{(i)} \quad \text{(A.13)}$$

where $x_1^{(i)}(t)$ and $x_2^{(i)}(t)$ are two independent random number drawn from a standard Gaussian distribution at time t. Then, we calculate Eq. 3.22 nummerically by

$$\mathbf{n}^{(i)}(t+\Delta t) = \mathbf{n}^{(i)}(t) + J_n(\mathbf{d}_{\parallel}^{(i)}(t) - \mathbf{n}^{(i)}(t)) + \sqrt{\Delta t}[\sqrt{D_{\parallel}} \mathbf{d}_{\parallel}^{(i)}(t) x_1^{(i)}(t) + \sqrt{D_{\perp}} \mathbf{d}_{\perp}^{(i)}(t) x_2^{(i)}(t)]. \quad \text{(A.14)}$$

B

Measurements: center of mass, velocity, cell orientation and defect detection

In our phase-field approach, we need to keep measuring some quantities at each time step to implement the model. For example, we must know each cell's centre of mass velocity to implement the equation aligning the cell polarisation to its centre of mass velocity, Eq. 3.17. Other measurements, such as the velocity field, cell orientation field, and the positions of defects, are essential in interpreting the physics behind collective cell motility. We will discuss them in the following sections.

B.1 Cell velocity

The centre-of-mass position of cell i is defined as

$$\mathbf{x}_{com}^{(i)} = \frac{\int d\mathbf{x}\varphi^{(i)}(\mathbf{x})\mathbf{x}}{\int d\mathbf{x}\varphi^{(i)}(\mathbf{x})}. \tag{B.1}$$

Taking the time derivative of $\mathbf{x}_{com}^{(i)}$ gives the centre of mass velocity,

$$\mathbf{v}_{com}^{(i)} = \frac{d\mathbf{x}_{com}^{(i)}}{dt} = \frac{1}{A}[\int d\mathbf{x}\ \mathbf{x}\frac{\partial\varphi^{(i)}}{\partial t} - \mathbf{x}_{com}^{(i)}\int d\mathbf{x}\frac{\partial\varphi^{(i)}}{\partial t}] \tag{B.2}$$

where $A = \int d\mathbf{x}\phi^{(i)}(\mathbf{x})$, and $\frac{\partial\varphi^{(i)}}{\partial t}$ is obtained from the dynamic equation of the phase-field, Eq. 3.1. Note that for the periodic boundary condition, the centre

of mass can also be written as

$$\mathbf{x}^{(i)}_{com,x} = \frac{L_x}{2\pi}\arg(\int_0^{L_x} dx \int_0^{L_y} dy\ \varphi^{(i)}(x,y)e^{i2\pi x/L_x}) \tag{B.3}$$

$$\mathbf{x}^{(i)}_{com,y} = \frac{L_y}{2\pi}\arg(\int_0^{L_x} dx \int_0^{L_y} dy\ \varphi^{(i)}(x,y)e^{i2\pi x/L_y}) \tag{B.4}$$

where $\mathbf{x}^{(i)}_{com,x}$ and $\mathbf{x}^{(i)}_{com,y}$ are x and y coordinate for the centre mass of cell i.

B.2 Deformation tensor and cell orientation

We follow the steps in [125] to show how the deformation tensor 3.18 is calculated. If a n-dimensional function $f(\mathbf{x})$ is linearly symmetric, it is constituted of a family of isovalue, n-1 dimensional, parallel hyperplanes quantified by a unit vector $\hat{\mathbf{k}}_\mathbf{0}$. The Fourier transform of a linearly symmetric function is distributed along the line parallel to $\hat{\mathbf{k}}_\mathbf{0}$ and passes the origin in Fourier domain. In the spirit of finding $\hat{\mathbf{k}}_\mathbf{0}$, we can define an effective energy function, $V[f]$, in Fourier domain to measure how well $f(\mathbf{x})$ concentrates along $\hat{\mathbf{k}}_\mathbf{0}$. It reads

$$V[f] = \int d^n x'\ |\hat{f}(\mathbf{x}')|^2 d^2(\mathbf{x}', \hat{\mathbf{k}}_\mathbf{0}) \tag{B.5}$$

where x' is the coordinate in the Fourier domain, $\hat{f}(\mathbf{x}')$ is the Fourier transform of $f(\mathbf{x})$, and

$$d^2(\mathbf{x}', \hat{\mathbf{k}}_\mathbf{0}) = (\mathbf{x}' - \mathbf{x}'^\mathbf{T}\hat{\mathbf{k}}_\mathbf{0}\hat{\mathbf{k}}_\mathbf{0})^T(\mathbf{x}' - \mathbf{x}'^\mathbf{T}\mathbf{k}_0\hat{\mathbf{k}}_\mathbf{0}) = \hat{\mathbf{k}}_\mathbf{0}^T(\mathbf{I}\mathbf{x}'^T\mathbf{x}' - \mathbf{x}'\mathbf{x}'^T)\hat{\mathbf{k}}_\mathbf{0} \tag{B.6}$$

is the square of the Euler distance from point $\mathbf{x}'$ to the line that passes the origin and is parallel to $\hat{\mathbf{k}}_\mathbf{0}$. Thus, we can rewrite $V[f]$ in terms of matrix multiplications.

$$V[f] = \hat{\mathbf{k}}_\mathbf{0}^T\mathbf{J}\hat{\mathbf{k}}_\mathbf{0} \tag{B.7}$$

where

$$J_{ii} = \frac{1}{4\pi^2}\int d^n x' \sum_{j\neq i} x_j'^2 |\hat{f}(\mathbf{x}')|^2 \tag{B.8}$$

$$J_{ij} = -\frac{1}{4\pi^2}\int d^n x' x_i' x_j' |\hat{f}(\mathbf{x}')|^2 \quad (i \neq j) \tag{B.9}$$

The unit vector $\hat{\mathbf{k}}_\mathbf{0}$ that minimises $V[f]$ gives the orientation of function $f(\mathbf{x})$. Eq. B.7 shows that $V[f]$ is minimised or maximised when $\hat{\mathbf{k}}_\mathbf{0}$ is the unit eigenvector of $\mathbf{J}$ corresponding to the minimum eigenvalue or the maximum eigenvalue respectively. Thus, we convert the problem of finding the linearly symmetric axis of $f(\mathbf{x})$ to calculating the eigenvectors of matrix $\mathbf{J}$. Interestingly, it is possible to compute $\mathbf{J}$ in the spatial domain. Using the Parseval relation, we get

$$J_{ii} = \int d^n x \ \sum_{j \neq i} (\frac{\partial f(\mathbf{x})}{\partial x_j})^2 \tag{B.10}$$

$$J_{ij} = -\int d^n x \ \frac{\partial f(\mathbf{x})}{\partial x_i} \frac{\partial f(\mathbf{x})}{\partial x_j} \quad (i \neq j) \tag{B.11}$$

As adding a multiple of identity matrix to a matrix does not change its eigenvectors ($\mathbf{J}$ and $\mathbf{J} - c\mathbb{I}$ have the same set of eigenvectors), we can define the traceless deformation tensor for the phase field $\varphi^{(i)}$,

$$\mathcal{D}^{(i)} = -\int d\mathbf{x} \left\{ \nabla\varphi^{(i)} \nabla\varphi^{(i)^T} - \frac{\mathbb{I}}{2} \mathrm{Tr}(\nabla\varphi^{(i)} \nabla\varphi^{(i)^T}) \right\}, \tag{B.12}$$

to quantify the orientation of $\varphi^{(i)}$. Note that in two-dimension, the eigenvector of $\mathcal{D}^{(i)}$ corresponding to the positive eigenvalues, along and perpendicular to the elongation the axis of the cell and the angle $\theta_d^{(i)} = \arctan(\mathcal{D}_{xy}^{(i)} / \mathcal{D}_{xx}^{(i)})$ can be defined for the cell orientation.

B.2.1 Coarse-grained fields

We define the tissue velocity field by

$$\mathbf{v}(\mathbf{x}) = \sum_i \varphi^{(i)} \mathbf{v}_{com}^{(i)}. \tag{B.13}$$

The coarse-grained deformation tensor can be defined as

$$\mathcal{D}(\mathbf{x}) = \sum_i \varphi^{(i)}(\mathbf{x}) \mathcal{D}^{(i)}. \tag{B.14}$$

Thus, the coarse-grained field for orientation angle is

$$\theta_d(\mathbf{x}) = \frac{1}{2} \arctan(\mathcal{D}_{xy}(\mathbf{x}) / \mathcal{D}_{xx}(\mathbf{x})). \tag{B.15}$$

These coarse-grained fields are then smoothed by applying a sliding window of size $3R \times 3R$ to filter out the noise.

B.2.2 Defect detection

We first calculate the coarse-grained field for the orientation angle using Eq. B.15. Then we calculate the topological charge at each lattice point by examining the change of orientation angle of its 8 neighbouring lattice points around an anticlockwise closed loop, and label defects at the points with charge +1/2 or -1/2 (Fig. B.1) [126].

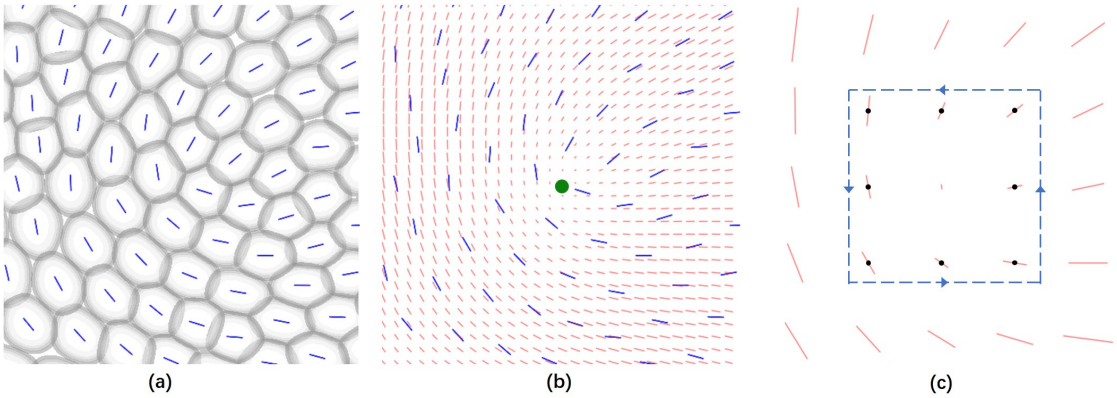


Figure B.1: (a) Snapshot of the cells and their elongation axes (blue bars) around a +1/2 defect in the confluent monolayer. (b) The coarse-grained orientation field (red bars) is overlaid by the elongation axis of the cells (long blue bars). The green dot labels the defect core. (c) The orientation field(red bars) around the +1/2 defect. The topological charge of the centre point is calculated by examining the change of orientation angle of its 8 neighbouring lattice points (the black dots) around the anticlockwise closed loop (the dashed line in blue).

We crop and align the fields around each defect and average over all the defects for all time steps to get the average orientation field and the velocity field around the defects (Fig. 5.2).

C Additional comments

We will discuss how we implement the cell-cell adhesion to improve the numerical stability and also list the supplementary figures for Chapter 5 in this appendix.

C.1 The cell-cell adhesion

The passive cell-cell adhesive force for cell i follows from the free energy as

$$\mathbf{f}_{\mathrm{adh}}^{(i)}(\mathbf{x}) = \frac{\delta \mathcal{F}^{\mathrm{adh}}}{\delta \varphi^{(i)}} \nabla \varphi^{(i)} = \omega \lambda \nabla \varphi^{(i)} \sum_{j \neq i} \nabla^2 \varphi^{(j)}. \tag{C.1}$$

However, the cell-cell adhesion then tends to make the cell interface sharper and hence its Laplacian larger, which can lead to unstable numerical behaviour easily [90, 93]. When the cell-cell adhesion overcomes the Cahn-Hilliard term which stabilises the cell interface, the cells come increasingly close leading to an increasingly large Laplacian which further enhances the cell-cell adhesion. This positive feedback can cause simulation instabilities. By introducing the modification $g(\nabla^2\varphi)$, we suppress too high cell-cell adhesions and thus make the simulations more stable by define a modified adhesive force to improve the numerical stability:

$$\tilde{\mathbf{f}}_{\mathrm{adh}}^{(i)}(\mathbf{x}) = \omega \lambda \nabla \varphi^{(i)} \sum_{j \neq i} g(\nabla^2 \varphi^{(j)}). \tag{C.2}$$

The function is defined as $g(w) = \frac{w}{\sqrt{1+(w/M)^2}}$. M is the maximum value of $g(w)$ and has the same units as w. We set $M = 1/\Delta x^2$ for $g(\nabla^2\varphi)$. where Δx is the

lattice spacing. We remark that $\tilde{\mathbf{f}}^{(i)}_{\text{adh}} \approx \mathbf{f}^{(i)}_{\text{adh}}$ when $\nabla^2\varphi^{(j)} << M$. A similar formulation is used in [86].

C.2 Supplementary figures for Chapter 5

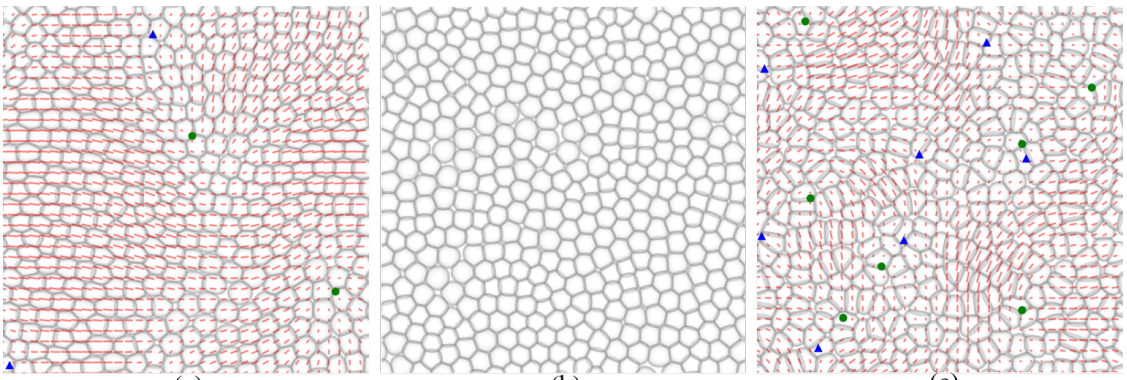


Figure C.1: Systems with both inter-cellular and self deformation forces Simulation snapshots with (a) a contractile system with a small self-contractility and a strong inter-cellular contractility $\zeta_{\text{inter}} = -0.6$, $\zeta_{\text{self}} = -0.1$. The self-contractility does not qualitatively change the behaviour. (b) a jammed system with commensurate self and inter-cellular contractility $\zeta_{\text{inter}} = -0.6, \zeta_{\text{self}} = -0.4$, cell elongation axes are not shown as cells are nearly isotropic. This is because the intracellular contractile force is strong enough to counter the effective extensile forces on a given cell due to intercellular interactions so the cells do not elongate. (c) a extensile system with a small self-contractility and a strong inter-cellular extensility $\zeta_{\text{inter}} = +0.4$, $\zeta_{\text{self}} = -0.1$. The self-contractility does not qualitatively change the behaviour. $\omega = 0.0$ for (a), (b) and (c).

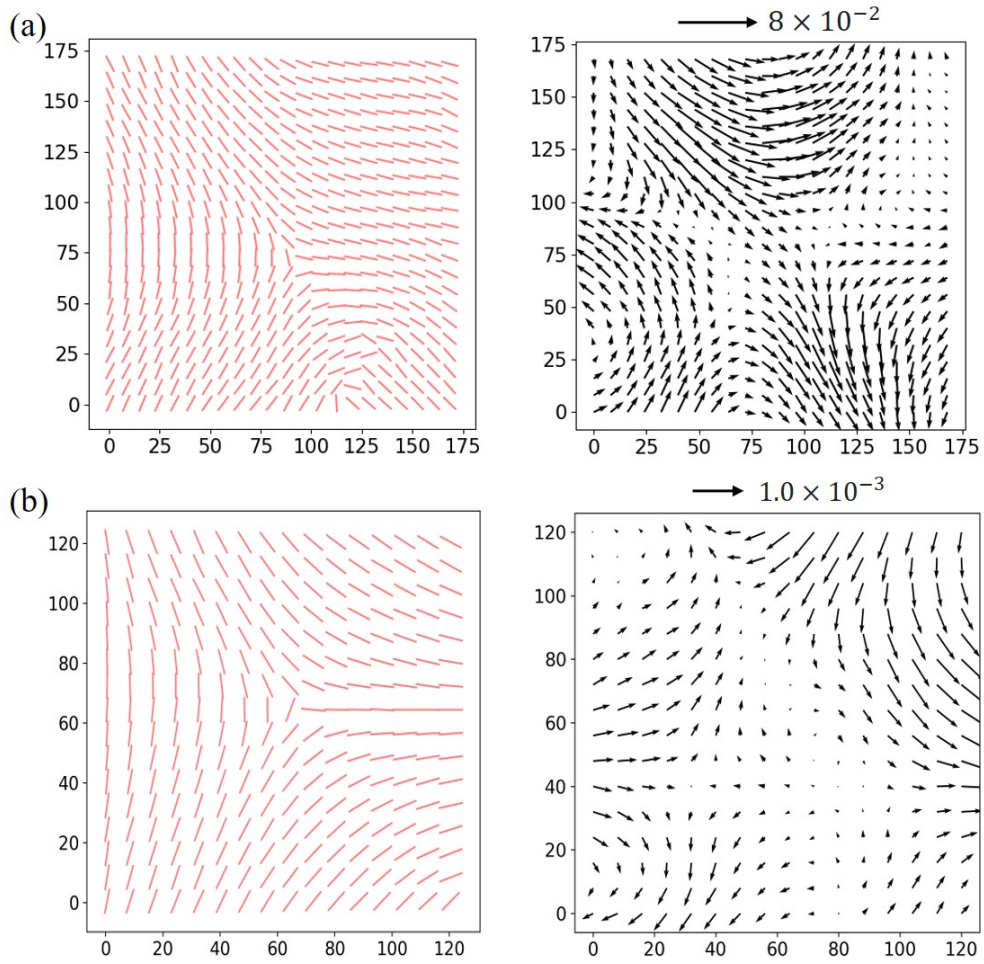


Figure C.2: Trefoil-like, -1/2, defects in simulations without fluctuations. Averaged cell elongation axes (left) and velocity (right) fields in the vicinity of a $-1/2$ defect for (a) a contractile system with $\zeta_{\text{inter}} = -0.6$ (b) a extensile system with $\zeta_{\text{inter}} = +0.4$. Note the scale change in the velocity between the contractile and extensile cases. 86 and 529 -1/2 defects are averaged for (a) and (b) respectively

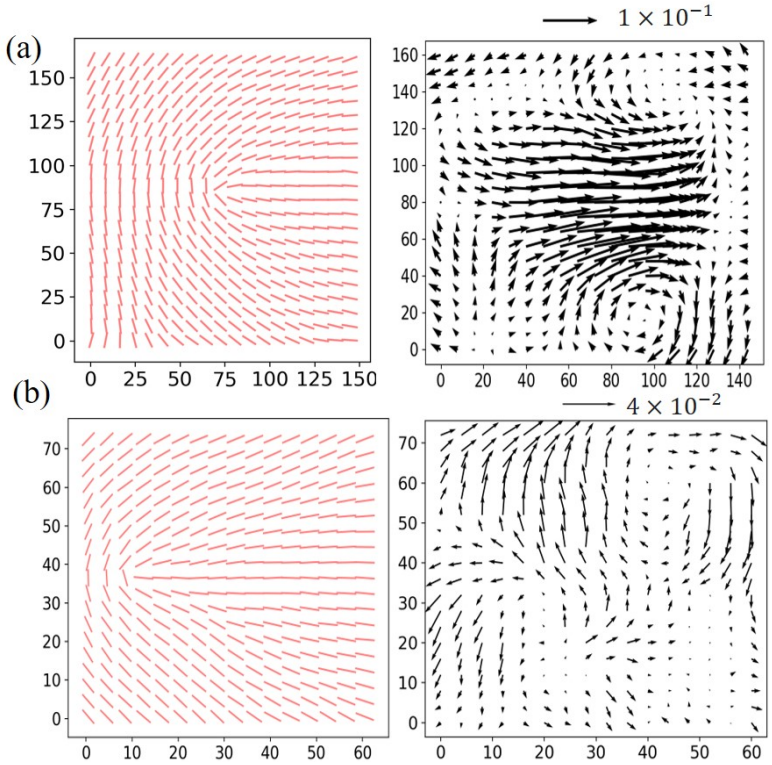


Figure C.3: Behaviour of comet-like, $+1/2$, defects as anisotropic fluctuations are introduced. Averaged cell elongation axes (left) and velocity (right) fields in the vicinity of a $+1/2$ defect for (a) a contractile system with with anisotropic fluctuations which enhance its contractility $\zeta_{\text{inter}} = -0.4, D_{\parallel} = 0.2, D_{\perp} = 0.0, \omega = 0.0$. (b) a contractile system with anisotropic fluctuations which result in extensile-like behaviour $\zeta_{\text{inter}} = -0.4, D_{\parallel} = 0.1, D_{\perp} = 0.6, \omega = 0.0$. 97 and 621 $+1/2$ defects are averaged for (a) and (b) respectively

C.3 Supplementary information for Chapter 6

C.3.1 Oscillation period

To investigate the relation between the oscillation period and the cell-cell adhesion, we plot the oscillation frequency against the cell-cell adhesion control parameter, ω. The figure below shows that the oscillation period, T, increases with cell-cell adhesion.

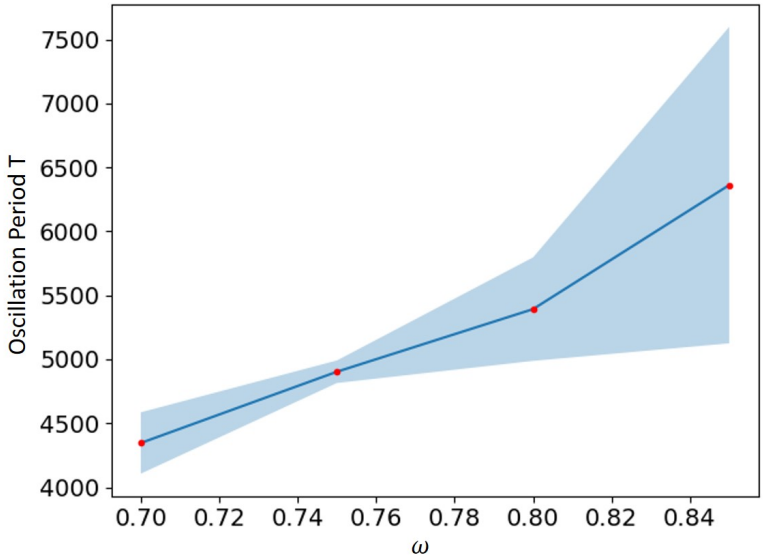


Figure C.4: Oscillation period: The oscillation period as a function of the cell-cell adhesion ω. $AR_0 = 1.0$ and $\kappa = 4.0$ for this figure.

C.4 Viscoelastic behaviour of passive tissue

To investigate the viscoelastic behaviour, we apply a sinusoidal, dynamical shear strain

$$\epsilon_{xy} = \epsilon_0 \sin \frac{2\pi}{T_s} t$$

to a passive tissue ($\zeta_{\text{inter}} = 0$) by adding two confining walls at the the left and right edges of the tissue and varying the slope of them over time, where ϵ_0 is the strain amplitude, and T_s is the period of the strain. We choose $\epsilon_0 = 1/7$ and $T_s = 20000$ to make the process slow and free of neighbour exchange.

According to materials theory, the stress σ_{xy} lags the sinusoidal strain by a phase difference, δ. Thus,

$$\sigma_{xy} = \sigma_0 \sin(\frac{2\pi}{T_s}t + \delta)$$

where σ_0 is the stress amplitude. $\delta = 0$ and $\delta = \pi/2$ for purely elastic material and for purely viscous material respectively.

To investigate the phase difference, we measure the tissue stress $\sigma_{\alpha\beta}$ by

$$\sigma_{\alpha\beta} = \frac{\sum A^{(i)}\sigma^{(i)}_{\alpha\beta}}{\sum A^{(i)}}, \tag{C.3}$$

where

$$\sigma^{(i)}_{\alpha\beta} = \frac{1}{A^i}\int d\mathbf{x}\ \frac{1}{2}(f^{(i)}_{\alpha}x_{\beta} + f^{(i)}_{\beta}x_{\alpha}) \tag{C.4}$$

is the coarse-grained equilibrium cell stress [127–129] and $A^{(i)}$ is the area of a cell. $f^{(i)}_{\alpha}$ is the α ($\alpha = x$ or y) component of the force density exerted on cell i which equals the passive force density in this case. x_α is the α component of position vector $\mathbf{x}$. Note that the passive cell dynamics under this dynamical strain ($\epsilon_0 = 1/7$ and $T_s = 20000$) is extremely slow and is considered quasi-equilibrium, so the equilibrium stress, Eq. C.4 is used for the stress calculation.

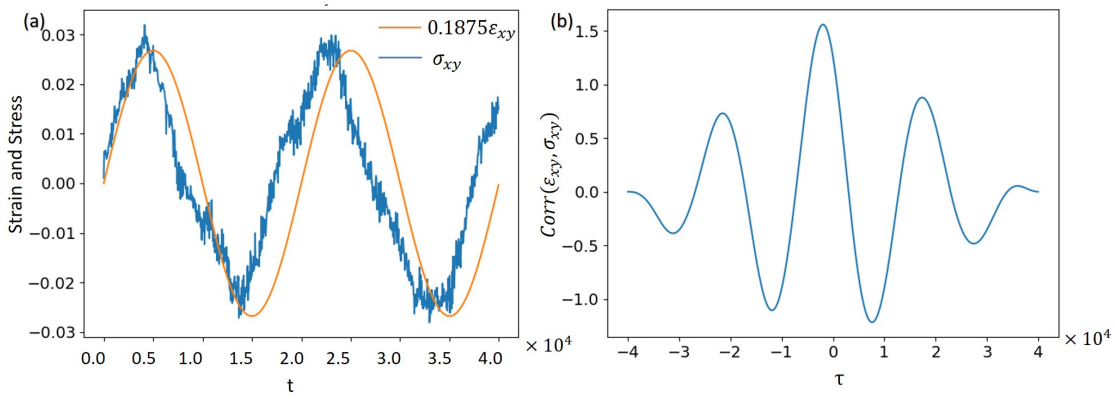


Figure C.5: Viscoelastic behaviour for the passive tissue: (a) The shear strain,ϵ_{xy} and tissue stress σ_{xy} as a function of time. (b) The cross-correlation between ϵ_{xy} and σ_{xy}. It peaks at $\tau \approx -1920$ which corresponds to $\delta \approx 0.603$ (34.56^o). $AR_0 = 1.0$, $\kappa = 4.0$, $\omega = 0.75$ and $\zeta_{\text{inter}} = 0$ for this figure.

Fig. C.5(a) shows that the shear strain and stress of the tissue. Then, We compute the cross-correlation between ϵ_{xy} and σ_{xy},

$$\text{Corr}(\tau) = \int dt\ \epsilon_{xy}(t-\tau)\sigma_{xy}(t), \tag{C.5}$$

where τ is the time shift, and quantify δ by the time shift corresponding to the maximum cross-correlation. Fig.C.5(b) shows that the cross-correlation peaks at $\tau \approx -1920$. This time shift corresponds to $\delta \approx 0.603$ (34.56^o) for the passive tissue, showing a viscoelastic behaviour.

References

[1]T. Sanchez, D. T. Chen, S. J. DeCamp, M. Heymann, and Z. Dogic, "Spontaneous motion in hierarchically assembled active matter", Nature **491**, 431–434 (2012).

[2]E. Rozbicki, M. Chuai, A. I. Karjalainen, F. Song, H. M. Sang, R. Martin, H.-J. Knölker, M. P. MacDonald, and C. J. Weijer, "Myosin-ii-mediated cell shape changes and cell intercalation contribute to primitive streak formation", Nature cell biology **17**, 397–408 (2015).

[3]T. E. Angelini, E. Hannezo, X. Trepat, M. Marquez, J. J. Fredberg, and D. A. Weitz, "Glass-like dynamics of collective cell migration", Proceedings of the National Academy of Sciences **108**, 4714–4719 (2011).

[4]M. C. Marchetti, J.-F. Joanny, S. Ramaswamy, T. B. Liverpool, J. Prost, M. Rao, and R. A. Simha, "Hydrodynamics of soft active matter", Reviews of modern physics **85**, 1143 (2013).

[5]T. Vicsek, A. Czirók, E. Ben-Jacob, I. Cohen, and O. Shochet, "Novel type of phase transition in a system of self-driven particles", Physical review letters **75**, 1226 (1995).

[6]J. Toner and Y. Tu, "Long-range order in a two-dimensional dynamical xy model: how birds fly together", Physical review letters **75**, 4326 (1995).

[7]A. Doostmohammadi, S. P. Thampi, and J. M. Yeomans, "Defect-mediated morphologies in growing cell colonies", Physical review letters **117**, 048102 (2016).

[8]K. Kawaguchi, R. Kageyama, and M. Sano, "Topological defects control collective dynamics in neural progenitor cell cultures", Nature **545**, 327–331 (2017).

[9]S. Ramaswamy and M. Rao, "Active-filament hydrodynamics: instabilities, boundary conditions and rheology", New Journal of Physics **9**, 423 (2007).

[10]S. P. Thampi, R. Golestanian, and J. M. Yeomans, "Instabilities and topological defects in active nematics", EPL (Europhysics Letters) **105**, 18001 (2014).

[11]G. Duclos, C. Erlenkämper, J.-F. Joanny, and P. Silberzan, "Topological defects in confined populations of spindle-shaped cells", Nature Physics **13**, 58–62 (2017).

[12]T. B. Saw, A. Doostmohammadi, V. Nier, L. Kocgozlu, S. Thampi, Y. Toyama, P. Marcq, C. T. Lim, J. M. Yeomans, and B. Ladoux, "Topological defects in epithelia govern cell death and extrusion", Nature **544**, 212–216 (2017).

[13]L. Balasubramaniam, A. Doostmohammadi, T. B. Saw, G. H. N. S. Narayana, R. Mueller, T. Dang, M. Thomas, S. Gupta, S. Sonam, A. S. Yap, et al., "Investigating the nature of active forces in tissues reveals how contractile cells can form extensile monolayers", Nature materials **20**, 1156–1166 (2021).

[14]B. Ladoux and R.-M. Mège, "Mechanobiology of collective cell behaviours", Nature reviews Molecular cell biology **18**, 743–757 (2017).

[15]M. Murrell, P. W. Oakes, M. Lenz, and M. L. Gardel, "Forcing cells into shape: the mechanics of actomyosin contractility", Nature reviews Molecular cell biology **16**, 486–498 (2015).

[16]B. Ladoux and A. Nicolas, "Physically based principles of cell adhesion mechanosensitivity in tissues", Reports on Progress in Physics **75**, 116601 (2012).

[17]F. Huber, J. Schnauß, S. Rönicke, P. Rauch, K. Müller, C. Fütterer, and J. Käs, "Emergent complexity of the cytoskeleton: from single filaments to tissue", Advances in physics **62**, 1–112 (2013).

[18]A. Brugués, E. Anon, V. Conte, J. H. Veldhuis, M. Gupta, J. Colombelli, J. J. Muñoz, G. W. Brodland, B. Ladoux, and X. Trepat, "Forces driving epithelial wound healing", Nature physics **10**, 683–690 (2014).

[19]A. Ravasio, I. Cheddadi, T. Chen, T. Pereira, H. T. Ong, C. Bertocchi, A. Brugues, A. Jacinto, A. J. Kabla, Y. Toyama, et al., "Gap geometry dictates epithelial closure efficiency", Nature communications **6**, 1–13 (2015).

[20]L. Petitjean, M. Reffay, E. Grasland-Mongrain, M. Poujade, B. Ladoux, A. Buguin, and P. Silberzan, "Velocity fields in a collectively migrating epithelium", Biophysical journal **98**, 1790–1800 (2010).

[21]A. Doostmohammadi, J. Ignés-Mullol, J. M. Yeomans, and F. Sagués, "Active nematics", Nature communications **9**, 1–13 (2018).

[22]G. Duclos, S. Garcia, H. Yevick, and P. Silberzan, "Perfect nematic order in confined monolayers of spindle-shaped cells", Soft matter **10**, 2346–2353 (2014).

[23]M. Deforet, V. Hakim, H. Yevick, G. Duclos, and P. Silberzan, "Emergence of collective modes and tri-dimensional structures from epithelial confinement", Nature communications **5**, 1–9 (2014).

[24]T. B. Saw, W. Xi, B. Ladoux, and C. T. Lim, "Biological tissues as active nematic liquid crystals", Advanced materials **30**, 1802579 (2018).

[25]R. Mayor and C. Carmona-Fontaine, "Keeping in touch with contact inhibition of locomotion", Trends in cell biology **20**, 319–328 (2010).

[26]C. Malinverno, S. Corallino, F. Giavazzi, M. Bergert, Q. Li, M. Leoni, A. Disanza, E. Frittoli, A. Oldani, E. Martini, et al., "Endocytic reawakening of motility in jammed epithelia", Nature materials **16**, 587–596 (2017).

[27]D. T. Tambe, C. Corey Hardin, T. E. Angelini, K. Rajendran, C. Y. Park, X. Serra-Picamal, E. H. Zhou, M. H. Zaman, J. P. Butler, D. A. Weitz, et al., "Collective cell guidance by cooperative intercellular forces", Nature materials **10**, 469–475 (2011).

[28]M. Abercrombie and J. E. Heaysman, "Observations on the social behaviour of cells in tissue culture: ii."monolayering" of fibroblasts", Experimental cell research **6**, 293–306 (1954).

[29]M. Abercrombie, "Contact inhibition and malignancy", Nature **281**, 259–262 (1979).

[30]C. Carmona-Fontaine, H. K. Matthews, S. Kuriyama, M. Moreno, G. A. Dunn, M. Parsons, C. D. Stern, and R. Mayor, "Contact inhibition of locomotion in vivo controls neural crest directional migration", Nature **456**, 957–961 (2008).

[31]A. Palamidessi, C. Malinverno, E. Frittoli, S. Corallino, E. Barbieri, S. Sigismund, G. V. Beznoussenko, E. Martini, M. Garre, I. Ferrara, et al., "Unjamming overcomes kinetic and proliferation arrest in terminally differentiated cells and promotes collective motility of carcinoma", Nature materials **18**, 1252–1263 (2019).

[32]F. Giavazzi, M. Paoluzzi, M. Macchi, D. Bi, G. Scita, M. L. Manning, R. Cerbino, and M. C. Marchetti, "Flocking transitions in confluent tissues", Soft matter **14**, 3471–3477 (2018).

[33]J. H. Kim, X. Serra-Picamal, D. T. Tambe, E. H. Zhou, C. Y. Park, M. Sadati, J.-A. Park, R. Krishnan, B. Gweon, E. Millet, et al., "Propulsion and navigation within the advancing monolayer sheet", Nature materials **12**, 856–863 (2013).

[34]C. Blanch-Mercader and J. Casademunt, "Hydrodynamic instabilities, waves and turbulence in spreading epithelia", Soft matter **13**, 6913–6928 (2017).

[35]G. Duclos, C. Blanch-Mercader, V. Yashunsky, G. Salbreux, J.-F. Joanny, J. Prost, and P. Silberzan, "Spontaneous shear flow in confined cellular nematics", Nature physics **14**, 728–732 (2018).

[36]C. Pérez-González, R. Alert, C. Blanch-Mercader, M. Gómez-González, T. Kolodziej, E. Bazellieres, J. Casademunt, and X. Trepat, "Active wetting of epithelial tissues", Nature physics **15**, 79–88 (2019).

[37]R. Sunyer, V. Conte, J. Escribano, A. Elosegui-Artola, A. Labernadie, L. Valon, D. Navajas, J. M. Garcıa-Aznar, J. J. Muñoz, P. Roca-Cusachs, et al., "Collective cell durotaxis emerges from long-range intercellular force transmission", Science **353**, 1157–1161 (2016).

[38]C.-P. Heisenberg and Y. Bellaıche, "Forces in tissue morphogenesis and patterning", Cell **153**, 948–962 (2013).

[39]X. Trepat, M. R. Wasserman, T. E. Angelini, E. Millet, D. A. Weitz, J. P. Butler, and J. J. Fredberg, "Physical forces during collective cell migration", Nature physics **5**, 426–430 (2009).

[40]R. Alert and X. Trepat, "Physical models of collective cell migration", Annu. Rev. Condens. Matter Phys **11**, 77–101 (2020).

[41]S. Henkes, Y. Fily, and M. C. Marchetti, "Active jamming: self-propelled soft particles at high density", Physical Review E **84**, 040301 (2011).

[42]D. L. Barton, S. Henkes, C. J. Weijer, and R. Sknepnek, "Active vertex model for cell-resolution description of epithelial tissue mechanics", PLoS computational biology **13**, e1005569 (2017).

[43]D. Bi, X. Yang, M. C. Marchetti, and M. L. Manning, "Motility-driven glass and jamming transitions in biological tissues", Physical Review X **6**, 021011 (2016).

[44]D. Bi, J. H. Lopez, J. M. Schwarz, and M. L. Manning, "Energy barriers and cell migration in densely packed tissues", Soft matter **10**, 1885–1890 (2014).

[45]M. Chiang and D. Marenduzzo, "Glass transitions in the cellular potts model", EPL (Europhysics Letters) **116**, 28009 (2016).

[46]B. Smeets, R. Alert, J. Pešek, I. Pagonabarraga, H. Ramon, and R. Vincent, "Emergent structures and dynamics of cell colonies by contact inhibition of locomotion", Proceedings of the National Academy of Sciences **113**, 14621–14626 (2016).

[47]F. Graner and J. A. Glazier, "Simulation of biological cell sorting using a two-dimensional extended potts model", Physical review letters **69**, 2013 (1992).

[48]J. A. Glazier and F. Graner, "Simulation of the differential adhesion driven rearrangement of biological cells", Physical Review E **47**, 2128 (1993).

[49]A. Szabó, R. Ünnep, E. Méhes, W. Twal, W. Argraves, Y. Cao, and A. Czirók, "Collective cell motion in endothelial monolayers", Physical Biology **7**, 046007 (2010).

[50]J.-A. Park, J. H. Kim, D. Bi, J. A. Mitchel, N. T. Qazvini, K. Tantisira, C. Y. Park, M. McGill, S.-H. Kim, B. Gweon, et al., "Unjamming and cell shape in the asthmatic airway epithelium", Nature materials **14**, 1040–1048 (2015).

[51]M. Aliee, J.-C. Röper, K. P. Landsberg, C. Pentzold, T. J. Widmann, F. Jülicher, and C. Dahmann, "Physical mechanisms shaping the drosophila dorsoventral compartment boundary", Current biology **22**, 967–976 (2012).

[52]J. Comelles, S. Soumya, L. Lu, E. Le Maout, S. Anvitha, G. Salbreux, F. Jülicher, M. M. Inamdar, and D. Riveline, "Epithelial colonies in vitro elongate through collective effects", Elife **10** (2021).

[53]E. Teomy, D. A. Kessler, and H. Levine, "Confluent and nonconfluent phases in a model of cell tissue", Physical Review E **98**, 042418 (2018).

[54]A. Das, S. Sastry, and D. Bi, "Controlled neighbor exchanges drive glassy behavior, intermittency, and cell streaming in epithelial tissues", Physical Review X **11**, 041037 (2021).

[55]R. Mueller, J. M. Yeomans, and A. Doostmohammadi, "Emergence of active nematic behavior in monolayers of isotropic cells", Physical review letters **122**, 048004 (2019).

[56]G. Zhang, R. Mueller, A. Doostmohammadi, and J. M. Yeomans, "Active inter-cellular forces in collective cell motility", Journal of the Royal Society Interface **17**, 20200312 (2020).

[57]G. Zhang and J. M. Yeomans, "Active forces in confluent cell monolayers", arXiv preprint arXiv:2111.14401 (2021).

[58]P.-G. De Gennes and J. Prost, *The physics of liquid crystals*, 83 (Oxford university press, 1993).

[59]F. Reinitzer, "Beiträge zur kenntniss des cholesterins", Monatshefte für Chemie und verwandte Teile anderer Wissenschaften **9**, 421–441 (1888).

[60]S. Chandrasekhar, B. Sadashiva, and K. Suresh, "Liquid crystals of disc-like molecules", pramana **9**, 471–480 (1977).

[61]E. F. Gramsbergen, L. Longa, and W. H. de Jeu, "Landau theory of the nematic-isotropic phase transition", Physics Reports **135**, 195–257 (1986).

[62]R. A. Simha and S. Ramaswamy, "Hydrodynamic fluctuations and instabilities in ordered suspensions of self-propelled particles", Physical review letters **89**, 058101 (2002).

[63]A. J. Vromans and L. Giomi, "Orientational properties of nematic disclinations", Soft matter **12**, 6490–6495 (2016).

[64]X. Tang and J. V. Selinger, "Orientation of topological defects in 2d nematic liquid crystals", Soft matter **13**, 5481–5490 (2017).

[65]R. Di Leonardo, S. Keen, F. Ianni, J. Leach, M. Padgett, and G. Ruocco, "Hydrodynamic interactions in two dimensions", Physical Review E **78**, 031406 (2008).

[66]L. Giomi, M. J. Bowick, P. Mishra, R. Sknepnek, and M. Cristina Marchetti, "Defect dynamics in active nematics", Philosophical Transactions of the Royal Society A: Mathematical, Physical and Engineering Sciences **372**, 20130365 (2014).

[67]Z. Püspöki, M. Storath, D. Sage, and M. Unser, "Transforms and operators for directional bioimage analysis: a survey", Focus on bio-image informatics, 69–93 (2016).

[68]W. J. Boettinger, J. A. Warren, C. Beckermann, and A. Karma, "Phase-field simulation of solidification", Annual review of materials research **32**, 163–194 (2002).

[69]K. Kassner and C. Misbah, "A phase-field approach for stress-induced instabilities", EPL (Europhysics Letters) **46**, 217 (1999).

[70]L.-Q. Chen, "Phase-field models for microstructure evolution", Annual review of materials research **32**, 113–140 (2002).

[71]I. Aranson, V. Kalatsky, and V. Vinokur, "Continuum field description of crack propagation", Physical review letters **85**, 118 (2000).

[72]B. Bourdin, G. A. Francfort, and J.-J. Marigo, "Numerical experiments in revisited brittle fracture", Journal of the Mechanics and Physics of Solids **48**, 797–826 (2000).

[73]A. Karma, D. A. Kessler, and H. Levine, "Phase-field model of mode iii dynamic fracture", Physical Review Letters **87**, 045501 (2001).

[74]I. McCue, B. Gaskey, P.-A. Geslin, A. Karma, and J. Erlebacher, "Kinetics and morphological evolution of liquid metal dealloying", Acta Materialia **115**, 10–23 (2016).

[75]P.-A. Geslin, I. McCue, B. Gaskey, J. Erlebacher, and A. Karma, "Topology-generating interfacial pattern formation during liquid metal dealloying", Nature communications **6**, 1–8 (2015).

[76]M. R. Tonks, A. Cheniour, and L. Aagesen, "How to apply the phase field method to model radiation damage", Computational Materials Science **147**, 353–362 (2018).

[77]Q. Du, C. Liu, and X. Wang, "Simulating the deformation of vesicle membranes under elastic bending energy in three dimensions", Journal of computational physics **212**, 757–777 (2006).

[78]S. Aland, S. Egerer, J. Lowengrub, and A. Voigt, "Diffuse interface models of locally inextensible vesicles in a viscous fluid", Journal of computational physics **277**, 32–47 (2014).

[79]F. Ziebert and I. S. Aranson, "Computational approaches to substrate-based cell motility", npj Computational Materials **2**, 1–16 (2016).

[80]M. E. Cates and E. Tjhung, "Theories of binary fluid mixtures: from phase-separation kinetics to active emulsions", Journal of Fluid Mechanics **836** (2018).

[81]B. Palmieri, Y. Bresler, D. Wirtz, and M. Grant, "Multiple scale model for cell migration in monolayers: elastic mismatch between cells enhances motility", Scientific reports **5**, 1–13 (2015).

[82]A. J. Kabla, "Collective cell migration: leadership, invasion and segregation", Journal of the Royal Society Interface **9**, 3268–3278 (2012).

[83]J. Notbohm, S. Banerjee, K. J. Utuje, B. Gweon, H. Jang, Y. Park, J. Shin, J. P. Butler, J. J. Fredberg, and M. C. Marchetti, "Cellular contraction and polarization drive collective cellular motion", Biophysical Journal **110**, 2729–2738 (2016).

[84]G. Peyret, R. Mueller, J. d'Alessandro, S. Begnaud, P. Marcq, R.-M. Mège, J. M. Yeomans, A. Doostmohammadi, and B. Ladoux, "Sustained oscillations of epithelial cell sheets", Biophysical journal **117**, 464–478 (2019).

[85]L. Coburn, L. Cerone, C. Torney, I. D. Couzin, and Z. Neufeld, "Tactile interactions lead to coherent motion and enhanced chemotaxis of migrating cells", Physical Biology **10**, 046002 (2013).

[86]J. Löber, F. Ziebert, and I. S. Aranson, "Collisions of deformable cells lead to collective migration", Scientific reports **5**, 1–7 (2015).

[87]S. Henkes, K. Kostanjevec, J. M. Collinson, R. Sknepnek, and E. Bertin, "Dense active matter model of motion patterns in confluent cell monolayers", Nature Communications **11**, 1405 (2020).

[88]V. Maruthamuthu, B. Sabass, U. S. Schwarz, and M. L. Gardel, "Cell-ecm traction force modulates endogenous tension at cell–cell contacts", Proceedings of the National Academy of Sciences **108**, 4708–4713 (2011).

[89]A. F. Mertz, Y. Che, S. Banerjee, J. M. Goldstein, K. A. Rosowski, S. F. Revilla, C. M. Niessen, M. C. Marchetti, E. R. Dufresne, and V. Horsley, "Cadherin-based intercellular adhesions organize epithelial cell–matrix traction forces", Proceedings of the National Academy of Sciences **110**, 842–847 (2013).

[90]J. Löber, F. Ziebert, and I. S. Aranson, "Modeling crawling cell movement on soft engineered substrates", Soft matter **10**, 1365–1373 (2014).

[91]F. Ziebert, S. Swaminathan, and I. S. Aranson, "Model for self-polarization and motility of keratocyte fragments", Journal of The Royal Society Interface **9**, 1084–1092 (2012).

[92]E. Tjhung, A. Tiribocchi, D. Marenduzzo, and M. E. Cates, "A minimal physical model captures the shapes of crawling cells", Nature communications **6**, 1–9 (2015).

[93]M. Nonomura, "Study on multicellular systems using a phase field model", PloS one **7**, e33501 (2012).

[94]B. Loewe, M. Chiang, D. Marenduzzo, and M. C. Marchetti, "Solid-liquid transition of deformable and overlapping active particles", Physical Review Letters **125**, 038003 (2020).

[95]B. A. Camley, Y. Zhang, Y. Zhao, B. Li, E. Ben-Jacob, H. Levine, and W.-J. Rappel, "Polarity mechanisms such as contact inhibition of locomotion regulate persistent rotational motion of mammalian cells on micropatterns", Proceedings of the National Academy of Sciences **111**, 14770–14775 (2014).

[96]W. Marth and A. Voigt, "Collective migration under hydrodynamic interactions: a computational approach", Interface Focus **6**, 20160037 (2016).

[97]D. Wenzel, S. Praetorius, and A. Voigt, "Topological and geometrical quantities in active cellular structures", The Journal of chemical physics **150**, 164108 (2019).

[98]D. Bi, J. Lopez, J. M. Schwarz, and M. L. Manning, "A density-independent rigidity transition in biological tissues", Nature Physics **11**, 1074–1079 (2015).

[99]J. Deseigne, O. Dauchot, and H. Chaté, "Collective motion of vibrated polar disks", Physical Review Letters **105**, 098001 (2010).

[100]D. Grossman, I. Aranson, and E. B. Jacob, "Emergence of agent swarm migration and vortex formation through inelastic collisions", New Journal of Physics **10**, 023036 (2008).

[101]D. T. Tambe, U. Croutelle, X. Trepat, C. Y. Park, J. H. Kim, E. Millet, J. P. Butler, and J. J. Fredberg, "Monolayer stress microscopy: limitations, artifacts, and accuracy of recovered intercellular stresses", PLoS ONE **8**, e55172 (2013).

[102]C. Blanch-Mercader, V. Yashunsky, S. Garcia, G. Duclos, L. Giomi, and P. Silberzan, "Turbulent dynamics of epithelial cell cultures", Physical review letters **120**, 208101 (2018).

[103]F. Vafa, M. J. Bowick, B. I. Shraiman, and M. C. Marchetti, "Fluctuations can induce local nematic order and extensile stress in monolayers of motile cells", Soft Matter **17**, 3068–3073 (2021).

[104]A. Patelli, I. Djafer-Cherif, I. S. Aranson, E. Bertin, and H. Chaté, "Understanding dense active nematics from microscopic models", Physical review letters **123**, 258001 (2019).

[105]A. Killeen, T. Bertrand, and C. F. Lee, "Polar fluctuations lead to extensile nematic behavior in confluent tissues", Physical Review Letters **128**, 078001 (2022).

[106]M. Abercrombie, "Contact inhibition in tissue culture", In vitro **6**, 128–142 (1970).

[107]B. Stramer and R. Mayor, "Mechanisms and in vivo functions of contact inhibition of locomotion", Nature reviews Molecular cell biology **18**, 43–55 (2017).

[108]O. J. Meacock, A. Doostmohammadi, K. R. Foster, J. M. Yeomans, and W. M. Durham, "Bacteria solve the problem of crowding by moving slowly", Nature Physics **17**, 205–210 (2021).

[109]H. H. Wensink, J. Dunkel, S. Heidenreich, K. Drescher, R. E. Goldstein, H. Löwen, and J. M. Yeomans, "Meso-scale turbulence in living fluids", Proceedings of the National Academy of Sciences **109**, 14308–14313 (2012).

[110]N. Khalilgharibi, J. Fouchard, N. Asadipour, R. Barrientos, M. Duda, A. Bonfanti, A. Yonis, A. Harris, P. Mosaffa, Y. Fujita, et al., "Stress relaxation in epithelial monolayers is controlled by the actomyosin cortex", Nature physics **15**, 839–847 (2019).

[111]S. Tlili, M. Durande, C. Gay, B. Ladoux, F. Graner, and H. Delanoë-Ayari, "Migrating epithelial monolayer flows like a maxwell viscoelastic liquid", Physical Review Letters **125**, 088102 (2020).

[112]A. Mongera, P. Rowghanian, H. J. Gustafson, E. Shelton, D. A. Kealhofer, E. K. Carn, F. Serwane, A. A. Lucio, J. Giammona, and O. Campàs, "A fluid-to-solid jamming transition underlies vertebrate body axis elongation", Nature **561**, 401–405 (2018).

[113]V. Yashunsky, D. Pearce, C. Blanch-Mercader, F. Ascione, L. Giomi, and P. Silberzan, "Chiral edge currents in confined fibrosarcoma cells", arXiv preprint arXiv:2010.15555 (2020).

[114]R. Voituriez, J.-F. Joanny, and J. Prost, "Spontaneous flow transition in active polar gels", EPL (Europhysics Letters) **70**, 404 (2005).

[115]M. Trulsson, "Rheology and shear jamming of frictional ellipses", Journal of Fluid Mechanics **849**, 718–740 (2018).

[116]V. Petrolli, M. Le Goff, M. Tadrous, K. Martens, C. Allier, O. Mandula, L. Hervé, S. Henkes, R. Sknepnek, T. Boudou, G. Cappello, and M. Balland, "Confinement-induced transition between wavelike collective cell migration modes", Phys. Rev. Lett. **122**, 168101 (2019).

[117]L. Emmanuel, H. Le Thi, J. M. Yeomans, and A. Doostmohammadi, "Self-sustained oscillations of active viscoelastic matter", Journal of Physics A: Mathematical and Theoretical **55**, 275601 (2022).

[118]Y. Kaizuka, R. Machida, and Y. Ota, "Mechanochemical regulation of cell adhesion by incorporation of synthetic polymers to plasma membranes", Langmuir **37**, 366–375 (2020).

[119]X. Serra-Picamal, V. Conte, R. Vincent, E. Anon, D. T. Tambe, E. Bazellieres, J. P. Butler, J. J. Fredberg, and X. Trepat, "Mechanical waves during tissue expansion", Nature Physics **8**, 628–634 (2012).

[120]P.-F. Lenne, E. Munro, I. Heemskerk, A. Warmflash, L. Bocanegra-Moreno, K. Kishi, A. Kicheva, Y. Long, A. Fruleux, A. Boudaoud, et al., "Roadmap for the multiscale coupling of biochemical and mechanical signals during development", Physical biology **18**, 041501 (2021).

[121]N. Hino, L. Rossetti, A. Marın-Llauradó, K. Aoki, X. Trepat, M. Matsuda, and T. Hirashima, "Erk-mediated mechanochemical waves direct collective cell polarization", Developmental cell **53**, 646–660 (2020).

[122]D. Boocock, N. Hino, N. Ruzickova, T. Hirashima, and E. Hannezo, "Theory of mechanochemical patterning and optimal migration in cell monolayers", Nature physics **17**, 267–274 (2021).

[123]G. W. Brodland and H. H. Chen, "The mechanics of cell sorting and envelopment", Journal of Biomechanics **33**, 845–851 (2000).

[124]M. Bayram, T. Partal, and G. Orucova Buyukoz, "Numerical methods for simulation of stochastic differential equations", Advances in Difference Equations **2018**, 1–10 (2018).

[125]J. Bigun, *Optimal orientation detection of linear symmetry*, 1987.

[126]J. Hobdell and A. Windle, "A numerical technique for predicting microstructure in liquid crystalline polymers", Liquid crystals **23**, 157–173 (1997).

[127]A. Nestor-Bergmann, G. Goddard, S. Woolner, and O. E. Jensen, "Relating cell shape and mechanical stress in a spatially disordered epithelium using a vertex-based model", Mathematical medicine and biology: a journal of the IMA **35**, i1–i27 (2018).

[128]A. Drescher and G. Jong, "Photoelastic verification of a mechanical model for the flow of a granular material", in *Soil mechanics and transport in porous media* (Springer, 2006), pp. 28–43.

[129]A. N. Norris, "Mechanics of elastic networks", Proceedings of the Royal Society A: Mathematical, Physical and Engineering Sciences **470**, 20140522 (2014).